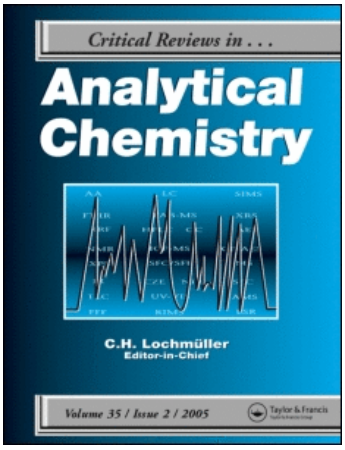


**Critical Reviews in Analytical Chemistry**
Publication details, including instructions for authors and subscription information:
http://www.informaworld.com/smpp/title~content=t713400837

# X-Ray Scattering Methods for the Study of Polymer Interfaces

Mark D. Foster[a]
[a] Department of Polymer Science, The University of Akron, Akron, OH

**To cite this Article** Foster, Mark D.(1993) 'X-Ray Scattering Methods for the Study of Polymer Interfaces', Critical Reviews in Analytical Chemistry, 24: 3, 179 — 241
**To link to this Article: DOI:** 10.1080/10408349308050553
**URL:** http://dx.doi.org/10.1080/10408349308050553

*Critical Reviews in Analytical Chemistry*, 24(3):179–241 (1993)

# X-Ray Scattering Methods for the Study of Polymer Interfaces

*Mark D. Foster*

The University of Akron, Department of Polymer Science, Akron, OH 44325-3909

**ABSTRACT:** A variety of characterization methods based on X-ray scattering may be used to sensitively probe the structure of polymer surfaces and interfaces. Among these are small angle scattering in transmission, specular reflectivity, grazing incidence off-specular scattering, and grazing incidence diffraction. X-ray measurements provide information on electron density differences across interfaces, total interfacial area and volume fraction of a dispersed phase, microroughness of sharp interfaces, interface width, parameters of near-interface electron density profiles, and in-plane ordering in thin films and near surfaces. This review focuses on experimental aspects of the methods as analytical techniques, considering the relative merits of different approaches, and reviewing some recent measurements not yet reviewed elsewhere. Particular attention is given to the rapidly growing fields of specular reflectivity and off-specular scattering. After discussing general theoretical concepts applicable to all the techniques and general instrumentation requirements, each method is considered in turn. For each, the basic theory and methods of analysis are presented, followed by a description of specific instrumentation needs and notes on sample preparation. In the cases of off-specular scattering and grazing incidence diffraction some examples of recent applications are reviewed. A few remarks on prospects for further development of the various techniques are offered as well.

**KEY WORDS:** X-ray scattering, polymer interfaces, characterization, small angle scattering, reflectivity, diffuse scattering, grazing incidence diffraction.



## I. INTRODUCTION

The study of interfaces is key to advances being made in a variety of technologies using polymers including adhesives, coatings, biomedicine, microelectronics, miniature sensors, and others. It is, therefore, imperative that those involved in research in these areas be familiar with the unique opportunities and limitations of various techniques for polymer interface characterization. A wide variety of analytical methods have been developed, many of them in the recent past. Surface chemical composition and molecular orientation have been probed, for example, with X-ray photoelectron spectroscopy (XPS or ESCA),[1] static secondary ion mass spectroscopy (SSIMS),[2] Auger spectroscopy (AES),[1] and grazing incidence Fourier transform infrared spectroscopy (GI-FTIR).[3] Microscopies, including transmission electron microscopy (TEM),[4] atomic force microscopy (AFM),[5] phase interferometric microscopy (PIM),[6] and plasmon enhanced microscopy (PEM)[7] have provided information on surface topology and domain boundaries in thin films. Concentration depth profiling, including the study of interfacial widths has been pursued with ion bombardment techniques such as dynamic secondary ion mass spectroscopy (DSIMS),[8] forward recoil spectroscopy (FRES),[9] Rutherford backscattering (RB),[9] and nuclear reaction analysis (NRA),[10] as well as with infrared microdensitometry (IR-MD),[11] attenuated reflection infrared spectroscopy (ATR-IR),[3] XPS and surface enhanced Raman spectroscopy (SERS).[12] Reflection geometry scattering experiments

1040-8347/93/$.50

using visible light, (ellipsometry, EL),[13] and neutrons (neutron reflectometry, NR)[17,18] have been valuable in measuring structure and kinetics in thin film systems. Overviews of the comparative advantages and disadvantages of these widely varying techniques have been presented by Russell[15] and Stamm.[14]

The focus of this review is on X-ray scattering techniques. They play an important role in the study of polymer interfaces due to their usefulness in characterizing interfaces at some distance from the polymer sample surface and because they may probe structure both parallel and normal to interfaces. In particular, X-ray measurements can provide information on electron density differences across interfaces, total interfacial area and volume fraction of a dispersed phase, microroughness of sharp interfaces, interface width, parameters of near-interface electron density profiles, and in-plane correlations. Their unique strengths and limitations are detailed further in the following sections.

The X-ray scattering techniques discussed in this review include small angle scattering in transmission (SAXS), specular reflectivity, anomalous reflectivity, grazing incidence diffuse scattering, and grazing incidence diffraction. Both SAXS and specular reflectivity have been the subjects of previous reviews,[16-18] and specular reflection of polymers in particular was reviewed in depth fairly recently.[18] The present work builds on and complements these earlier reviews by focusing on experimental aspects of the methods as analytical techniques, considering the relative merits of different approaches, and reviewing some recent measurements not yet reviewed elsewhere. Particular attention is given to the rapidly growing field of off-specular scattering.

The text is divided into three main sections. In this introductory section (I) general theoretical concepts applicable to all the techniques are presented and general instrumentation requirements discussed. Section II covers SAXS, introducing the method, presenting basic theory, and considering various techniques for analyzing the data from two phase systems to account for total interfacial area in the scattering volume, fluctuations within phases, interfacial roughness and curvature, and interface width of diffuse phase boundaries. Notes on instrumentation and sample preparation follow. Section III deals with grazing incidence methods, first discussing general aspects of the grazing incidence geometry and then considering in turn specular reflectivity, near-specular diffuse scattering, and scattering far from the specular direction (grazing incidence diffraction). Anomalous reflectivity and interferometry are treated as variations on specular reflectivity. Within the discussion of each experimental technique methods of analysis, instrumentation, and sample preparation are presented with an extended comparison with SAXS accompanying the discussion of specular reflectivity. Some examples of recent applications are reviewed for the off-specular scattering techniques. A brief concluding section presents an overview and outlook for the future.

### A. Overview of Important Scattering Concepts

The present discussion is predominantly conceptual and illustrative and serves (1) to explain how the interface sensitivity of the X-ray experiment comes about (2) and to provide a basis for discussing the limitations of the technique. A few of the most often used equations are summarized in the sections devoted to specific techniques. In-depth discussions of the general theory and formalism of X-ray scattering may be found in a variety of monographs[19,20] and further details particular to each type of scattering measurement found in articles referenced below. It is important to note that throughout the following discussion only elastic scattering is considered.

A generic scattering experiment is presented schematically in Figure 1. When an incident beam characterized by wave vector $\mathbf{k}_0$ ($k_0 = |\mathbf{k}_0| = 2\pi/\lambda$) strikes a sample, some fraction of it interacts with the electrons in the material in absorption and scattering processes. The direction of the scattered radiation exiting the sample at an angle $2\theta$

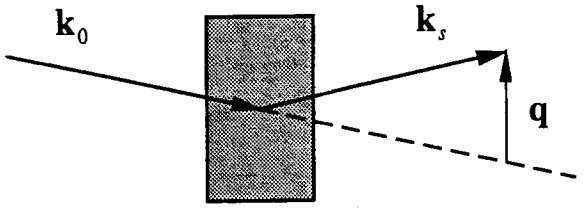


**FIGURE 1.** Schematic of a generic elastic scattering process. An incident beam characterized by wave vector $\mathbf{k}_0$ penetrates into a sample and is scattered through angle $2\theta$. The direction of the scattered beam is then given by $\mathbf{k}_s$.

from the incident direction is described by $\mathbf{k}_s$ and the change in momentum which takes place upon scattering described by the scattering vector $\mathbf{q} \equiv \mathbf{k}_s - \mathbf{k}_0$. When only the magnitude of $2\theta$ is of interest $q = 4\pi \sin\theta/\lambda$ is a convenient variable to use because it accounts for the wavelength, $\lambda$, used as well as for the angle. While the polarizations of incident and scattered beams play an important role in visible light and polarized neutron scattering, they are generally ignored for X-ray experiments. Polarized beams are not readily generated or analyzed.

A general quantity that characterizes the interaction of a material with electromagnetic radiation is its refractive index, $n$. For the specific case of X-rays the refractive index is slightly less than unity and may be written to a good approximation as

$$n = 1 - \delta + i\beta \tag{1}$$

where $\beta$ represents the absorption component

$$\beta = \frac{r_0\lambda^2}{2\pi} N_A \sum_i \frac{\rho_i}{A_i} f_i''(q) \tag{2}$$

and

$$\delta = \frac{r_0\lambda^2}{2\pi} N_A \sum \frac{\rho_i}{A_i} [Z_i + f_i'(q)] \tag{3}$$

where $r_0$ is the classical electron radius ($2.82 \times 10^{-13}$ cm), $\lambda$ is the wavelength, $N_A$ is Avogadro's number, and $\rho_i$, $A_i$, and $Z_i$ are the mass density, atomic weight, and atomic number of element $i$ in the sample. The dispersion and absorption portions of the atomic scattering factors, which are wavelength and scattering angle dependent, are indicated by $f'$ and $f''$, respectively. For small angle scattering the angle dependence of each may be neglected and only the wavelength dependence retained. Typically, $\beta$ is actually determined from a measured mass absorption coefficient, $\mu$

$$\beta = \frac{\mu\lambda}{4\pi} \tag{4}$$

and $\delta$ described in terms of the electron density, $\rho_e$

$$\delta = \frac{\lambda^2}{2\pi} \rho_e r_0 \tag{5}$$

With this definition of a refractive index for X-rays well-known optical methods may be applied to the description of X-ray scattering. When $n$ varies through a sample, waves scattering coherently (i.e., scattered without energy loss) from different sample volume elements interfere. Details of the features of the resulting spectrum are dictated by correlations in $\rho_e$ or $n$ over distances probed by the experiment. The shape of these features is typically described by the differential scattering cross-section, $d\sigma/d\Omega(\mathbf{q})$, which is the scattered intensity per unit solid angle per incident flux. While $n(\mathbf{r})$ describes directly the real space structure of a sample, $d\sigma/d\Omega$ describes the scattering from that sample in reciprocal space.

The intensity observed in an experiment using a pinhole collimated beam of infinitesimal cross-section, expressed as counts per second, is given by

$$I_{expt}(\mathbf{q}) = \Phi \cdot T \cdot E \cdot \int \frac{d\sigma}{d\Omega}(\mathbf{q}) d\Omega \tag{6}$$

where $\Phi$ is the incident flux in photons per area per second, $T$ is a dimensionless transmission coefficient, $E$ is the detector efficiency in counts per photon, and $\Omega$ is the solid angle over which the scattering is col-

lected by the detector. With the appropriate interpretations of $T$ this equation may serve for either transmission or reflection measurements, and thus $T$ is both sample and apparatus dependent. The limits on the integral as well as the factors $\Phi$ and $E$ depend only on the apparatus, while $d\sigma/d\Omega$, the differential cross-section for scattering, is independent of the instrument and contains information on the sample structure. In order to connect the character of the observed scattering with features of the sample structure we will focus first on the form of the differential cross-section, leaving remarks concerning the instrument-dependent parameters for the appropriate instrument specific sections below.

In order to discuss the form of $d\sigma/d\Omega$ in the most intuitive way possible, we begin with the simple case for which one may assume that any incident wave interacts with, or is scattered by, the sample material only once. Multiple scattering effects are neglected and the amplitudes of scattered fields are small with respect to that of the incident field. This limiting case, corresponding to the so-called kinematic or Born approximation, is actually an excellent one for much of the small angle scattering from polymer systems in both transmission and reflection geometries. Only in cases of extremely small incident angles and strongly scattering surfaces will it be necessary to explicitly include multiple scattering effects. Because the Born approximation allows one to derive some analytical results and readily separate various contributions to the scattering, the author will use it whenever possible, though more rigorous results are also summarized.

When the Born approximation is invoked the scattering process may be modeled mathematically using the Fourier transform. The differential cross-section for scattering is given by

$$\frac{d\sigma}{d\Omega}(\mathbf{q}) = r_0^2 \left| \mathrm{F}\{\rho_e(\mathbf{r})\} \right|^2 \qquad (7)$$

where the integration volume, $V$, is the sample volume illuminated by the beam, and $\mathbf{F}\{\rho_e(\mathbf{r})\}$ denotes the Fourier transform of $\rho_e(\mathbf{r})$. For the special case of a two-phase sample in which both phases are uniform and homogeneous at the molecular level and the phase boundaries are sharp, Eq. (7) may be written:

$$\frac{d\sigma}{d\Omega}(\mathbf{q}) = r_0^2 (\Delta\rho_e)^2 \int_V \int_V e^{-i\mathbf{q}(\mathbf{r}-\mathbf{r}')} d\mathbf{r}\, d\mathbf{r}' \qquad (8)$$

Because we wish to focus on the interface or interfaces in the system, it is advantageous to transform the volume integrals in Eq. (8) into surface integrals over the surface, $S$, dividing the two phases[31,139]

$$\frac{d\sigma}{d\Omega}(\mathbf{q}) = r_0^2 (\Delta\rho_e)^2 \frac{1}{(\mathbf{q}\cdot\mathbf{A})^2} \int_S \int_S (d\mathbf{S}\cdot\mathbf{A}) \cdot (d\mathbf{S}'\cdot\mathbf{A}) e^{-i\mathbf{q}\cdot(\mathbf{r}-\mathbf{r}')} \qquad (9)$$

where $\mathbf{A}$ is an arbitrary unit vector in space and $d\mathbf{S}$ is the differential surface vector parallel to the surface normal. The differential cross-section may now be separated conveniently into three terms

$$\frac{d\sigma}{d\Omega}(\mathbf{q}) = r_0^2 (\Delta\rho_e)^2 S_T S(\mathbf{q}) \qquad (10)$$

The first is the contrast factor, which represents the mean square scattering length density fluctuation in the system. For the special case of a two-phase system this is simply the square of the scattering length density difference between the two phases, $r_0^2(\Delta\rho_e)^2$. Second is the total interfacial area in the illuminated sample volume, $S_T = \hat{S}V$, where $\hat{S}$ is the interfacial area per unit sample volume. The third factor is the structure factor $S(\mathbf{q})$, which contains the form of the scattering and depends only on the interfacial structure, not the size or chemistry of the sample. Similar expressions may also be written for the case of more than two phases. For our purposes in this work it is convenient to consider a structure factor which is defined on a per unit surface area basis. It is interesting to note that the differential cross-section may be expressed in the same form for neu-

tron scattering simply by substituting the appropriate quantities in the contrast factor. For neutron scattering, the scattering length per scattering entity is $b_{eff}$ rather than $r_0$, where $b_{eff}$ is the effective nuclear scattering length. The electron density, $\rho_e$, is replaced by the density of nuclei, $N$, so that the contrast factor becomes $[\Delta(Nb)]^2$.

The calculation of experimentally measured intensities involves including details of the apparatus. Relative intensities $I_{expt}(\mathbf{q})$ in counts per second are obtained by convoluting $d\sigma/d\Omega$ with the instrumental resolution function and multiplying by the factors $\Phi$, $T$, and $E$ defined for Eq. (6). When a pinhole beam is used the resolution convolution is simply the integration shown in Eq. (6). However, in general the required convolution is more complex. Relative intensities are so named because they are apparatus dependent. If one wishes to compare intensities measured in different laboratories all must be corrected for collimation effects and normalized for incident flux, detector efficiency, and transmission coefficient. Once corrected, these are referred to as absolute intensities.

Using Eq. (7) and (10) one can readily point out several general aspects of the scattering behavior of an interface. First, the form of the scattering is clearly determined by the structure of the interface alone. Second, the magnitude of the scattered intensity measured with a single apparatus using samples of equivalent geometry will vary with the total interfacial area $S_T$ and contrast $r_0^2(\Delta\rho_e)^2$. $S_T$ will depend on the illuminated volume and phase volume fractions $\phi_i$, while the contrast will vary with the mass densities and chemical compositions of the two phases. If one were to generalize Eq. (10) for systems of several phases one would find that the interface presenting the greatest contrast (i.e., across which $\Delta\rho_e$ is largest) tends to dominate the scattering behavior.

A property of the Fourier transformation dictates that features of $\rho_e(\mathbf{r})$ which occur at small $r$ will be seen in $F\{\rho_e(r)\}$, and thus $d\sigma/d\Omega(\mathbf{q})$, at large $\mathbf{q}$. Therefore, in order to precisely study details of interfaces between phases one will need to measure data over a larger range of $\mathbf{q}$ than is needed for study of large-scale sample features. Roughly speaking, the resolution of real space structure justified by a given data set varies as $2\pi/q_{max}$, where $q_{max}$ is the largest value of $q$ for which data are collected.

An important aspect and key limitation of all X-ray scattering techniques is that in general it is impossible to obtain uniquely from the raw data a picture of the sample structure in real space. While the inverse of Fourier transformation may be readily defined, scattering data generally may not be inverted to yield $\rho_e(\mathbf{r})$ directly because only a portion of the function $d\sigma/d\Omega(\mathbf{q})$ is measured in any real experiment. Also, the phase information is generally lost, although some special techniques allow one to circumvent the phase loss problem.[95,123,124] When considering standard X-ray results alone it is only possible to argue that a given structure model is or is not consistent with the observations. Fortunately, however, often clues to the structure are available from other observations and intuition and it is possible to tightly constrain potential models.

## B. General Notes on Instrumentation

Measurement of X-ray scattering phenomena requires two basic elements, a radiation source, and a diffractometer, also called a camera or spectrometer. When appraising the suitability of an instrument to a particular analysis or specifying a system, the important issues to consider are resolution, sensitivity, speed of measurement, and cost. For a given resolution, speed is determined by source intensity and detection efficiency and speed may be gained if one is willing to relinquish resolution.

Two general source types are the tube source and the synchrotron. Common X-ray tubes are of the sealed or rotating target type, with the rotating target offering a factor of 10 increase in intensity at a substantial increase in capital expenditure, system complexity, and maintenance cost. The rotating anode focus stability is also not as good as that of the sealed tube. With either tube type various wavelengths of radiation may be ob-

tained by securing a selection of targets of various materials, generally at substantial additional cost. Because the focus acts effectively as the first slit in the collimation of the beam, the attainable collimation and intensity is dependent on the focus type. A fine focus in either a slit or point configuration offers the finest collimation and greatest brilliance at a loss of total intensity and stability. The point focus has analytical advantages, but the slit focus allows one to maximize total intensity while paying a price in ease of data analysis by introducing a substantial loss of collimation in one beam dimension.

Synchrotron sources, while available only at large, centralized user facilities, present a marvelous combination of remarkable intensity, intrinsically outstanding collimation, and wavelength tunability.[21] These capabilities are demanded by more sophisticated and difficult scattering experiments, particularly when time-resolved *in situ* data are required.

Many similarities exist among the diffractometers used for different types of X-ray scattering measurements and these are highlighted here, while the differences are discussed in the sections below dealing with the various techniques. Key features, shown schematically in Figure 2, are components for monochromatization, collimation, sample positioning and environmental control, scattered beam analysis, and detection. Additional components used in some setups include mirrors for redirecting or focusing the beam and beam intensity monitors.

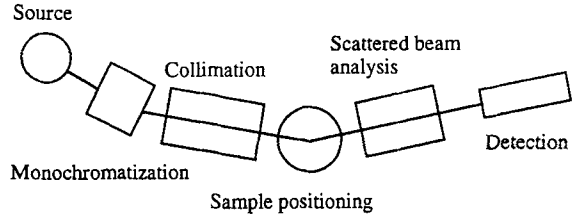


**FIGURE 2.** In a generic scattering apparatus X-rays generated by the source are collimated and often monochromated before striking the sample. The scattered beam may then be analyzed for direction or energy or both before being detected.

## II. SMALL ANGLE SCATTERING IN TRANSMISSION (SAXS)

### A. Introduction

In transmission methods[60] the primary beam strikes the sample perpendicular to the surface, penetrates through the sample, and emerges from the opposite side. The unscattered and forward scattered beams are blocked before reaching the detector and not analyzed, while the small fraction of intensity associated with photons scattered away from the incident direction is carefully observed. Because the entire sample thickness is probed in such techniques, scattering from the near-surface regions comprise only a very small fraction of the overall scattering. Thus, the measurements are generally sensitive to "bulk" rather than "surface" structure. However, some information on interfaces between regions within the sample is available from scattering at the largest $q$ values studied with SAXS. Measured intensities are affected by the total electron density fluctuations in the scattering volume, total and specific interfacial area in a multiphase system, interfacial microroughness and curvature, and width of diffuse interfaces. In principle parameter values characterizing all of these features may be derived from the SAXS data.[24]

The method denoted classically as "small angle X-ray scattering" is that which employs a transmission geometry and detection of the scattered radiation over a range of a few milliradians to a few degrees as shown schematically in Figure 3. An example of a small angle scattering measurement from a polymer sample[23] is shown in Figure 4. It is important to note that in this experiment the internal interfaces studied may in general lie at all possible orientations to the incident beam direction (in contrast to reflectivity experiments). Therefore, in the equations outlined below we assume an isotropic sample and consider expressions for scattering averaged over all orientations of the incident beam on the interface. To emphasize this orientation averaging we represent the corresponding structure factor as $\bar{S}(q)$.

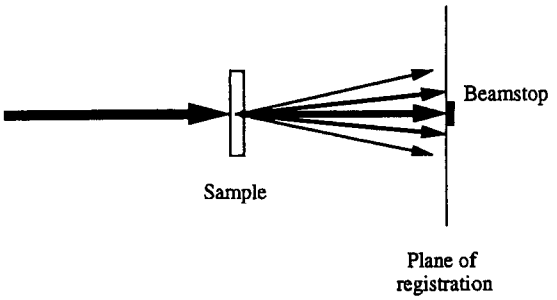


**FIGURE 3.** In classical small angle X-ray scattering the incident beam is perpendicular to the sample surface and the entire sample thickness is probed.

## B. Theory and Analysis

### 1. General Equations

The most widely exploited basis for obtaining information on interfaces using this technique is the so-called Porod's law and experimentally observed deviations from it.[31,34] Porod[28-30] obtains an expression for the small angle scattering asymptotic behavior for a two-phase system under the two assumptions that the individual phases are homogeneous on an atomic scale and that the interfaces between phases are atomically sharp. In this limit the absolute intensity measured using a point collimation is given for an isotropic system by

$$\lim_{q \to \infty} I_{\text{expt}}(q) = K_P q^{-4} \qquad (11)$$

$$K_P = I_e(q) 2\pi (\Delta\rho_e)^2 S_T \qquad (12)$$

where $I_e(q)$ is the absolute scattering intensity from a single electron under the prevailing experimental conditions. If all sample parameters and camera parameters are kept constant, the use of this equation presents a simple way to estimate the relative amounts of surface area in two samples. In many cases, however, it may be desirable to determine the surface area per unit sample vol-

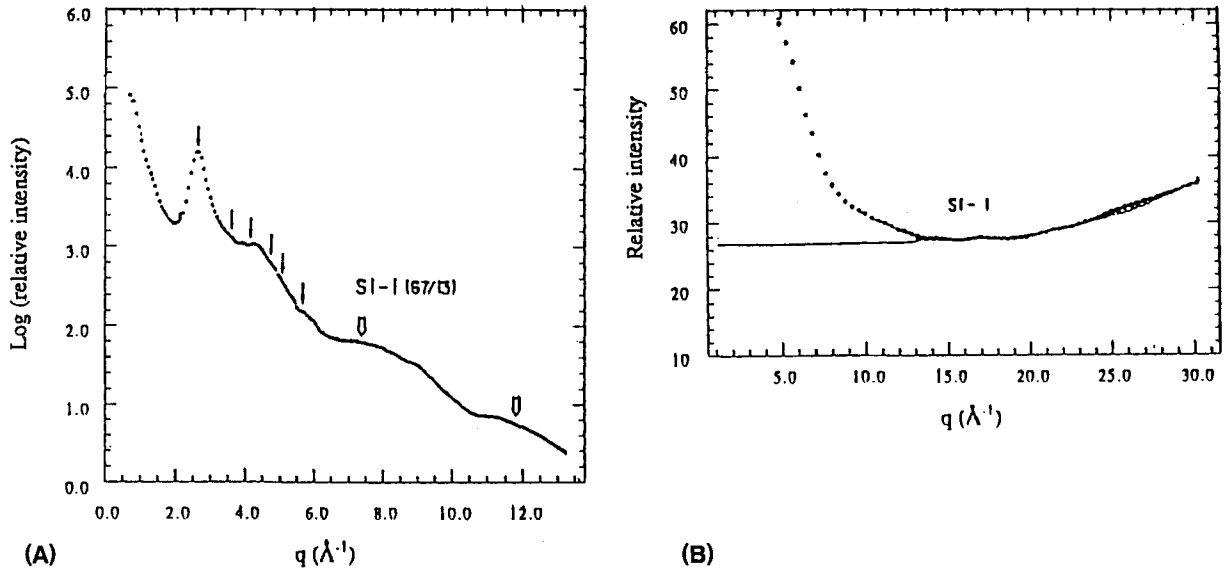


**FIGURE 4.** (A) Relative, desmeared scattering intensity curve[23] from a polystyrene-polystyrene diblock copolymer solution cast film with spherical domains corrected for air scattering and background scattering from each of the amorphous microphases. The polymer has total molecular weight, $M_r$, of 80,000 g / mol and is 16 wt% PI. The SAXS from this system is unusually rich, displaying a strong first maximum characteristic of a nearest-neighbor distance between domains at $q = 0.0259$ Å$^{-1}$ as well as broad maxima related to the scattering characteristic of the spherical shape of the single domain. (B) Relative, smeared intensity curve[23] for the same PS-PI sample corrected for air scattering and absorption. These data over a broader range of $q$ display clearly the fluctuation scattering which must be subtracted before determination of the interface width. The solid curve shows a fit to the background using Eq. (26). (Reproduced, with permission, from reference 23.)

ume, $\hat{S}$. This may be done by dividing $S_T$ by an illuminated sample volume calculated from the sample thickness and a knowledge of the beam cross-section at the sample. The difficult part of this determination is quantification of the absolute intensity of the incident beam, which is needed to calculate $I_e$. Such a calibration performed using a secondary standard is typically subject to error of 10 to 20%,[25,26] although with effort the error can be perhaps halved.

Porod also shows that $\hat{S}$ can be obtained without an absolute intensity determination by using the invariant, $Q$, measured in relative intensity units. The invariant is defined as

$$Q \equiv \int_0^\infty q^2 I(q)\, dq \qquad (13)$$

Its name derives from the fact that its value depends only on the mean squared electron density fluctuation in the sample and not on particulars of the how the fluctuations are distributed. In other words, for a rigorously two-phase system with uniform phases of volume fraction $\phi_1$ and $\phi_2$ separated by sharp boundaries and illuminated volume, $V$,

$$Q = 2\pi^2 I_e(q) V (\Delta\rho_e)^2 \phi_1 (1 - \phi_1) \qquad (14)$$

and

$$\hat{S} = \pi \phi_1 (1 - \phi_1) \left\{ \frac{\lim_{q \to \infty} [q^4 I(q)]}{Q} \right\} \qquad (15)$$

This second method of obtaining the specific surface using the invariant has its own shortcomings because one must evaluate an integral over a $q$ range from zero to infinity. However, when both the invariant and absolute intensity are evaluated one can obtain estimates of two further structural parameters, the two-phase volume fractions.

Because experiment provides values of $I(q)$ only over a limited range of $q$, one must rely on extrapolations to zero and large $q$ to approximate the value of $Q$. Minimizing the error in these extrapolations requires careful technique and adequate instrumentation, so that $I$ is measured as close to the main beam as possible and also to large enough $q$ that the extrapolation is reliable. If the data do extend into the region of asymptotic behavior and Eq. (11) is followed experimentally, it is clear that the extrapolation should be straightforward. As discussed below, the intensity in general does not follow the simple relationship presented in Eq. (11), and more complicated functional forms must be used to describe the data at large $q$ and to perform the extrapolation. The signal to noise ratio in the $q$ range over which the extrapolation to $q = \infty$ is carried out is generally quite small, requiring long measurement times to reduce statistical errors to a reasonable level.

The challenge of obtaining sufficient statistics in the Porod region may be answered in part by using slit collimation, as one may gain a factor of 10 in intensity over that obtained with point collimation. When using the slit collimation, however, application of the above analysis requires the deconvolution of collimation effects from the data (also called "desmearing")[27] or a modification of the equations to be used. A Gaussian distribution[42,43] may often be used as a good approximation for the incident intensity distribution, $W_l(u)$, along the beam height, measured in the plane of registration

$$W_l(u) = W_l(0) \exp(-p^2 u^2) \qquad (16)$$

The relative position, $u$, along the slit is expressed in reciprocal length units and represents a real space position $x$ normalized by the sample to detector distance, $a$, and wavelength, $\lambda$

$$u = \frac{2\pi x}{a\lambda} \qquad (17)$$

The effective height of the beam is reflected in $p$, which is related to the standard deviation of the distribution and decreases as the height increases. $W_l(0)$ is the normalization constant. In the case that our slit is much longer than it is wide, and smearing due to the detector aperture and wavelength distribution may be neglected, the collimation

convolution required for the SAXS experiment may be expressed as

$$\tilde{I}_{\text{expt}}(q) = \int_{-\infty}^{\infty} W_i(u) I\left(\sqrt{q^2 + u^2}\right) du \quad (18)$$

Because deconvolution is an inherently unstable procedure[27] it is often advantageous to operate with a slit collimation which at least approximately satisfies the so-called infinite slit approximation, where the dimension of the beam perpendicular to the axis along which the data are collected (the height) is much larger than the beam dimension parallel to the data collection axis (the width). In this case the collimation effects can be dealt with analytically and Eq. (11) to (15) are replaced with

$$\lim_{q \to \infty} \tilde{I}(q) = K'_P q^{-3} \quad (19)$$

$$K'_P = I_e(q) \pi^2 (\Delta\rho_e)^2 S_T \quad (20)$$

$$\tilde{Q} \equiv \int_0^{\infty} q\tilde{I}(q) dq$$

$$= 2Q = 4\pi^2 I_e(q) V (\Delta\rho_e)^2 \phi_1 (1 - \phi_1) \quad (21)$$

$$\hat{S} = 4\phi_1(1 - \phi_1) \lim_{q \to \infty} \left[q^3 \tilde{I}(q)\right] / \tilde{Q} \quad (22)$$

where the tilde ($\sim$) denotes smeared quantities measured with slit collimation. Unfortunately, for polymer systems one sometimes must go to such large values of $q$ that the infinite slit height approximation does not hold for the high $q$ tail of the curve (although it may still be appropriate for the data near the primary beam). In this case one may turn to various published routines for treatment of the detailed smearing problem. These have been reviewed by Glatter.[34]

## 2. Analyzing Deviations from Porod's Law

Very few experimental systems are found to follow the expressions corresponding to Porod's ideal two-phase system, and plots of $q^4 I(q)$ vs. $q$ (or $q^2$) are found to increase slightly or decrease slightly with $q$. These observed deviations are referred to as "positive" and "negative", respectively. In fact, however, more than one structural variation from Porod's assumptions may be present for any given sample, some of which cause positive deviations and some which cause negative ones. The four causes of deviations are fluctuations in electron density within a phase, interface roughness, interface curvature, and gradual electron density variation across the interface. Generally detailed study of these deviations for polymer systems attempts to minimize the influence of three effects on the data so that the magnitude of the fourth may be inferred.

### a. Fluctuations

Fluctuations in the electron density of a given phase cause positive deviations;[35] the intensity at large angles falls somewhat more slowly than expected from the Porod model. Often it will be necessary to remove the fluctuation scattering from the data before considering the form of the interface. A variety of methods for this subtraction, using different functional expressions to approximate the form of the fluctuation scattering, have been presented in the literature.[34-37,39,40]. These methods, and their relative merits have been reviewed by Koberstein et al.[39] and Shilov et al.[41] These authors also consider different model profile forms to use in analyzing the fluctuation corrected data. Only a brief discussion is presented here.

For the purposes of subtracting the fluctuation contribution, the overall intensity in the Porod region is envisioned to contain a fluctuation term

$$I_{\text{expt}}(q) = K_P q^{-4} + I_f(q) \quad (23)$$

where $I_f(q)$ has one of the forms

$$I_f(q) = \text{const} \quad (24)$$

$$I_f(q) = a \exp(bq^2) \quad (25)$$

$$I_f(q) = a + \Sigma b_n q^n \quad (26)$$

The first form was suggested by Ruland[35] and Bonart and Müller,[36] the second and third by Ruland[38] and Vonk,[37] respectively. Vonk[37] and Roe[40] have demonstrated that the choices of form represented by Eq. (25) or (26) are nearly equivalent for practical purposes. An example of fitting the background using Eq. (26) is given in Figure 4B. Much more critical than this choice of functional form is the proper determination of the absolute magnitude of the fluctuation scattering component.

### b. Roughness

A second cause of deviations is interfacial roughness; i.e., the change in electron density across the interface may be abrupt, but the contour of the interface is not smooth. Auvray and Auroy[31] point out that in this case the amount of interfacial area observed depends on the scale of observation, which varies as $q^{-1}$. They show that the differential cross-section from a sample containing objects of size $R$ may be approximated in the range of $q$ for which $q^{-1} < R$ by

$$\frac{d\sigma}{d\Omega}(q) \sim \frac{1}{a^6}\frac{\sum(q^{-1})}{q^4} \qquad (27)$$

where $a$ is the size of the effective scattering entities. The dependence on the degree of roughness is captured in $\Sigma(q^{-1})$, the amount of apparent area seen at the resolution $q^{-1}$. This is Porod's law with a surface area factor which continually changes as one moves through $q$.

In order to obtain more detailed expressions for the asymptotic behavior of $S(q)$ it is necessary to consider specific types of roughness. Of greatest applicability are models which envision the roughness as randomly distributed. For these the asymptotic form of the structure factor can be worked out in the Born approximation in certain specific cases for both normal and grazing incidence. We consider $q$ large enough that we may consider the interfaces to be flat locally, though not smooth on a length scale $\leqslant 1/q$. One may then envision an interface such as that sketched in Figure 5, for which the height deviations $[z(x', y') - z(x, y)]$ with respect to the average smooth interface is a Gaussian random variable. The distribution of this deviation we assume depends only on the relative position $(X, Y) = (x' - x, y' - y)$ and thus the interface roughness may be described by a function

$$g(X, Y) = \langle [z(x', y') - z(x, y)]^2 \rangle \qquad (28)$$

which represents an averaging over all pairs of points on the interface whose $(x, y)$ coordinates are separated by $(X, Y)$.

One specific type of roughness for which $\bar{S}(q)$ may be calculated is that characterizing a self-affine interface,[139] which is described by

$$g(X, Y) = g(R) = AR^{2h} \qquad (0 < h < 1) \qquad (29)$$

where $R \equiv (X^2 + Y^2)^{0.5}$. Such interfacial texture is thought to be a good model for various kinds of real interfaces. The exponent $h$ is a measure of "jaggedness," with smoother interfaces characterized by larger values of $h$. At sufficiently large distances this interface will appear smooth, but at length scales smaller than a crossover length, $R_0$, where

$$R_0 \equiv A^{1/2(1-h)} \qquad (30)$$

the interface looks like a fractal surface. $\bar{S}(q)$ is found to show two regimes of power law

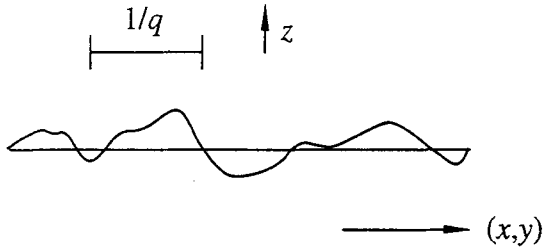


**FIGURE 5.** Schematic of a surface which is not smooth on a length scale $\leqslant 1/q$ and the corresponding average surface, which is taken to be the $(x, y)$ plane.

behavior,[139,140] varying as $q^{-(3+h)}$ in the asymptotic limit

$$\bar{S}(q) \approx \frac{A_1}{q^4} + \frac{A_2}{q^{3+h}} \tag{31}$$

with

$$A_1/A_2 = c(R_0)^{1-h} \tag{32}$$

and $c$ a constant of order unity.

Another important special case is that of a self-similar or fractal surface, which was discussed first by Bale and Schmidt.[33] In this case, the asymptotic form of $\bar{S}(q)$ is given by $\bar{S}(q) \sim D_s^{-6}$, where $D_S$ is the fractal dimension of the surface. Scattering from this interface type also falls off more rapidly than $q^{-4}$, and Sinha et al.[139] point out that in practice it may be difficult to distinguish the self-affine from the truly self-similar interface, as one should have data accumulated from over several decades of $q$ to do this.

### c. Curvature

A third interfacial parameter which may affect the asymptotic SAXS behavior is interfacial curvature, which becomes important when the curvature is of the same order of magnitude as $q$. In this case the equation for the pinhole collimated intensity, Eq. (11) becomes[32]

$$I_{exp\,t}(q) = I_e(q)2\pi(\Delta\rho_e)^2 S_T \left\{ \frac{1}{q^4} + \frac{1}{q^6} \cdot \left[ \frac{1}{4}\langle (C_1 + C_2)^2 \rangle + \frac{1}{8}\langle (C_1 - C_2)^2 \rangle \right] \right\} \tag{33}$$

where $C_1$ and $C_2$ are the local principal interfacial curvatures and the averages $\langle\ \rangle$ are taken over the entire interfacial area. The curvature correction to Porod's law varies as $q^{-6}$ and is always positive. Thus, if a sample contains a dispersed phase presenting sharp and locally smooth boundaries, the so-called Porod plot of $q^4 I(q)$ vs. $q$ will contain a bump or maximum at a value of $q$ below that at which the canonical Porod $q^{-4}$ asymptotic behavior is reached. Auvray and Auroy[31] point our that in the special case of a dilute monodisperse spherical dispersed phase $I(q)$ has the form

$$I(q) = I_e(q)2\pi(\Delta\rho_e)^2 S_T \cdot \left[ \frac{1}{q^4} + \frac{1}{q^6 R^2} + \text{oscillating terms} \right] \tag{34}$$

where $R$ is the sphere radius, and the curvature correction is clearly seen. For this case a maximum in the Porod plot occurs at roughly $q_P = 3/R$. For other, less well-defined dispersed phase geometries the value of $q_P$ also provides a clue to the interfacial curvature, although not as precisely defined.

### d. Finite Interface Width

The existence of smooth, gradual transitions in electron density normal to the phase boundaries rather than abrupt changes is the fourth important effect[35] that can cause deviations from the simple $q^{-4}$ Porod law behavior. Such profiles may be characterized using a nominal interface "width", $E$, defined as

$$E \equiv (\rho_1 + \rho_2)(d\rho(x)/dx)^{-1} \tag{35}$$

and illustrated in Figure 6 for a system that has fluctuations within the two phases as well. In this case[139] the orientation averaged structure factor, $\bar{S}(q)$, for pinhole collimation has the asymptotic form $q^{-4}|f(q)|^2$ where $f(q)$ is an effective form factor for the electron density variations:

$$f(q) = \int_{-\infty}^{\infty} \left[ \frac{d\rho_e(z)}{dz} \right] e^{-iqz} dz \tag{36}$$

This form will generally correspond to the intensity at large $q$ falling faster that $q^{-4}$. Information on the interphase width may thus be derived, in principle, from observed devia-

tions from Porod's law. However, the effect of interface width will be convoluted with those due to scattering length density fluctuations, roughness, and curvature. One may ask if, in fact, it is possible to separate these various effects and generally it is. Laterally rough and diffuse interfaces may be distinguished[139] in that the first leads to scattering which falls off more slowly than $q^{-4}$, while the latter yields scattering dropping off more rapidly than $q^{-4}$.

Detailed study of the interface width requires that the effects of fluctuations, roughness, and curvature be dealt with first. Curvature effects generally may be avoided simply by pursuing the measurement to sufficiently large values of $q$. Scattering attributable to fluctuations is then subtracted from the overall intensity.

The first method of estimating the interfacial width from fluctuation corrected data relies on comparisons of the data with model expressions incorporating smooth interfacial profiles. If the profile is described as a step function convoluted with a smearing function $h(r)$ such as illustrated in Figure 6, the fluctuation corrected intensity $I_{corr}(q)$ may be written as[35]

$$I_{corr}(q) = I_0(q)H^2(q) \qquad (37)$$

$I_0(q)$ is the intensity which would be scattered by an ideal system with sharp boundaries and $H^2(q)$ is the Fourier transform of the autocorrelation of the smearing function. (Expressions in the original papers are given in terms of a scattering vector $s = q/2\pi$.) $H^2(q)$ will have different forms depending on the profile envisioned. The most widely considered smearing function is the Gaussian shown in Figure 6

$$h(r) = \left(\frac{1}{2\pi\sigma^2}\right)\exp\left(-\frac{r^2}{2\sigma^2}\right) \qquad (38)$$

for which

$$H^2(q) = \exp(-\sigma^2 q^2) \qquad (39)$$

and the width $E$ is related to $\sigma$ by $E = \sqrt{12}\,\sigma$.

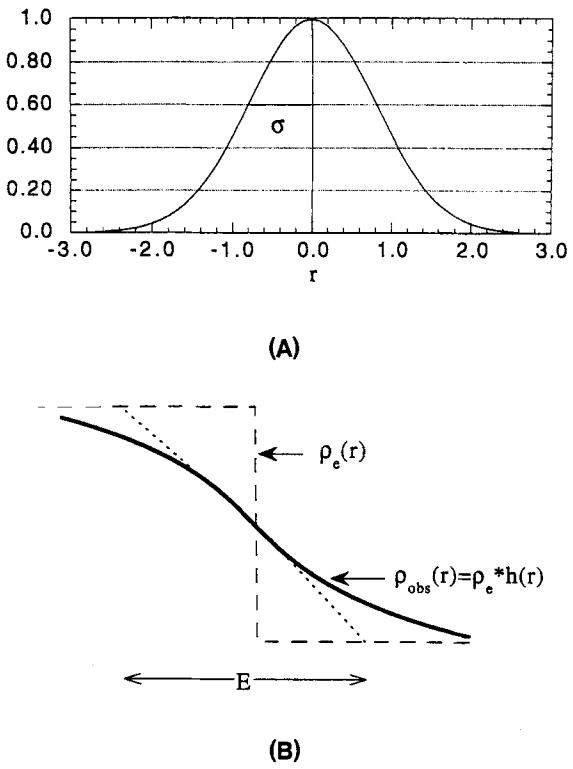


**FIGURE 6.** (A) A Gaussian smearing function of standard deviation $\sigma$ and (B) the corresponding broad interface electron density profile.

The corresponding expression for the asymptotic behavior in the case of point collimation becomes

$$\lim_{q\to\infty} I = K_P q^{-4}\exp(-\sigma^2 q^2) \qquad (40)$$

and therefore the value of $\sigma$ may be determined graphically from a plot of $\ln[q^4 I(q)]$ vs. $q^2$. Because the expression for $I$ at large $q$ is exact in this case, the only limitations on this analysis are two that always apply. First, the range of $q$ used for the determination must be sufficiently large to allow the slope and intercept to be properly estimated. Second, the minimum $q$ included must be large enough that the asymptotic expression is a good approximation to the data. Other approaches based on expansions of the exponential in Eq. (40) for $\sigma q/2\pi \ll 1$ are correspondingly limited in application.[39] Care also must be taken in considering systems for which $E$ represents a substantial fraction of a domain dimension, e.g., weakly segregated

block copolymers, or when the interfaces are highly curved, e.g., spherical domains in ordered asymmetric block copolymers.

In the case that the infinite slit approximation holds, the smeared intensity of the sigmoidal interface becomes[35]

$$\tilde{I}(s) = (K'_P/q^3)\left[(1 - 2\sigma^2q^2)erfc(\sigma q) + \frac{2}{\sqrt{\pi}}\sigma q\exp(-\sigma^2q^2)\right]$$

$$K'_P = W_l(0)K_P\pi/2 \tag{41}$$

where $W_l(0)$ is the constant value of weighting function $W_l(u)$. Linear regression analysis is aided by approximating this analytical result by[39,52]

$$\tilde{I}(q) \cong (K'_P/q^3)\exp\left[-1.36(\sigma q)^{1.81}\right] \tag{42}$$

and then considering the variation of $\ln[q^3\tilde{I}]$ with $q^{1.81}$. $E$ is given by $\sqrt{12}\,\sigma$ with

$$\sigma = \left(\frac{-\text{slope}}{1.36}\right)^{1/1.81} \tag{43}$$

$$K'_P = \exp(\text{intercept}) \tag{44}$$

where slope and intercept refer to a best fit line to the data. If one requires a precision of $\pm 5\%$ in $E$ this approximation scheme of Siemann and Ruland[52] and Koberstein et al.[39] is applicable for $0.056 < \sigma q < 8.54$. All other approaches discussed in the literature have considerably more limited ranges of application.

Because real slit collimated experimental setups may not justify use of the infinite slit approximation in the Porod region, it is also instructive to consider how a finite beam height may be taken into account using a Gaussian distribution for $W_l(u)$

$$W_l(u) = W_l(0)\exp(-p^2u^2)$$

as discussed by Koberstein et al.[39] The expression for the asymptotic behavior becomes in this case

$$\tilde{I}(q) = \left(\frac{K'_P}{q^3}\right)\exp\left(\frac{p^2q^2}{4\pi^2}\right)\cdot\left[(1 - 2\alpha^2q^2)erfc(\alpha q) + \frac{2}{\sqrt{\pi}}\alpha q\exp(-\alpha^2q^2)\right] \tag{45}$$

$$\alpha = \left[\sigma^2 + (p/2\pi)^2\right]^{0.5} \tag{46}$$

which may also be approximated as above to yield

$$\lim_{q\to\infty}\left[\tilde{I}(q)\exp\left(-\frac{p^2q^2}{4\pi^2}\right)\right] \approx (K'_P/q^3)\exp\left[-1.36(\alpha q)^{1.81}\right] \tag{47}$$

This expression yields the result given in Eq. (40) for the limiting case of infinite slit height, for which $p$ goes to zero.

Perhaps the most important aspect of the Porod region analysis is its tremendous sensitivity to the subtraction of background and fluctuation scattering. Siemann and Ruland[52] demonstrated in an investigation of styrene-isoprene triblock copolymer interfaces variations in $E$ of $\pm 40\%$ when the fluctuation background intensity used is altered by only $\pm 2\%$. Ruland[44] has also recently shown that if the diffuse interface is not a smooth density transition but rather a sharp interface with a statistically varying position above and below the average interface position, $E$ may be underestimated substantially. Orientation of the interfaces, such as has been done in diblock copolymer systems,[53,54] may be used to minimize this error. Intensity measurements along a specific axis in reciprocal space then provide information on the coarseness of the interfaces.

### 3. Correlation Function Analysis

A second type of method for analyzing small angle transmission data for interface

width involves first Fourier transforming the data to obtain the correlation function, $\gamma(r)$.[37,55] The correlation function presents in real space all the model independent information about the sample structure that is available from the scattering data. Consideration of the detailed form of $\gamma(r)$ for a two-phase structure reveals that the slope of $\gamma(r)$ should be constant and nonzero as $r$ approaches zero if the interface is infinitely sharp, while for any real system with finite interface width, $d\gamma(r)/dr$ is constant over some range of $r$ only for sufficiently large values of $r$, as shown in Figure 7. The value of $r$ at which the constant slope is attained may be related to the interface width.

The Fourier transform technique has not found wide acceptance for two reasons. First, the procedure of Fourier transformation is a nontrivial analysis step. Second, while qualitative comparisons of interface width among different samples may be made without resorting to detailed models of the interface profile, one must still invoke a model to obtain quantitative comparisons.

#### 4. Sandwich Technique

A third technique for judging interface width exploits the increased sensitivity that can be obtained simply by greatly increasing the area of interface in the sample and observing the variation in the invariant, $Q$, with interface change. This technique has been used by research groups with both neutron and X-ray small angle scattering to study the phenomenon of polymer interdiffusion.[45-50] Samples with many parallel layers ("sandwich" geometry) as well as discrete latex spheres have been used with neutrons. Although preparation of the multilayered samples is quite tedious, deuteration of one component provides excellent neutron scattering contrast while maintaining miscibility of the components at annealing temperatures. Unfortunately, pairs of polymer components displaying good X-ray contrast tend to be immiscible, limiting the potential use of this technique with X-rays. The author is aware of only one published X-ray transmission study[50] of this type with a polymer system. In that work the interdiffusion of poly(methyl methacrylate) (PMMA) and poly(vinylidene fluoride) (PVDF) is investigated. As neighboring layers become more highly interdiffused the scattering intensity increases initially as the total scattering length density fluctuations increase due to more contact between PMMA and PVDF segments.

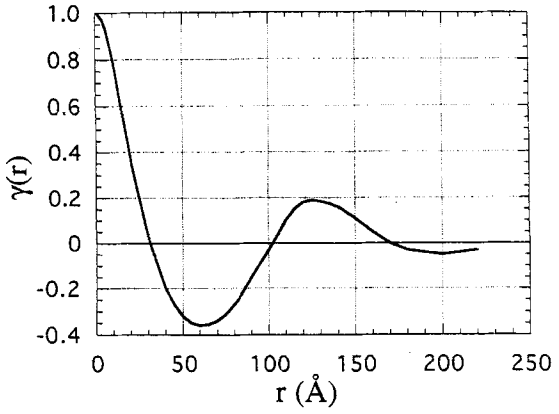


**FIGURE 7.** Effect of finite interface width on the correlation function $\gamma(r)$ near the origin.

### C. Instrumentation

The two primary distinctions among the various types of small angle cameras for interface study are the type of collimation (point or slit) and detector type (film, step counter, or position sensitive detector). Analysis of SAXS data for interfacial information necessitates measurements to comparatively large $q$ values (typically $2\theta = 6°$ to $8°$ for $CuK_\alpha$, $q = 0.85$ to $1.1$ Å$^{-1}$) with good statistics, so that good background subtraction may be done in the Porod region. This requirement recommends experimental setups with high intensity, low background, and good counting precision. However, one need not have outstanding spatial resolution in the Porod region. Both slit and point collimation devices have been used for polymer interface study. The slit collimation offers more intensity, for example, when working with sealed tube sources. In particular, the Kratky type

slit collimation has been used by several investigators.[51,52,56,57] This design offers good resolution and low parasitic scattering near the primary beam, as well as good intensity. However, one must account for smearing of the scattering pattern in the analysis and while analytical expressions exist for the "infinite slit" approximation, this limiting case is not always approached closely for larger $q$. Therefore, more complicated corrections may be needed.[39] Use of point collimation[58] avoids this difficulty. A detailed comparison of two cameras, one using a Kratky slit system and the other a more highly collimated beam, is presented by Todo et al.[58] in a discussion of interfacial width measurements.

Film detection,[20,59] while useful for survey measurements and investigations of sample orientation, has been superseded in Porod region measurements by counting techniques, [20,157] as they are more appropriate for the low intensities involved. Specifically, position-sensitive counters are particularly useful because, in contrast to step counters, they allow measurement of the entire Porod region simultaneously. This decreases measurement time and errors within a single curve due to primary intensity fluctuations. When using point collimation to avoid desmearing, a radial averaging over data from two-dimensional position-sensitive detectors may be used with isotropic samples to improve counting statistics.



### D. Sample Preparation

The important criteria SAXS samples must meet are appropriate size, proper thickness, thickness uniformity across the illuminated area, and an absence of colloidal-sized voids or contaminant particles. The amount of material required to make a sample will vary, in general, with the collimation used. Lower resolution or slit-type collimations, which optimize intensity, require more sample due to the larger illuminated area. A minimum area required for a Kratky camera measurement is about $1 \times 25$ mm$^2$, corresponding to about 25 mg of polymer (for 1-mm thickness). For ease of mounting, sample widths of 3 to 4 mm are more workable, but in any case the amount of material required is generally $< 300$ mg.

Competition between two dependencies of intensity on sample thickness dictate that an optimum thickness, $t_{opt}$, exists for each sample. The strength of the desired scattering signal increases linearly with thickness, while the transmission coefficient of the sample drops exponentially. Multiple scattering effects, which complicate the analysis, also become more prevalent as thickness increases. A simple optimization yields an expression for the optimal thickness of $1/\mu(l)$, where $\mu$ is the mass absorption coefficient of the material evaluated at the wavelength of interest (tabulated in Reference 60). For hydrocarbon polymers $t_{opt}$ is on the order of 2.5 mm, while for polymers containing atoms with high atomic number it may be as low as 0.1 mm. Nonuniformity in thickness will lead to distortions of the scattering pattern, while the presence of voids or foreign particles results in spurious additional scattering intensity, particularly at low $q$.

Sample preparation for SAXS measurements is generally less demanding than that for methods using grazing incidence. Surface roughness is not an issue and if point collimation is used, the area over which the sample faces must be plane and parallel is quite small. In addition, one may still obtain approximate results even when the faces are not plane. Finally, samples that flow (due to low molecular weight, high temperature, or high solvent content) may be studied with SAXS by mounting them in a closed chamber with windows that minimize the additional scattering and adsorption.

## III. GRAZING INCIDENCE METHODS

### A. General Features

In grazing incidence methods the orientation of the sample with respect to the primary beam is set so that the angle between the sample surface and incident beam, $\theta_0$, is no larger than a few degrees, as suggested schematically in Figure 8 for the simple case

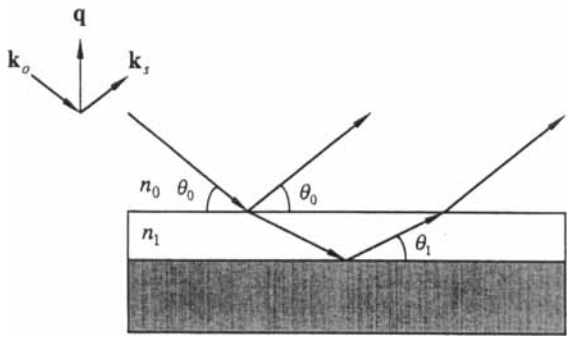


**FIGURE 8.** In a grazing incidence experiment the beam incident upon the sample at angle $\theta_0$ may be in general both partially transmitted through the interface and partially reflected. The transmitted beam is propagated at a grazing angle $\theta_1$ with respect to the surface and may be reflected from other interfaces in the sample, such as the film / substrate interface illustrated here. In this case the radiation reflected from the two interfaces interfere, yielding a distinctive pattern characteristic of the film thickness.

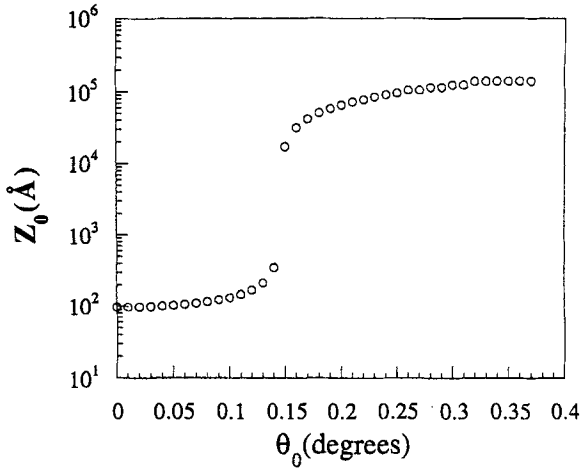


**FIGURE 9.** The characteristic penetration depth $z_0$ varies slowly with incident angle $\theta_0$ for $\theta \ll \theta_c$, but increases abruply at $\theta_c$ as shown here for a typical polymeric material and $CuK_\alpha$ radiation ($\theta_c = 0.15°$).

of a single interface. The interaction of the X-rays with the sample when striking it at small angles differs importantly in two ways from that at normal incidence. First, the penetration depth of the beam is limited because the distance the beam must travel to reach the other side of a sample of given thickness increases rapidly as $\theta_0$ decreases. The amplitude of the transmitted field, $E$, drops along the path through the sample and the structure is effectively probed only down to the depth at which $E$ drops to a threshold value. We choose as a convenient measure the depth, $z_0$, at which $E$ falls to $1/e$ times its incident value and we refer to this as the effective penetration depth. The strong dependence of $z_0$ on $\theta_0$ is demonstrated in Figure 9 for a beam of wavelength 1.54 Å incident upon a typical polymeric material from vacuum. In calculating this curve one must account for the fact that when the beam is transmitted through the interface it is refracted slightly toward the surface. This is because condensed matter always has a lower refractive index for X-rays than does air or vacuum.

The direction of the beam in the sample, specified by $\theta_1$ with respect to the interface, is given by Snell's law as:

$$\cos\theta_1 = (n_0/n_1)\cos\theta_0 \qquad (48)$$

where both the $n_i$ and $\theta_i$ have real and imaginary parts in the case of absorbing materials. As $\theta_0$ is decreased toward zero a critical value, $\theta_c$, is reached at which $\theta_1$ no longer has any real component, but is purely imaginary. There is no true "transmitted" beam but only an exponentially damped evanescent wave at the surface which penetrates a finite distance into the sample. The value of the critical angle for incidence from air or vacuum is given to a good approximation by

$$\theta_c = \sqrt{2\delta_1} \qquad (49)$$

where $\delta_1$ is the real component of the refractive index defined in Eq. (1). $\theta_c$ is on the order of 0.15° to 0.18° for typical polymers and $CuK_\alpha$ radiation. Note that while $z_0$ varies dramatically in a small region of $\theta_0$ about $\theta_c$, it closely approaches its minimum value for $\theta_0$ only slightly less than $\theta_c$. The change in direction that occurs upon refraction may also be described by changes in the $z$ component of the wave vector, $k_z$. In vacuum $n_0$ is unity and the magnitude of $k_z$ for

the incident beam is given by

$$k_{z,0} = 2\pi \sin(\theta_0)/\lambda \qquad (50)$$

The value of $k_z$ in the $i$th layer of a multilayer sample is given by

$$k_{z,i}\left(k_{z,0}^2 - k_{c,i}^2\right)^{0.5} \qquad (51)$$

where $k_{c,i}$ is the critical value of $k_z$ for the material in layer $i$. Eq. (50) and (51) also hold to a good approximation for incidence from dry air at standard temperature and pressure.

The second important effect of grazing incidence is that the intensities of radiation reflected and scattered from the surface of the sample become measurable. Whenever a beam strikes an interface some portion is reflected, but for normal incidence the reflected intensity is immeasurably small. The ratio of reflected to incident field amplitudes, or reflectance, $r$, of an ideally smooth, sharp interface between materials $i$ and $i + 1$, is given by

$$r = \frac{k_{z,i} - k_{z,i+1}}{k_{z,i} + k_{z,i+1}} \qquad (52)$$

where the $k_{z,i}$ are related by Eq. (51). Eq. (52) is rigorously correct only for radiation polarized in the direction perpendicular to the plane of incidence ("s" polarization). However, for X-ray wavelengths it provides an excellent approximation for unpolarized radiation over the range of $k_{z,0}$ of interest. In fact, polarization may be neglected safely in the discussion below. The ratio of reflected to incident intensities, $R$, at the surface of a single, ideal interface is given by an expression derived by Fresnel:

$$R \equiv \frac{I_0}{I_r} = rr^* = \left|\frac{k_{z,0} - k_{z,1}}{k_{z,0} + k_{z,1}}\right|^2$$

$$= \left|\frac{q_{z,0} - q_{z,i}}{q_{z,0} + q_{z,i}}\right|^2 = R_F(q_{z,0}) \qquad (53)$$

where $r^*$ represents the complex conjugate

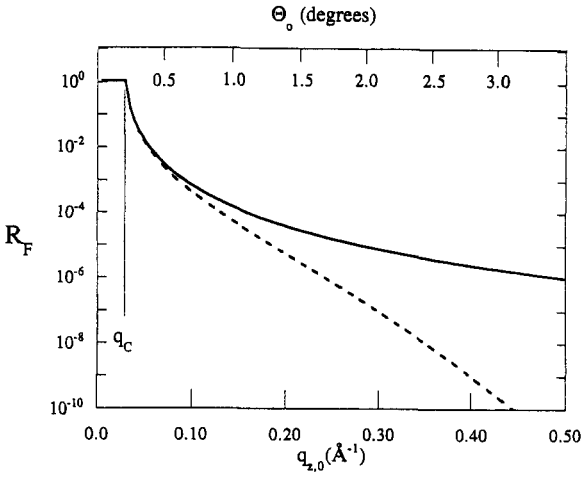


**FIGURE 10.** Variation of the Fresnel reflectivity of a single interface between air and silicon (solid line). Also shown is the reflectivity expected when microroughness with root mean square amplitude of 7 Å is added at the interface (dotted line).

of $r$ and $q_{z,0} = 2k_{z,0}$ is the magnitude of the scattering vector characterizing the reflected beam.

The form of $R_F(q_{z,0})$ is shown in Figure 10 for the case of an ideal air/silicon substrate interface. For $\theta \gg \theta_c$ one finds that $R_F$ decreases rapidly with $\theta$

$$R_F \propto \theta^{-4} \propto k_{z,0}^{-4} \propto q_{z,0}^{-4} \qquad (54)$$

just as does the small angle scattering intensity in the Porod region of SAXS in transmission mode. For $\theta_0 < \theta_c$, $R_F$ is nearly unity, falling short by a very small amount attributable to absorption in the surface region. The remarkable gain in reflectivity at grazing incidence is realized not only for the sample/air interface, but also for other interfaces within the penetration depth, meaning that beams reflected from interfaces some distance below the surface may contribute to the detected intensities. Information about the electron density in the neighborhood of these interfaces is therefore also available. It is because of the limited penetration depth and high reflectivities at low incidence angles that grazing techniques are particularly sensitive to near-surface structure.

For a real interface only a portion of the beam is reflected in the way described by the above equations. This radiation reflected in the plane of incidence at $\theta' = \theta_0$ is referred to as the "specular" beam. That portion of the incident intensity which is not reflected specularly is scattered by surface or subsurface structure or absorbed. All the phenomena occurring under grazing incidence, specular reflection, grazing incidence scattering, absorption, and fluorescence, provide opportunities to learn about the outer surface structure of the sample as well as interfaces within the sample. Information about these "buried" interfaces becomes available as the incident angle is increased above the critical value. Because it is generally difficult to gather at one time information from all the phenomena mentioned above, distinct experimental techniques have been developed for optimally exploiting each. The first of these techniques discussed is reflectometry. Second, diffuse specular scattering is considered. Within the realm of diffuse scattering two general measurement types exist. One type involves varying only the in-plane scattering vector while holding the penetration depth and $q_z$ constant. The final grazing incidence technique discussed considers the measurement of in-plane scattering far from the specular condition.



## B. Reflectometry

### 1. Introduction

X-ray reflectometry (XR) in its purest form considers only the specularly reflected radiation. A collimated beam strikes the surface at an angle $\theta_0$, and the reflected beam is observed with a detector lying in the plane of incidence at an angle $\phi$ with respect to the surface set equal to $\theta_0$. The detector angle with respect to the incident beam direction is then $2\theta$. In this case the momentum transfer vector, $\mathbf{q}$, has only a $z$ component and only the laterally averaged structural variations perpendicular to the surface are probed. In a typical experiment, reflected intensities are measured for a series of incident angles from nearly zero to a few degrees (the same angular range as for SAXS) by varying $\theta$ and $\phi$ symmetrically. Due to this symmetry it is equally convenient to discuss specular reflectivity using either $k_{z,0}$ or $q_{z,0}$ to specify the scattering geometry. In this section the latter variable will be used more frequently to facilitate comparison between equations for SAXS and XR. (When appearing without a subscript indicating the medium to which they pertain the variables $k_z$ and $q_z$ are assumed to refer to quantities in air or vacuum.) Later consideration of asymmetrical grazing incidence experiments will require the use of $k_{z,0}$ at certain points.

### 2. Analysis and Theory

#### a. Basic Concepts

The reflectivity, $R$, is defined in terms of total intensity while the scattering cross-section is defined in terms of the flux. In the case that $d\sigma/d\Omega$ has a specular part it is related to $R$ in the following way

$$R = \frac{1}{L_x L_y \sin\theta_0} \int \left(\frac{d\sigma}{d\Omega}\right)_{\text{spec}} d\Omega \quad (55)$$

where $L_x L_y$ is the area of the reference plane surface about which the sample surface fluctuates. The factor $1/\sin\theta_0$ accounts for the change in flux at the surface as $\theta_0$ is varied. For the grazing incidence geometry a normalized structure factor analogous to that introduced in Eq. (10) may be defined

$$S(\mathbf{q}) \equiv \frac{d\sigma}{d\Omega} \frac{1}{r_0^2 (\Delta\rho_e)^2 L_x L_y} \quad (56)$$

with the total surface area $S_T$ germane to the SAXS experiment being replaced by a reference surface $L_x L_y$. In general, the overall structure factor contains both specular and diffuse components, $S(\mathbf{q}) = S_{\text{spec}}(\mathbf{q}) + S_{\text{diff}}(\mathbf{q})$, with the specular part being that associated with delta functions in $q_x$ and $q_y$. Therefore, the reflectivity may also be ex-

pressed as

$$R = \frac{r_0^2(\Delta\rho_e)^2}{\sin\theta_0}\int S_{\text{spec}}(\mathbf{q})\,d\Omega \qquad (57)$$

Often a great deal may be learned about a sample simply by studying the raw reflectivity profile and making a few simple calculations. General features key to this preliminary analysis can be highlighted by considering the reflectivity of three example systems: a single air/substrate interface, a homogeneous thin film, and a periodic multilayer. The first important characteristic of the reflectivity to note is the critical value, $q_c$, associated with the rapid dropoff in reflectivity with $q_{z,0}$. Typically polymer samples will be mounted on substrates having electron densities higher than that of the polymer so that the dropoff is readily associated with the substrate. Roughness or diffuseness at an interface will decrease its reflectivity relative to that of a sharp, smooth interface,[68] as demonstrated in Figure 10 for the case of the air/silicon substrate interface, with the deviation growing more pronounced with increasing $q_{z,0}$. Thus, an experienced user may obtain some clue to overall roughness when comparing samples of similar makeup by noting for each the reflectivity at a reference value of $q_{z,0}$.

Addition of an organic film atop a substrate adds two new features to the sample reflectivity, modulations at $q_{z,0}$ below the sharp dropoff in reflectivity and interference fringes. Both are seen in data from a polystyrene film on float glass shown in Figure 11. Once $q_{z,0}$ exceeds the critical value of

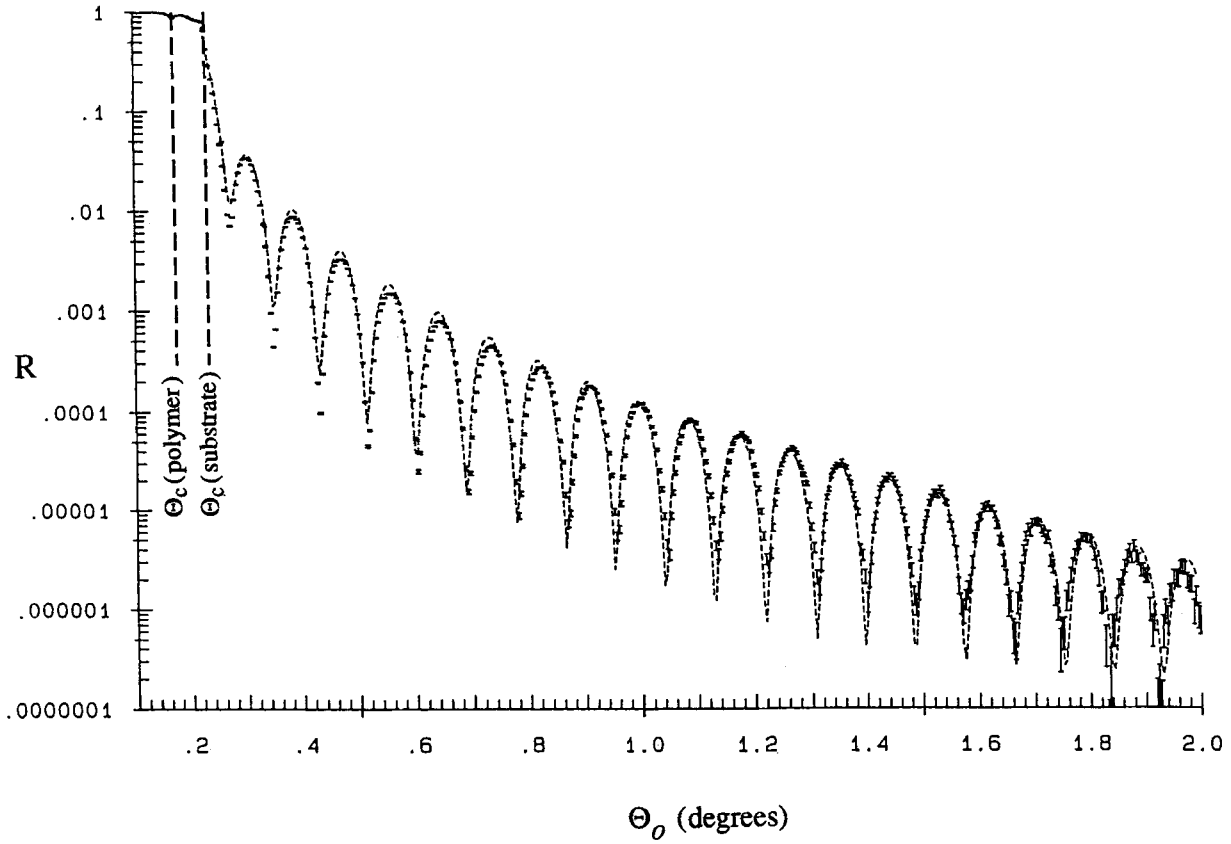


**FIGURE 11.** Experimental reflectivity data for a polystyrene film spun cast on float glass as measured by Foster et al.[74] The Kiessig fringes are well represented by a model calculation, shown as the dashed curve, which assumes a film thickness of 493 Å, average film density of 1.05 g / cm$^3$, air / polymer interface root mean square (rms) roughness of 3 Å and polymer / substrate roughness of 6 Å rms.

the film, a portion of the beam will be transmitted through the film and reflected at the polymer substrate interface as pictured in Figure 8. If the substrate has a higher electron density than that of the film, which is generally the case, this transmitted beam will be nearly totally reflected at the polymer/substrate interface when $q_{c,poly} < q_{c,sub}$. However, absorption in the film attenuates the intensity slightly and because this attenuation increases with film thickness, its magnitude allows an approximate thickness determination.

Interference of the beams reflected at the two interfaces results in a modulation of the Fresnel curve both below and above the substrate $q_c$ to form "Kiessig fringes", named after H. Kiessig, who first observed such fringes with metal films.[61] The thickness of the film, $d$, may be readily estimated from the spacing of two successive minima, $\Delta q_{z,1}$, in a fashion that is independent of the refractive index of the film[15]

$$d = 2\pi/\Delta q_{z,1} \propto 2\pi/\Delta q_{z,0} \qquad (58)$$

The strength of these oscillations increases with the magnitudes of the electron density jumps $\Delta\rho_e$ at the air/polymer and polymer/substrate interfaces. However, diffuseness at one or both of the interfaces will generally reduce the oscillation amplitude and cause it to decrease with increasing $q_{z,0}$, although if the roughnesses of two interfaces are well correlated,[62] deep minima may still be observed. Existence of oscillations over a large $q_{z,0}$ range suggests that the sample has uniform thickness and well-defined interfaces.

Samples with structures that vary periodically in the $z$ direction, such as ordered block copolymer films and Langmuir-Blodgett multilayers, will yield reflectivity spectra containing Bragg peaks. These are due to construc-

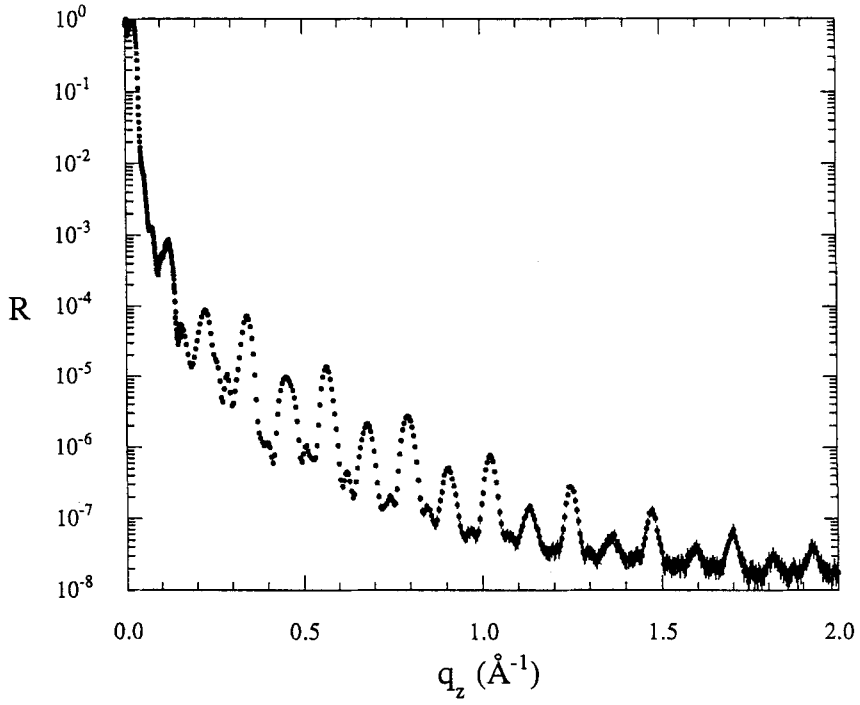


**FIGURE 12.** The very regular structure of a Langmuir-Blodgett multilayer[108] containing layers of both cadmium arachidate and a polyglutamate copolymer yield many orders of Bragg peaks in the measured reflectivity. Background and diffuse scattering have not been subtracted here.

tive interference of beams reflected from the periodic structure. Figure 12 presents an example of a Langmuir-Blodgett film. If the characteristic spacing, $D$, of the periodic structure differs sufficiently from other important dimensions in the system, the positions and shapes of the Bragg peaks may be analyzed to infer the periodic spacing. The first peak position, $q^*_{1,\text{expt}}$ is related to $D$ by

$$D = \frac{2\pi}{q^*_{1,\text{corr}}} \tag{59}$$

where $q^*_{1,\text{corr}} \equiv \sqrt{q^{*2}_{1,\text{expt}} - q^{*2}_c}$ is a peak position corrected for the shift caused by the total reflection region. The peak heights and breadths are related to the number of periods present and the perfection of their ordering. Peak intensities drop and the peaks broaden when the number of periods is reduced to only a few, or when the ordering is imperfect.

Overall film thickness, average electron density, characteristic spacings of periodic structures, and approximate thicknesses of other key structural components may all be derived from reflectivity data without detailed analysis under proper conditions. Further information, particularly on interfacial profiles in the sample, can be properly gained only from a more involved analysis. First, the data must be corrected by subtracting contributions from background as well as diffuse scattering in the specular direction. While the background is largely dependent on experimental conditions, the diffuse scattering is sample dependent, as discussed below. For samples with very rough or textured surfaces, the diffuse scattering generally will be significant, particularly at higher $q$. After correction the data may be analyzed rigorously as specular intensities using the techniques outlined briefly below. As no commercial analysis software is available that is generally applicable to the analysis of polymer samples, the novice user will need to code his own or adapt that from other users or both. While scientifically mundane, the implementation of a reliable analysis package requires a nontrivial effort, and a few points of particular concern are highlighted.

Two primary classes of techniques are available for the analysis of specular reflectivity data. The first, more common class, involves simulating the reflectivity from a candidate model structure and varying the model parameters by means of nonlinear regression to obtain the best possible agreement between simulated and measured reflectivity. In the second class, a reduced reflectivity is considered to gain insight into the square of the electron density gradient's Fourier transform.[64-66,77] This second class of techniques is not addressed further here.

Central to the model-dependent regression techniques is a method for calculating the reflectivity curve from a given model; this method can take one of three forms. Important to two of these three calculational formalisms is the concept that the reflectivity from an arbitrarily complex electron density profile may be calculated to a sufficiently good approximation from a discretized version of the electron density profile. That is, the real structure is approximated as a stack of $N$ homogeneous layers of thickness, $d_i$ and electron density, $\rho_{e,i}$, such that the $\rho_e$ profile through the stack approximates the continuous profile as shown in Figure 13. Should the discretization chosen be too coarse, the calculated reflectivity contains artifacts (see demonstration in Russell's review[18]). Indiscriminate reduction of the step size, on the other hand, leads to artifacts due to machine roundoff error and unnecessary computational cost. An appropriate compromise depends upon the sharpness of features in the "true" profile and the range of $q$ to which $R$ must be calculated, i.e., the resolution required. Higher resolution of sharper features necessitates a finer discretization. The consideration of microscopic roughness and instrumental resolution, which is always necessary for real samples, is discussed below after the basic methods are introduced using the simpler case of ideal interfaces and perfect collimation.

In the first calculational scheme for the regression technique[71] the reflectance and

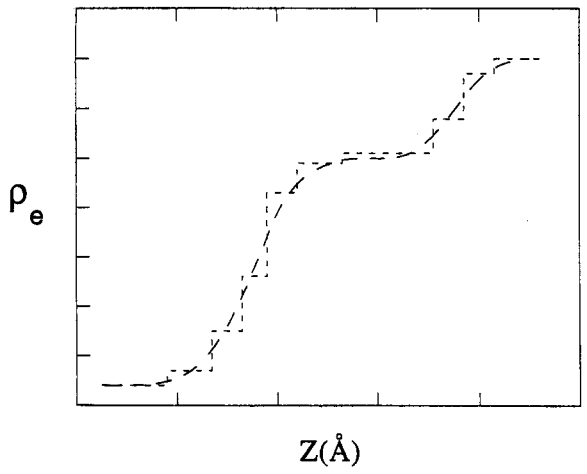


**FIGURE 13.** The reflectivity from a sample characterized by a smoothly varying electron density profile may be calculated by first approximating the continuous function by a discretized profile, as suggested here schematically.

transmittance at each interface in the discretized structure are calculated recursively starting with the layer/substrate interface. The reflectance at that interface is that given by Eq. (52). This result is used to solve the general recursive equation

$$r_{i-1,i} = \frac{r'_{i-1,i} + r'_{i,i+1}\exp(2id_ik_{z,i})}{1 + r'_{i-1,i}r'_{i,i+1}\exp(2id_ik_{z,i})} \quad (60)$$

involving the thickness of the $i$th layer, $d_i$, and the reflectance $r'_{i,i+1}$ caculated from Eq. (52). Eq. (60) is solved first at the $(N-1)/N$ interface and then on up through the layers to the air/sample interface. The overall sample reflectivity is obtained as the modulus of the air/top layer reflectance.

In the second calculational scheme[63] an optical transfer matrix formalism is used. The optical characteristics of any single layer $i$ are summarized in a matrix $\mathbf{M}_i$ which contains the coefficients of two simultaneous linear differential equations linking the amplitude of the electromagnetic field in the layer and its derivative. In principle, any form of refractive index profile through the layer for which the equations may be solved analytically, e.g., constant or linear, may be chosen. In practice, the layer profile is generally assumed to be constant, yielding

$$\mathbf{M}_i = \begin{bmatrix} m_{11,i} & m_{12,i} \\ m_{21,i} & m_{22,i} \end{bmatrix} = \begin{bmatrix} \cos(k_{z,i}d_i) & \sin(k_{z,i}d_i)/k_{z,i} \\ -k_{z,i}\sin(k_{z,i}d_i) & \cos(k_{z,i}d_i) \end{bmatrix} \quad (61)$$

If this single layer is resting on a substrate characterized by $k_{c,N+1}$, the reflectance of the supported film is given by

$$r_i = \frac{k_{z,0}k_{z,N+1}m_{12} + m_{12} - ik_{z,N+1}m_{11} + ik_{z,i}m_{22}}{k_{z,0}k_{z,N+1}m_{12} - m_{21} + ik_{z,N+1}m_{11} + ik_{z,0}m_{22}} \quad (62)$$

The reflectance of a stack of uniform layers, such as represented by our discretized profile, may be found simply by first multiplying the transfer matrices of all $N$ layers to form the transfer matrix of the total film, $\mathbf{M}_T$

$$\mathbf{M}_T = \mathbf{M}_1\mathbf{M}_2 \ldots \mathbf{M}_N \quad (63)$$

and calculating $r$ as in Eq. (62) using the elements of $\mathbf{M}_T$. The reflectivity obtained as $rr^*$ is that which one would measure in an ideal experiment with perfect collimation and a single wavelength of incident radiation.

The third formalism for calculating the model reflectivity involves simplifying the problem by assuming that the scattered and reflected fields are always of negligible magnitude compared to the incident field. This corresponds to the Born approximation and this approach is acceptable for $q \geqslant 4q_c$ and for samples containing no large electron density gradients. Near $q_c$ the assumptions required clearly do not hold. The reflectivity averaged over the coherence of the beam is given by[146]

$$R(q_z) = R_F(q_z)\left|\frac{1}{\rho_s}\int_0^\infty dz\, e^{iq_zz}\frac{\partial\rho(z)}{\partial z}\right|^2 \quad (64)$$

where $\rho_s$ is a reference electron density, e.g., that of the substrate. The beauty of this approach is that contributions of various

structural features to the reflectivity often may be explicitly separated and studied as demonstrated below.

### b. Roughness Effects

Accounting rigorously for interfacial microroughness in calculations of specular reflectivity is an important issue that has been addressed in a detailed way[73,134-142] by a number of authors. Pynn[142] discusses the connections among the various approaches that have been used. We present here an overview for the randomly rough interfaces introduced above, considering first the roughness corrections calculated in the Born approximation and then in the distorted wave Born approximation (DWBA). Two common computational approaches for including these effects in data analysis are summarized and their limits of applicability highlighted.

In deriving the reflectivity from the random, isotropic interface with Gaussian distributed heights $z(x, y)$ shown in Figure 5, we proceed from Eq. (9). For the grazing incidence geometry the average smooth interface, $S_0$, associated with rough interface is conveniently taken to be the $(x, y)$ plane. If we describe our interface with $g(x, y)$ defined in Eq. (24) and consider an area $L_x L_y$ of the reference plane, the structure factor, including both specular and diffuse components,[139] is

$$S(\mathbf{q}) = \frac{1}{q_{z,0}^2} \iint_{S_0} dX\, dY e^{-q_{z,0}^2 g(x,y)/2} e^{-i(q_x X + q_y Y)} \tag{65}$$

Sinha et al.[139] discuss the special case of the self-affine random interface described by Eq. (29). If there is no finite value of $R$ for which $g(R)$ goes to zero, the mean square roughness $\langle z^2 \rangle$ is not defined, and if one neglects instrumental resolution effects $S(\mathbf{q})$ has no specular component. However, strong diffuse scattering is found in the specular direction. The power law dependence of this scattering varies with $h$

$$[S_{\text{diff}}(\mathbf{q})]_{[q_x = q_y = 0]} = \frac{2\pi Q_h(A)}{q_z^{2+2/h}} \tag{66}$$

with

$$Q_h(A) = \int_0^\infty d\xi\, \xi e^{-(A/2)\xi^{2h}} \tag{67}$$

and differs from that seen for the orientationally averaged scattering observed with SAXS in Eq. (31). If there is a very long length-scale cutoff for $g(R)$,[139] a power law dependence involving $h$ will still be observed in the specular direction.

In experimental systems $\langle z^2 \rangle = \sigma^2$ does have a well-defined value due to finite sample size or other reasons. Therefore, we may rewrite Eq. (65) in terms of the height-height correlation function $C(X, Y)$ and mean square roughness by noting that[139]

$$g(X, Y) = 2\langle z^2 \rangle - 2\langle z(X, Y) z(0, 0) \rangle \tag{68}$$

and

$$\begin{aligned} C(X, Y) &\equiv \langle z(X, Y) z(0, 0) \rangle \\ &= \sigma^2 - \tfrac{1}{2} g(X, Y) \end{aligned} \tag{69}$$

so that

$$S(\mathbf{q}) = \frac{e^{-q_{z,0}^2 \sigma^2}}{q_{z,0}^2} \iint_{S_0} dX\, dY e^{q_{z,0}^2 C(X,Y)} e^{i(q_x X + q_y Y)} \tag{70}$$

The function $g(R)$ may now be modified to include an effective cutoff length $\xi$

$$g(R) = 2\sigma^2 [1 - e^{-(R/\xi)^{2h}}] \tag{71}$$

and a truly specular component in $S(\mathbf{q})$ is recovered

$$S_{\text{spec}}(\mathbf{q}) = \frac{4\pi^2}{q_{z,0}^2} e^{-q_{z,0}^2 \sigma^2} \delta(q_x) \delta(q_y) \tag{72}$$

Integrating in the right-hand side of Eq. (57) and noting that

$$d\Omega = \frac{dq_x\, dq_y}{k_0^2 \sin\theta_1} \tag{73}$$

with $k_0 \equiv \dfrac{2\pi}{\lambda}$ we obtain for $q_{z,0} \gg q_c$

$$R(q_{z,0}) \approx \frac{16\pi^2 r_0^2 (\Delta\rho_e)^2}{q_{z,0}^4} e^{-q_{z,0}^2\sigma^2} \tag{74}$$

At large $q_{z,0}$, where this expression is applicable, it is equivalent to

$$R(q_{z,0}) = R_F(q_{z,0}) e^{-q_{z,0}^2\sigma^2} \tag{75}$$

While Eq. (74) clearly fails at small $q_{z,0}$, it is readily handled computationally.

The Born approximation analysis may also be applied in the case that the interface is not sharp and rough, but rather diffuse; i.e., the $\rho_e$ profile through the interface is everywhere a smooth function. In this case[135] the reflectivity at large $q_z$ is given by

$$R(q_{z,0}) = R_F(q_{z,0}) \left| \frac{1}{\rho_{N+1}} \int dz \frac{\partial\rho_e(z)}{\partial z} e^{-iq_{z,0}z} \right|^2 \tag{76}$$

where $\rho_{N+1}$ is the value of $\rho_e$ for the substrate. For a sharp interface $\partial\rho_e(z)/\partial z$ is a delta function. A diffuse air/sample interface is typically assumed to have an error function shape,[138] with width characterized by $\sigma$,

$$\rho_e(z) = \rho_0 + (\rho_1 - \rho_0) erf(z, \sigma) \tag{77}$$

with $\rho_1$ as the electron density of the sample. The error function is defined as

$$erf(z, \sigma) = \frac{1}{\sigma\sqrt{2\pi}} \int_{-\infty}^{z} \exp\left(\frac{-\zeta^2}{2\sigma^2}\right) d\zeta \tag{78}$$

Then, $\partial\rho_e(z)/\partial z$ is given by

$$\frac{\partial\rho_e(z)}{\partial z} = \frac{\rho_1 - \rho_0}{\sigma\sqrt{2\pi}} \exp\left(\frac{-z^2}{2\sigma^2}\right) \tag{79}$$

We recognize this as the same interface profile used in SAXS analysis of diffuse interfaces when the smearing function $h(r)$ is that given in Eq. (37).

This formalism is readily extended to the case of a multilayer sample with $N$ layers on a substrate

$$R(q_{z,0}) = R_F(q_{z,0}) \cdot \left| \frac{1}{\rho_N} \sum_{i=0}^{N} (\rho_{i+1} - \rho_i) \cdot e^{iq_{z,0}D_i} e^{-(\frac{1}{2})q_{z,0}^2\langle\sigma_{i+1}^2\rangle} \right|^2 \tag{80}$$

with the media indices $i$ varying from $i = 0$ for air to $i = N + 1$ for the substrate and $D_i$ being the distance from the air surface to the interface between media $i$ and $i + 1$. The roughness of the interface between media $i$ and $i + 1$ is $\sigma_{i+1}$. It is the apparent roughness averaged over the coherence length of the experiment which is pertinent here,[110] and thus the averaged quantity $\langle\sigma^2\rangle$ is used. In the special case of a single film on a substrate Eq. (80) reduces to

$$R(q_z) = R_F(q_z) \frac{1}{\rho_s^2} \Big[ \rho_f^2 e^{-(\frac{1}{2})q_z^2\sigma_f^2} + (\rho_s - \rho_f)^2 \cdot e^{-(\frac{1}{2})q_z^2\sigma_s^2} + 2\rho_f(\rho_s - \rho_f) \cdot e^{-(\frac{1}{4})q_z^2(\sigma_s^2 + \sigma_f^2)} \cos(q_z d_f) \Big] \tag{81}$$

where the subscripts s and f indicate quantities referring to the substrate and film, respectively. The Born approximation result contains three distinct terms and allows one to see the important qualitative features of the reflectivity curve away from $q_c$. The first two terms represent the reflectivity from the

film surface and film/substrate interface, respectively, while the third term captures the interference between the two. If $(\rho_s - \rho_f)$ and $\rho_f$ are comparable, as they often are with hydrocarbon polymer films, the asymptotic level of the normalized reflectivity $R/R_F$ will be controlled by the interface with lower roughness. As interface roughnesses are increased, the oscillations at small $q_z$ are preserved and retain the same periodicity. However, oscillations at larger $q_z$ are damped.

In studying interfaces of low molecular weight organic liquids or low viscosity polymer solutions, capillary waves create a microroughness that can be probed with XR. The corresponding density-density correlations at the surface are long ranged,[69] and if finite size effects are ignored $g(R)$ is expected to diverge for large $R$. Thus, no true specular reflection is possible. In real experiments finite size effects manifest themselves in both a gravitational cutoff of $g(R)$ and instrumental resolution limits on the effective integration in Eq. (57). In fact, the mean square roughness $\sigma^2_{\text{eff}}$ measured depends on the resolution used.[146,149-151]

The function $g(R)$ for capillary waves is given to a good approximation by[151]

$$g(R) = 2\sigma^2 - BK_0(\kappa R) \tag{82}$$

where $B = k_B T/\pi\gamma$ and $\gamma$ is the liquid surface tension at temperature $T$ and $K_0(X)$ is the modified Bessel function.[152] The gravitational cutoff, $\kappa$, is given by

$$\kappa = \sqrt{\frac{\Delta\rho_m g}{\gamma}} \tag{83}$$

where $\Delta\rho_m$ is the mass density difference across the interface and $g$ is the gravitational acceleration. The intrinsic roughness of the interface is found to be[146,151]

$$\sigma^2 = \frac{1}{4}B \ln\left[\frac{q_u^2 + \kappa^2}{\kappa^2}\right] \tag{84}$$

where $q_u$ is the upper wave vector cutoff for the capillary waves,[146] which is on the order of $\pi/d_m$, where $d_m$ is the molecular diameter. In experiments, the length scale $1/\kappa$ is not accessible due to resolution limits and one cannot readily separate the true specular reflectivity from the diffuse scattering in the specular direction. Therefore, the measured roughness $\sigma^2_{\text{eff}}$ will actually be larger than the intrinsive value, representing modes which scatter outside the resolution volume.[146] Expressions for $\sigma^2_{\text{eff}}$ given by Braslau et al.[146] and Sanyal et al.[151] differ only slightly numerically and are essentially equivalent to

$$\sigma^2_{\text{eff}} \approx \frac{k_B T}{2\pi\gamma} \ln\left[\frac{2q_u}{\Delta q_y}\right] \tag{85}$$

where $\Delta q_y$ is the resolution in the $q_y$ direction.

The "effective specular reflectivity", $R_{\text{eff}}$, including diffuse scattering, may be calculated for the limiting case of very coarse resolution in $q_y$ to yield[59]

$$R_{\text{eff}} = R_F \exp\left[-q_{z,0}^2 \sigma^2_{\text{eff}}\right] \frac{1}{\sqrt{\pi}} \Gamma\left[\frac{1-\eta}{2}\right] \tag{86}$$

where

$$\eta = \tfrac{1}{2} B q_{z,0}^2 \tag{87}$$

and $\Gamma(X)$ is the gamma function. The factor $(1/\sqrt{\pi})\Gamma((1-\eta)/2)$, which comes from an integration over all $q_y$, differs from unity for large $\eta$. Thus, a simple Gaussian attenuation factor is not adequate to capture the effect of roughness on measured reflectivity with liquid systems. This has been confirmed in detail experimentally by Sanyal et al.[151] with ethanol and by Daillant and Bélorgey [144] for free-draining soap films. In the latter study the authors consider a slightly different form for the height–height correlation function,[143,144] but observe qualitatively similar behavior.

A more precise analysis[134,136-142] of interface roughness effects with solid samples may be achieved by invoking some variant of the

DWBA. Névot and Croce[138] find that when the roughness spectrum has predominantly high spatial frequencies[68] ($\nu > 1\ \mu m^{-1}$) the reflectivity $R_i$ of an interface between media $i$ and $i+1$ in a multilayer is given by

$$R_i(q_{z,i}) = R_{F,i}(q_{z,i})e^{-q_{z,i}q_{z,i+1}\sigma_{i+1}^2} \quad (88)$$

where $q_{z,i}$ is the scattering vector as calculated in the medium $i$ and $\sigma_{i+1}$ is the roughness of the interface. When low frequencies dominate[67]

$$R_i(q_{z,i}) = R_{F,i}(q_{z,i})e^{-q_{z,i}^2\sigma_{i+1}^2} \quad (89)$$

Expressions for the reflectance at one interface in a multilayer are readily obtained from Eq. (75), (88), and (89) by reducing the arguments of the exponentials by a factor of 2. For $q_{z,0} \gg q_c$ the exponential factors in both Eq. (88) and (89) are approximately equal to the simple $\exp[-q_{z,0}^2\sigma_{i+1}^2]$ factor. However, they can differ significantly[138] in the vicinity of $q_c$.

Two common techniques account for roughness in the analysis of reflectivity data. The first involves the inclusion of appropriate exponential attenuation factors chosen from the above options. This method is computationally efficient and may be recommended for use with solid samples having many layers and small interfacial roughnesses. However, the technique presents difficulties for liquid samples and samples with large interfacial roughnesses. The algorithm will allow one to assign roughnesses $\sigma_i$ and $\sigma_{i+1}$ to neighboring interfaces which sum to a length greater than the thickness of the intervening layer. The physical meaning of such assignments is unclear at best.

In the second technique one takes account of the interface diffuseness due to roughness by representing the interface profile with a smoothly varying function and then using the matrix formalism to calculate the reflectivity from a discretized profile of many layers. This is a legitimate means of modeling roughness when calculating the specular reflectivity alone because specular measurements are sensitive only to the laterally averaged variation in $\rho_e$ with depth. It provides an excellent approximation to the true rough surface solution for $q_z > q_c$ where the reflectivity is weak (see below), but is inexact for $q_z < q_c$.[139] However, this limitation is often not critical.

A variety of functional forms may be employed in principle for describing the interface profile, but the error function,[138] (see above) is most often used. When incorporating roughness in this way each sharp interface in the $\rho_e$ profile of a multilayer sample is replaced by several fictitious layers corresponding to the discretized error function. The total number of layers considered in the reflectivity calculation is greatly increased, and thus the computation time as well. The advantage of this technique is that large roughnesses at closely spaced interfaces can be handled in an explicit, realistic way by accounting for the overlap of interface profiles. Therefore, this method is recommended for samples with many narrowly spaced interfaces or large roughnesses. Very fine adjustments in the functional form of the interface profile will often not be justifiable on the basis of the experimental data. On the other hand, certain features, such as interface asymmetry, will yield reflectivity curves which simply cannot be reconciled with an error function-like profile. In this case some information besides simply a single characteristic profile width ($\sigma$) must be included in the model.

### c. Resolution Corrections

Instrumental resolution must be explicitly accounted for by first calculating the theoretical reflectivity $R$ as described above and then "smearing" the curve by convoluting it with an appropriate resolution function. The measurement of capillary wave roughness[146] is one clear example of the importance of this convolution. The smeared reflectivity profile $\tilde{R}$ measured with a spectrometer set at incident angle $\theta_0$, detector angles $\varphi$ and $\psi$,

and nominal wavelength $\lambda$ is given by[79,146]

$$\tilde{R}(\theta_0) = \iiint R(\theta,\phi,\psi,\lambda) \cdot w(\theta_0 - \theta_0', \phi - \phi', \psi - \psi', \lambda - \lambda') \cdot d\theta'\, d\phi'\, d\psi'\, d\lambda' \quad (90)$$

where the distribution function $w$ describes the resolution in each variable. Because $R$ is typically calculated as a function of $q_z$ it is convenient to define a resolution function $g(\mathbf{q}\text{-}\mathbf{q}')$ in reciprocal space and to perform the convolution in $\mathbf{q}$ space.

$$\tilde{R}(\mathbf{q}) = \int R(\mathbf{q}) g(\mathbf{q} - \mathbf{q}') d\mathbf{q}' \quad (91)$$

The forms of the functions $w$ and $g$ can vary widely in complexity depending on the precision of the experiment.

If our subtraction of other scattering effects is sufficiently good that our experimental $\tilde{R}$ contains only contributions from the specular part of the scattering cross-section, then the convolution need only account for contributions from a range of $q_z'$ at any nominal value of $q_z$.[143] Smearing in $q_x$ and $q_y$ may be neglected. In this case

$$\tilde{R}(q_z) = \int R(q_z) g_z(q_z - q_z')\, dq_z' \quad (92)$$

For tube-based reflectometers with simple crystal monochromatization it will be necessary to include the effect of imperfect monochromatization as well as angular resolution, while for synchrotron measurements the correction for $\Delta\lambda$ is unnecessary.

Consider the common case in which polychromaticity and beam divergence must be considered but the resolution of the out-of-plane angle $\Psi$ is not critical. For specular reflectivity measurements, the detector slit is typically set sufficiently narrow to limit background contributions to the signal, but wide enough to capture the entire divergent reflected beam. Thus, the angular divergence of interest is that due to the collimation of the incident beam, which is largely determined by slit dimensions in the direction parallel to the plane of incidence for a typical slit system. The effects of both $\Delta\lambda$ and $\Delta\theta_0$ may be taken into account approximately by noting that the nominal spread in $q_z$ values sampled at a given detector position varies roughly as

$$|dq_z| \cong \sqrt{\left(\left|\frac{\partial q_z}{\partial \theta_0}\right| d\theta_0\right)^2 + \left(\left|\frac{\partial q_z}{\partial \lambda}\right| d\lambda\right)^2} \cong \sqrt{q_z^2\left[\left(\frac{d\theta_0}{\theta_0}\right)^2 + \left(\frac{d\lambda}{\lambda}\right)^2\right]} \quad (93)$$

where $d\theta_0$ and $d\lambda$ are measures of distributions in $\theta_0$ and $\lambda$, respectively. The resolution function $g_z(q_z - q_z')$ may then be taken to be a box function or Gaussian function of width $|dq_z|$. For high resolution work, such as has been done with liquid crystal surfaces,[77,79] more rigorous resolution corrections are required. Pershan et al.[79] provide a detailed discussion of resolution and its effect on the overlapping of bulk and surface scattering.

From a practical standpoint it is important to note that if fixed slits are used, the relative resolution $dq_z/q_z$ generally will be controlled by the beam divergence for small $\theta_0$, but not at larger $\theta_0$. This suggests that in principle the slit dimensions for larger $\theta_0$ could be relaxed to gain intensity, while maintaining roughly constant relative resolution. However, continually adjusting motorized slits to keep $dq_z/q_z$ constant over a large range of $q_z$ may be impractical.

### 3. Instrumentation

Appropriate instrumentation and proper sample preparation are both critical to the successful exploitation of the XR technique. Geometrically, the experiment is identical to that of classical reflection mode wide angle diffraction done routinely in many laboratories using user-friendly commercial apparatus. However, good reflection measurements demand a combination of large intensity dynamic range and precise collimation at low

angles which a commercial apparatus aligned for routine wide angle work is generally unable to provide. Of course, both the necessary resolution and large dynamic range may be obtained by using a synchrotron radiation source. However, it is often possible to obtain excellent data using a sealed tube or rotating anode with an appropriate reflectometer. The collimation precision[80] needed depends on the incident angle range and the features to be studied. Typically, measurements must be made over incident angles from 0.1° to a few degrees. If data are sought for films of moderate thickness (100 to 500 Å) and only for $q_{z,0} \gg q_c$ a commercial diffraction apparatus may provide adequate resolution once it has been realigned specifically for low angle work and the smallest available slits have been mounted. Helpful summaries of important points of alignment, collimation, and choice of optics are offered by Parrish et al.[80] and Weiss et al.[75]

Data at the lowest angles present the greatest challenges to collimation because the incident beam footprint size diverges as the incident angle decreases to zero. Also, the relative error in the resolution of $q_{z,0}$ due to slit size grows as the incident angle is decreased. Particularly tight collimation is thus required to obtain data for $q_{z,0}$ near $q_c$, which is free of sample size effects. Fine resolution of the rapid decrease of intensity at $q_c$ or resolution of fringes for comparatively thick films[80] (e.g., 2000 to 5000 Å) both place extra demands on the collimation as well. For such measurements a device specifically suited to low angle measurements is generally required.

The range of reflectivity needed is also affected by the type of structure to be studied. In contrast to thick films, ultrathin films, such as monomolecular layers created using Langmuir-Blodgett (LB) or self-assembly techniques, present very widely spaced Kiessig fringes. Accurate determination of the film thickness requires measurement to $q_{z,0}$ on the order of 0.2 $Å^{-1}$ (2.8° for $\lambda$ = 1.54 Å), as demonstrated in Figure 14 for the case of a self-assembled monolayer (SAM) of hexadecyltrichlorosilane on silicon. However, it

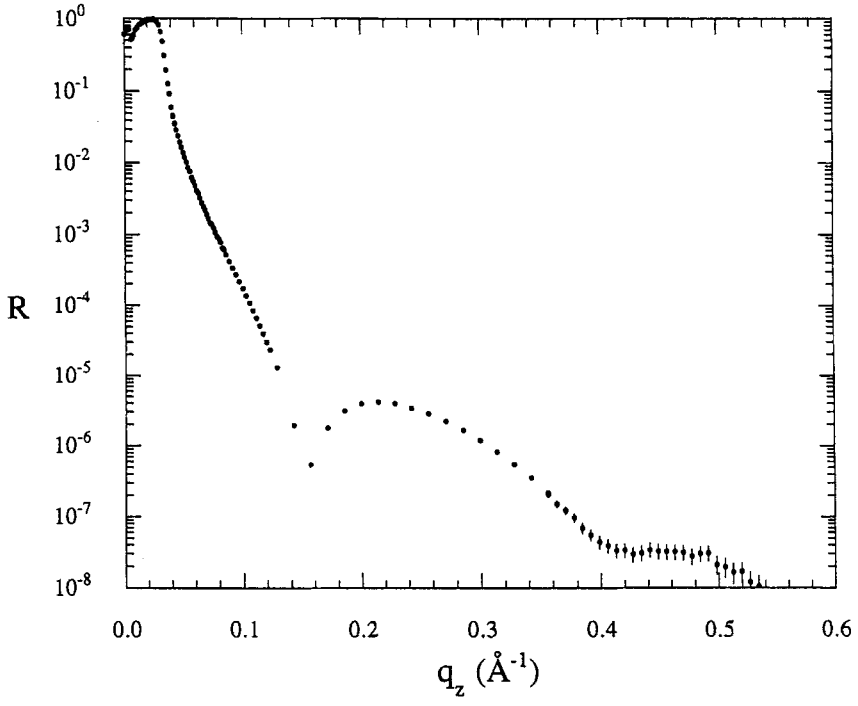


**FIGURE 14.** Reflectivity of a SAM of hexadecyltrichlorosilane on a silicon wafer with its native oxide layer.

may be possible to circumvent this difficulty. Thicker samples containing fine internal features of interest will also require measurements to high values of $q_{z,0}$. As a good first estimate one may assume that $r_{min}$, the minimum characteristic distance in the sample structure which is rigorously resolved by a data set extending to $q_{z,o} = q_{max}$, is given by $r_{min} = 2\pi/q_{max}$.

Two factors contributing to attainable dynamic range are primary beam intensity and background level. The primary intensity is affected by choices of X-ray source and optics. When using lower intensity sealed tube and rotating target anodes, primary intensity may be boosted by relaxing the collimation or monochromatization. Slit collimation brings a slight penalty in resolution, but the tradeoff is often warranted so long as sample size is of no issue. Dramatic improvements in intensity can be made by using mosaic crystals, for example, pyrolytic graphite, instead of single or multibounce single crystal monochromators. The use of single crystals may generally be reserved for cases in which outstanding resolution is demanded.[80,82] One advantage of multibounce single crystal monochromators is that they both select a wavelength and collimate. While changes in collimation geometry and monochromatization are best done infrequently, relaxing the collimation by opening the slits wider may be done easily between measurements using variable slits or even during a single measurement if motorized slits are used. Such adjustments allow quick tradeoff of resolution for intensity and the adjustment of footprint size to the available sample. However, the adjustments complicate the detailed analysis of the data. Often one finds that adoption of some standard configuration offering a prudent compromise between resolution and intensity allows the easiest comparison of various samples. Background scattering may be suppressed by minimizing the distance through air which any beam must pass, proper alignment of clean optical components, selection of a low noise detector, and optimization of noise suppression in the detector electronics. A final option for increasing intensity at the cost of resolution is to use focusing optics.

Early reflectivity measurements of organic films in general, and polymers in particular, came considerably later than the first measurements with metal and semiconducting materials.[61,70-73] Three factors probably contributed to this, and continue to make reflectivity with these systems a challenge. First, the critical angles of polymeric materials lie below those of metals. Second, polymers generally present weaker contrast than do inorganic systems. Finally, methods appropriate for creating polymer films of sufficient smoothness and planarity for reflectivity were developed long after single crystal polishing and evaporation techniques.

The recent literature offers descriptions of several possible reflectometer configurations. Foster et al.[74] describe a rotating anode-based reflectometer designed specifically for use with solid polymer films. This apparatus, shown in Figure 15, differs from commercial diffractometers in three ways:

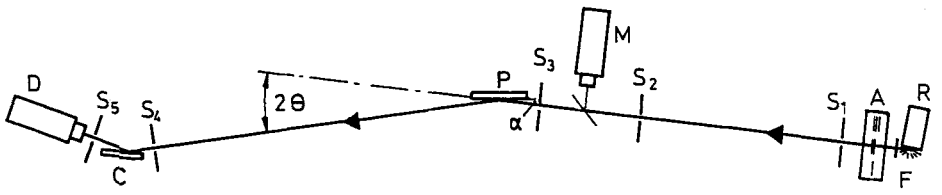


**FIGURE 15.** Schematic drawing of a rotating anode-based reflectometer.[74] *R* is the source; *F* is a nickel filter for suppressing the $K_\beta$ line; *A* is an automatic attenuator; $S_1$ to $S_5$ are slits; *M* is the incident beam monitor; *P* is the polymer sample; *C* is a graphite crystal; *D* is a NaI scintillation counter. (Reprinted with permission of Pergamon Press, Ltd.)

1. An automatic attenuator immediately adjacent to the anode adjusts the primary beam intensity to avoid saturating the detector at low incident angles. Various numbers of thin, pure nickel foils are mounted on a rotating circular frame, which is driven by a stepping motor interfaced with a microcomputer which also monitors beam intensity.
2. A beam monitor detects time fluctuations in the primary intensity and allows corrections for them.
3. The collimating and detector slits are mounted on an optical bench which allows their positions to be readily adjusted among various standard spacings to allow the tradeoff of intensity for resolution.

Specifically, one may use much longer slit spacings than are provided by commercial designs. Two potential disadvantages of this setup result from positioning the monochromator after the sample. Passing unneeded high energy photons through the collimation system and sample area can contribute to difficulties arising from fluorescence and radiation damage of the sample. Also, the energy spectrum of the monitored beam is not the same as that of the detected beam.

Weiss et al.[75] present a novel diffractometer (Figure 16) designed for use with horizontal liquid samples such as one might encounter in studies of polymer melts and polymer/liquid interfaces. This unique capability comes at the cost of greater complexity in the alignment of the collimation and detection arms, which must be raised and lowered in a synchronized fashion. Another distinguishing feature is use of a double bounce $^{111}$Ge single crystal to provide outstanding monochromatization before the sample.

One means of improving resolution is to use a longer wavelength of radiation. Jark and Stöhr[76] describe a compact triple axis diffractometer designed for use with soft X-rays (6 Å < 1 < 400 Å) at a synchrotron beamline. Because these X-rays are strongly absorbed in air, the beamline optics are maintained in ultrahigh vacuum and the diffractometer itself must function in a high vacuum environment of $10^{-6}$ torr pressure. This presents unusual design challenges and

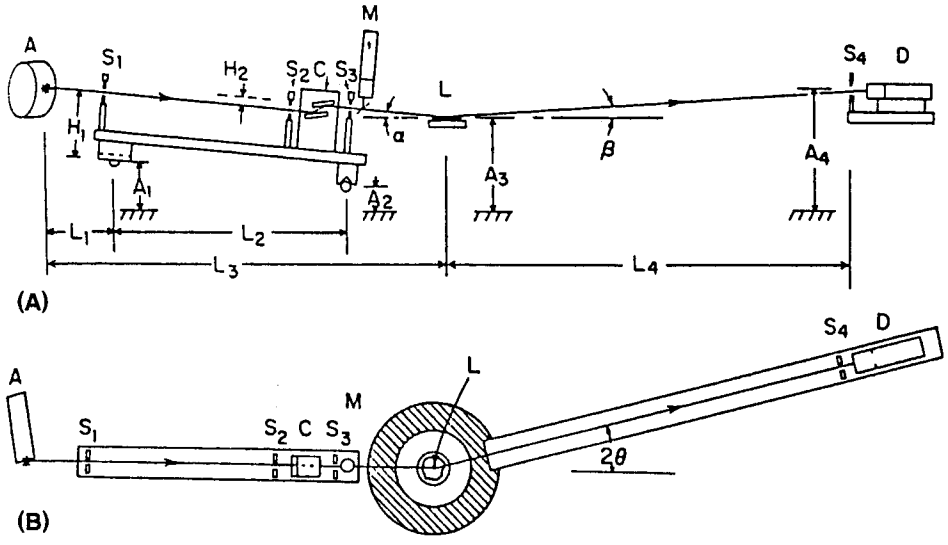


**FIGURE 16.** Novel rotating anode-based diffractometer[75] for reflectivity measurements from horizontal samples. (A) Side view. The beam from the anode *A* is collimated by slits $S_1$ and $S_2$, monochromatized by a double bounce $^{111}$Ge crystal *C* and monitored (*M*) before striking a liquid sample *L*. Slits $S_3$ and $S_4$ reduce background scattering recorded by the detector *D*. (B) Top view. (Reproduced, with permission, from reference 75.)

requires both that the sample be studied in high vacuum and that substantial amounts of time be set aside for pumping when changing samples. The compact construction forfeits some of the resolution gain accomplished by using soft X-rays. Also, the dynamic range is only about 5 orders of magnitude, far smaller than that available with other instruments. The Schottky-type GaAsP photodiode used is far from saturation when measuring the nearly $10^9$ photons per second count rate at total reflection, but electonic noise precludes measurement of count rates lower than ca. $10^4$ photons per second. Modifications could be made to deal with this limitation and substantially increase the dynamic range, so that the disadvantages of working with high vacuum and a synchrotron source remain the most important limitations of this reflectometer type.

Several groups have done reflectivity measurements on organic systems using synchrotron radiation, most notably Pershan and co-workers.[77,78,83] One possible configuration for a synchrotron-based reflectometer, which also allows grazing incidence diffraction measurements of liquid surfaces, is discussed by Schlossman and Pershan[83] and shown in Figure 17. A beam horizontally and vertically focused by a bent cylindrical mirror is monochromated by a $^{111}$Ge crystal before entering the hutch. A second $^{111}$Ge crystal, mounted in a four-circle goniometer, tilts the beam downward onto the sample at the proper angle.

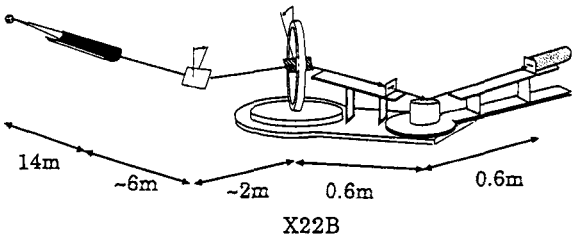


**FIGURE 17.** Schematic illustration of the reflectomer on beamline X22B at the National Synchrotron Light Source, Brookhaven National Laboratory, discussed by Schlossman and Pershan.[83] The beam is focused by a bent mirror, then monochromated and tilted downward onto the sample with two $^{111}$Ge crystals. This configuration also may be used for off-specular and grazing incidence diffraction measurements. (Reproduced, with permission, from reference 83.)

To keep the incident beams passing through the vertical axis of the sample center while varying $\theta_0$ requires rotating both Ge crystals simultaneously. Additionally, the sample is moved horizontally by rotating the "two-theta" arm of the goniometer carrying the second Ge crystal. A vertical slit before the sample limits footprint size, while a slit before the detector is opened to accept the divergent specular beam when measuring reflectivity or narrowed to define resolution when measuring off-specular scattering or surface diffraction.

Daillant et al.[84] discuss a series of elegant measurements of polymer wetting using a four circle diffractometer mounted on a conventional sealed tube Cu anode. The diffractometer is specially designed to allow reflectivity, surface diffraction, and grazing incidence measurements all to be performed. A flat $^{200}$LiF crystal is used as a primary monochromator and small collimation slits provide a $20 \times 100$ μm beam for mapping the variation of a thin film structure across the sample. This small beam cross-section is noteworthy because long beam profiles are often used in scattering experiments with sealed tube sources in order to improve flux. However, the authors report reflectivity measurements as low as $10^{-8}$ and an angular divergence of ca. 0.006° using the modest flux. In addition, they report surface diffraction measurements, which can be challenging, even with the help of a synchrotron source. On the other hand, the phenomena being studied are extremely slow and the speed of data collection is not important here.

Data collection speed is greatly improved with an apparatus described by Naudon et al.[85] which uses a position-sensitive detector (PSD). This reflectometer, shown schematically in Figure 18, operates in what the authors refer to as the "angular dispersive mode", collecting a reflectivity profile for $0 < q_z < 0.2$ Å$^{-1}$ with moderate resolution in

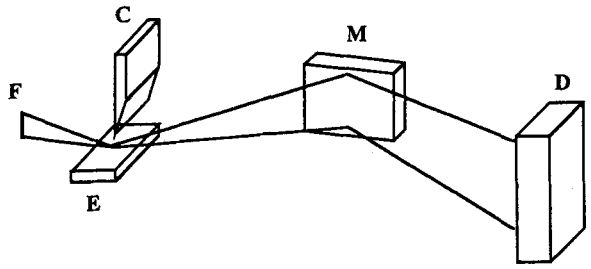


**FIGURE 18.** Schematic presenting the principle of the angular dispersive mode reflectometer with PSD. Point beams from along the line focus *F* are reflected from the sample *E* at different angles, monochromated by the $^{111}$Ge crystal and detected simultaneously by the PSD *D*.

a matter of several minutes. X-rays from a line focus ($8 \times 0.4$ mm$^2$) perpendicular to the sample surface plane are reflected from the sample, monochromated by a $^{111}$Ge crystal, and collected using a PSD oriented perpendicular to the sample. A knife edge positioned very close to the sample surface defines the length of the incident beam footprint (typically 5 mm), so that effectively the focus may be considered a source of many beams of small cross-section, each reflecting at a different angle. The angular resolution then depends on the spatial resolution of the PSD and the sample to detector distance as well as $\theta_0$. With a detector resolution of 175 μm and sample to detector distance of 2090 mm a resolution $\Delta\theta_0 = 0.005°$ is achieved at $\theta_0 = 2°$. This device is intended for quickly measuring thicknesses of many small thin film samples and the authors demonstrate its effectiveness for this usage. Due to the unusually small beam footprint, typically $0.2 \times 5$ mm$^2$, it is also readily used with imperfectly flat samples.

Reflectivity data also have been collected in a few cases using energy dispersive reflectometers. Bilderback and Hubbard[86,87] used a standard 50 kV X-ray generator and Si(Li) detector to measure X-ray mirrors over energies from 3.8 to 50 keV at 0.23° incidence, which corresponded to a $q_z$ range of 0.015 to 0.20 Å$^{-1}$. Chason and Warwick[81] probed a $q_z$ range of comparable size, while Tanner et al.[88] used a 150-kV tungsten source with a Ge(Li) detector to substantially increase the range of $q_z$ attainable with a single incident angle. The high reflectivity data for low $q_z$ are readily collected in a short time, but the method cannot compete at large $q_z$ with the statistics attainable with step counting systems. Thus it has not found broad application.

All of the instruments mentioned thus far represent diffractometers constructed specifically with a view toward performing reflection measurements. The option of constructing or acquiring a dedicated apparatus may not be an option for some investigators. Thus, the recent report by Elben and Strobl[89] of a comparatively straightforward modification of a Kratky small angle camera is of considerable interest. The replacement of the conventional sample stage with a rotating one driven by a stepper motor allows the measurement with a conventional sealed tube anode of reflectivities over 6 orders of magnitude with a minimum $\theta_0$ of 0.1° and step size on the order of 0.012°. This approach recommends itself as a means to gain access to reflectivity measurements with a modest adaptation of existing resources.

## 4. Sample Preparation

The full advantages of reflection techniques for interfacial sensitivity can be realized only with samples that meet stringent requirements. First, the sample must be very planar. Best is a planarity comparable to that found with optical flats. However, the severity of the planarity criterion depends on the region of the reflectivity curve one must investigate. As with several other considerations, matters are not so critical if one is specifically interested in data at $q \gg q_c$, because distortions in the reflectivity curve due to the waviness of the surface become more pronounced as $\theta_0$ decreases. Unfortunately, sample alignment is generally done primarily using incident angles near the critical value, precisely because of the intrinsic sensitivity to exact surface placement and high intensities. Alignment of nonplanar samples may be very difficult and tedious or impossible. A second important criterion for a good reflec-

tivity sample is smoothness. Samples with micron-scale roughness cannot be studied at all and even microroughnesses of ca. > 60 Å rms will generally severely impede reflectivity analysis. The third criterion, which is important in the case one wishes to accurately determine layer thicknesses, is thickness uniformity. Variations in thickness should be kept in the 0.1 to 2 nm range for best results. A final, generic criterion is that sufficient electron density differences exist across interfaces of interest.

Because polymer surfaces manufactured by almost all commercial means fail to meet one or more of the above criteria, one is generally unable to train the reflectivity technique on a material in its technologically common form. However, it is often possible to create model samples with an advantageous planar geometry, using specialized techniques or substrates. Two substrates that recommend themselves are float glass and silicon wafers. While polished optical flats may offer better planarity than float glass, they are much more expensive and their surface microroughness is generally greater than the 5 to 10 Å rms microroughness for float glass. Float glass quality can vary widely among suppliers and one side of the glass is intrinsically of higher quality than the other due to the manufacturing process. Silicon wafers of standard dimension are readily obtained with one or both sides polished and with a variety of orientations. They offer outstanding microroughness of typically 3 to 5 Å root mean square, but planarity may vary from wafer to wafer. For critical applications each candidate wafer should be examined before sample deposition. Both the glass and silicon are available in various thicknesses, although nonstandard wafers are considerably more expensive. While standard thicknesses will work for smaller samples, for large-diameter (> 5 cm) samples substrate thickness must be greater to avoid bowing or surface stresses due to mounting.

Four techniques particularly suited to creating films with well-behaved surfaces are spin casting, evaporation, Langmuir-Blodgett deposition, and self-assembly. One other possibility is solution casting. At least four of these techniques share the property that the deposition process itself may significantly impact the morphology of the layer or surface, so precautions always should be taken to ensure that the sample has had an opportunity to equilibrate after deposition, unless one wishes specifically to study the "as-deposited" state.

Solution casting from dilute solution is a simple technique and may on occasion be acceptable for preparing a few samples. The surface upon which the film is cast must be carefully leveled and free from vibrations. Sample thickness may be varied by varying concentration. However, film surface microroughness varies widely and it is difficult to reliably prepare sample series for comparison purposes.

Spin casting[90] presents a far superior technique which is applicable to many polymers, although those that crystallize or are insoluble in common solvents present special challenges. Outstanding thickness uniformity and surface microroughness of about 3 to 10 Å root mean square are readily achievable. Choice of solution concentration (typically 0.5 to 2 wt% depending upon molecular weight) is critical and generally possible only after some experimentation to clarify the variation of thickness with concentration and spin speed. Care must be taken to properly clean the substrate and keep the substrate and solution free of dust in order to avoid film defects. During spinning the polymer solution is subjected to high shear and orientation of the polymer should be expected in the as-deposited state. Subsequent annealing under vacuum and moderately elevated temperature is necessary to fully remove residual solvent. Further annealing at higher temperatures also may be needed to attain true equilibrium.

Evaporation is a classical technique not generally applicable to polymers, but useful for modification of substrate surface character.[92-94] Evaporation also may be used to deposit metal films needed to create metal/polymer interfaces or multilayered samples. Clearly sputtering[96] and molecular beam epitaxy[95] may find utility in preparing multilayered samples containing metals. Both

may be used to create multilayer substrates useful for XR aided by interferometry.[91,95,96]

Langmuir-Blodgett (LB) deposition is used to produce films with precisely controlled thickness and order.[97,98] As such it is used with both small amphiphilic molecules as well as polymers to create monolayers for surface modification, ultrathin films for study of molecular interactions, and multilayers[99-101] for various purposes. This technique demands a high level of expertise and some sophisticated equipment for good and reproducible results. However, it offers capabilites for engineering complex multilayer structures which are unique at the present time. Well-ordered LB multilayers are readily studied by reflectivity[102,103] as they exhibit outstanding thickness uniformity, good microroughness, and often periodic structures which yield readily recognized characteristic reflectivity features.[104] The stability of LB thin film structures has been investigated and is a key issue to consider when using such films.[107,108] Schwarz et al.[105] recently demonstrated that layers of cadmium arachidate multilayers rearrange at the air surface and recent results of Tsukruk et al.[106] suggest similar phenomena may also occur with polymer LB films.

Self-assembly from solution can provide robust organic monolayers of precise thickness without extensive instrumentation.[97,98] By far the majority of SAMs studied to date have been created with small chain molecules.[109-111] Thus, the primary use of SAMs in polymer interface study is in substrate modification to provide low energy surfaces. When deposited on silicon wafers it is possible to form fairly uniform surfaces with few defects[112,113] and low microroughness. Therefore, small molecule SAMs work well in samples to be analyzed with XR. Deposition of multilayer structures[114] presents additional possibilities. Reflectivity study of polymer self-assembly into monomolecular layers by grafting (as opposed to adsorption) is only recently being studied.[115,116] Reflectivity will play an important role in the emerging study of such systems due to its sensitivity to layers of monomolecular thickness and "buried" interfaces.

For some studies, for example, those of interdiffusion, it is necessary to create bilayers or multilayers of polymers that do not lend themselves to self-assembly or LB deposition. Two techniques may be used in this case. In one,[117,118] a first film is cast directly on the sample substrate, while a second is cast on a spare substrate. The second film is then lifted from its substrate by floating it off in pure water and picked up using the sample substrate covered with the first film. It is impossible to form ideal interfaces in this matter, but careful vacuum annealing removes residual water and reduces voids between the layers. Some "wrinkles" in the top layer are unavoidable and the top polymer layer must be of sufficiently high molecular weight (typically $> 20{,}000$ g/mol) and thickness (e.g., $> 200$ Å) to have the mechanical strength to withstand the transfer. A second multilayer formation technique is to sequentially spin cast multiple layers on a single substrate using solvents specific to each layer.[118] If the solvent used to spin the second layer is a nonsolvent for the first, the contact time between the existing layer and solution may be short enough that no significant undesirable solvation occurs.

Two means for enhancing interface contrast are known in the literature, both of them methods used first for other analytical techniques. Hüttenbach et al.[119] use tiny gold spheres (Kirkendall markers)[120] evaporatively deposited between miscible polymer layers as a means of following the interface position during interdiffusion. The gold/polymer electron density difference is very large and the sample can be successively annealed and measured because the interface decoration presents a minor perturbation to the polymer movement across the interface. Schaub et al.[121] increase the electron density difference between two parts of a thin film sample by staining with $OsO_4$, a technique widely used in the TEM study of block copolymers.[122] The $OsO_4$ reacts with double bonds located in a particular molecule or portion of a molecule, strongly increasing its electron density. Application of this technique is limited by the need for certain bonds in the sample, although consideration of additional

known staining agents[122] such as $CH_3I$ would ameliorate this restriction. Another limitation arises from the resulting structure perturbation. Characteristic structural dimensions may be altered and the dynamic behavior of the sample is assuredly changed by staining. Once stained, the sample will not respond to thermal or other treatment at all as would an unstained film.

Samples that flow under the action of gravity may not be studied using grazing incidence techniques without special consideration. Because placing a window next to the sample surface may dramatically alter the electron density profile near the surface, using a closed cell to contain the sample is not an option, and the geometry of the camera must allow the sample to remain horizontal.

### 5. Comparison with SAXS

Both XR and SAXS measurements may provide information on interfacial thickness and thus it is helpful to compare the relative merits of the two techniques. SAXS has the advantage that it is a more widely known technique and SAXS apparatus may be found in many laboratories that do not have facilities suited to performing reflectivity measurements. However, obtaining sufficiently good data in the Porod region and performing the necessary background corrections is challenging and demands more than a passing familiarity with the technique, although the final determination of interface width $E$ from the corrected data may be reduced to a linear regression. A second, decided advantage of SAXS is that it may be used to study systems with irregularly shaped phases and rough surfaces, although the sample should be of uniform thickness across the illuminated area. Easily deformed samples also may be studied readily without demands on the camera design except for the use of a closed sample cell. In this sense SAXS requires less perfect samples. On the other hand, in order to have a sufficient signal for SAXS analysis at least one phase must have colloidal dimensions so that sufficient interfacial area is present.

Reflectometry presents an overall greater applicability to the study of polymer surfaces and interfaces, but provides advantages in the determination of interfacial thickness alone only in specific cases. The reflectivity apparatus is not so widely available, and while the necessary background correction may be more straightforward than that required for SAXS, the final evaluation of $E$ must be performed using nonlinear regression. Also, fluid systems require a particular reflectometer geometry. The great and very important advantage of reflectometry comes in its applicability to systems composed of thin films, e.g., dielectrics for microelectronics, and two phases separated by a single interface, e.g., immiscible homopolymer blends. The reflection geometry provides the sensitivity necessary to study these interfaces.

### 6. Variations on the Reflectivity Experiment

#### a. Anomalous Reflectivity

Sinha et al.[123] have recently described how the measurement of specular reflectivity close to, and away from, an absorption edge of the sample substrate allows one to recover phase information otherwise lost. In principle this measurement allows one to perform a model independent inversion of the data. The method is similar in approach to anomalous scattering techniques used in X-ray crystallography. In the present case the electron density profile perpendicular to the interface is inverted from many closely spaced points approximating a continuous function of $q_z$, while in crystallography a set of discrete reflections is used. Three important distinctions of the technique are made as compared to common specular reflectivity. First, an energy tunable source is required, necessitating the use of a synchrotron-based reflectometer. Second, the substrate must be chosen so that an absorption edge may be readily accessed. In the example presented by the authors, a Ge substrate was used with X-ray energies of 11.030 and 10.600 keV. The final distinction lies in the data analysis.

Taking advantage of the two measurements involves developing a set of two equations in the unknowns $\Delta\rho_e(\tilde{q}_z)$ and $\Delta\rho_e^*(\tilde{q}_z)$, which represent the Fourier transform (apart from a constant factor) of the electron density modulation $\Delta\rho_e(z)$ and its complex conjugate

$$\Delta\rho_e(\tilde{q}_z) = \int_{-\infty}^{\infty} \Delta\rho_e(z) e^{i\tilde{q}_z} dz \qquad (94)$$

and the scattering vector $\tilde{q}_z$ is that inside the sample. The electron density profile of the film is defined as $\rho_e(z) = \rho_0(z) + \Delta\rho_e(z)$, where $\rho_0(z)$ is some zeroth order approximation to the film's profile chosen such that the reflection coefficient $r_0(q_{z,0})$ from the system consisting of the substrate plus $\rho_0(z)$ may be calculated analytically using the DWBA.[139] Sinha and co-workers[123] chose $\rho_0(z)$ to be that of a uniform film of thickness $\delta$. In other words, $\rho_0(z)$ is constant for $z = 0$ to $z = \delta$. The reflectivity of the actual system is then given by

$$R(q_{z,0}) = \left| ir_0(q_{z,0}) + \frac{4\pi r_0}{q_z} \left[a^2(q_{z,0})\Delta\rho_e(\tilde{q}_z) + b^2(q_z)\Delta\rho_e^*(\tilde{q}_z)\right] + 2a(q_{z,0})b(q_{z,0})\Delta\rho_e(0)\right|^2 \qquad (95)$$

where $q_z$ is specified in the uniform film of density $\rho_0$. The coefficients $a(q_{z,0})$ and $b(q_{z,0})$ are the complex coefficients of the transmitted and reflected waves in the uniform film of electron density $\rho_0(z)$. If $\rho_0$ is chosen to be the true average electron density of the film, the term $\Delta\rho_e(0)$ drops out. This $\rho_0$ value may be determined iteratively if not known *a priori*. The term $r_0(q_{z,0})$, which depends only on the substrate identity, may be calculated for each of the two wavelengths used. For each value of $q_{z,0}$ for which $R(q_{z,0})$ has been measured, the real and imaginary parts of $\Delta\rho_e(\tilde{q}_z)$ may now be calculated from Eq. (95). Because $\Delta\rho_e(z)$ is real, $\Delta\rho_e(-\tilde{q}_z) = \Delta\rho_e^*(\tilde{q}_z)$ and only values $\Delta\rho_e(\tilde{q}_z)$ for $\tilde{q}_z > 0$ are needed to find $\Delta\rho_e(z)$. From a table of $\Delta\rho_e(z)$ values a second table of these quantities evaluated at equally spaced $\tilde{q}_z$ may be interpolated. A fast Fourier transform (FFT) is then used to obtain $\Delta\rho_e(z)$ without recourse to a specific model.

The anomalous reflectivity technique presents a unique capability in that it allows the data to be inverted in a model-independent way. However, it must be pointed out that use of data over a limited range of $q_z$ in any real experiment places restrictions on the effectiveness of this inversion. The author anticipates rapidly growing interest in the anomalous reflectivity technique, but for many researchers its dependence on the use of a synchrotron source will present a substantial difficulty.

### b. X-Ray Interferometry

X-ray interferometry[95,124] may also be used to recover phase information when performing XR measurements. In this technique the reflectivity is measured for a system that combines the unknown structure with a reference structure for which the reflectivity has been measured. If one considers only $q_z \gg q_c$ the Born approximation may be invoked and the overall reflectivity written as given in Eq. (76). Contributions to the reflectivity from the known structure and unknown structure may be explicitly separated

$$\frac{R(q_z)}{R_F(q_z)} = |F_{\text{ref}}(q_z) + F_{\text{unk}}(q_z)|^2 \qquad (96)$$

where $F_{\text{ref}}(q_z)$ is the term arising from the reference structure and $F_{\text{unk}}(q_z)$ is that from the unknown structure. Because these are complex quantities

$$\frac{R(q_z)}{R_F(q_z)} = |F_{\text{ref}}(q_z)|^2 + |F_{\text{unk}}(q_z)|^2 + 2|F_{\text{ref}}(q_z)||F_{\text{unk}}(q_z)|\cos \cdot\{[\varphi_{\text{unk}}(q_z) - \varphi_{\text{ref}}(q_z)] + [2\pi q_z z_{\text{ru}}]\} \qquad (97)$$

with $\varphi_i$ the phases of the respective terms each referenced to the center of mass of their respective profiles and $z_{ru}$ the distance along the $z$ direction between the two centers of mass. From a measurement of $R/R_F$ one may recover $\varphi_{unk}$ if both $F_{ref}(q_z)$ and $\varphi_{ref}(q_z)$ are known.

Rieutord et al.[124] describe how the air/sample and sample/substrate interfaces of a multilayer may play the role of reference structure for determination of the internal structure of a multilayer. They describe how the phase of the reference structure is evaluated and subsequently the amplitude and phase for $F_{unk}$ calculated. Several important aspects of the technique are discussed. One generalization which may be realized is the use of a single interface as the reference structure. On the other hand, aspects exist that limit the application of the technique. First, the phase determination will be accurate only if the reference and unknown terms are of the same order of magnitude. In the multilayer case the relative strengths of these terms depend on the number of layers, $N$, in the multilayer and on the amplitude of the electron density modulations within the multilayer. Because the strength of the reference term is fixed, while that of the internal structure increases with $N$, many layers will be needed if the internal structure electron density modulations are weak. If they are very strong, it may be difficult to perform the analysis except for films of very few layers. A second limitation arises from the need for well-defined interfaces throughout the sample, although small roughnesses may be tolerated.

Murphy et al.[95] introduce the reference structure by depositing the sample on a previously measured semiconductor multilayer superlattice structure deposited with molecular beam epitaxy (MBE). The great advantage to this approach is that the superlattice structure, in principle, may be optimized for the sample of interest. On the other hand, the technique requires the use of modern MBE fabrication techniques and access to a high resolution spectrometer. MBE is preferred to magnetron sputtering[96] for fabrication of the the substrate. Both LB deposited monolayers of cadmium arachidate and cadmium palmitate[95] as well as a layer of a biological macromolecule, yeast cytochrome $c$,[125] adsorbed to a SAM have been investigated with this technique.

## C. Off-Specular Scattering

### 1. Introduction

Off-specular or "diffuse" scattering experiments involve studying the scattered intensity away from but within a few degrees of the specular direction, and thus represent a type of small angle scattering. As shown in Figure 19, the scattering vectors investigated contain finite $q_x$ or $q_y$ components. Therefore, off-specular scattering provides information on both surface topology and near-interface inhomogeneities in directions parallel to the surface.

Diffuse scattering has not been developed as much as specular reflectivity due to its greater complexity and the later development of the accompanying theory. However, considerable progress has been made in this area in the last few years, and a variety of experiments have been performed recently. Although only a few with polymer systems[160] have been published, it is already clear that proper analysis of this scattering can bring important insights. The author therefore expects tremendous growth in this area in the

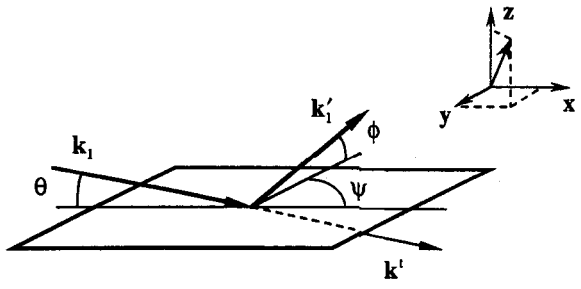


**FIGURE 19.** Scattering geometry for discussion of diffuse scattering and grazing incidence diffraction. (The convention adopted for the orientation of the $x$ and $y$ directions corresponds, for example, to that of Daillant and Bélorgey,[143] and differs from that used by Sinha et al.[139])

next few years, similar to the growth in reflectivity studies in the recent past. Russell[18] has briefly reviewed the earliest developments in this area, but several important advances have come rapidly in the short time since.

The equations discussed in the following are intended primarily for use with the study of surface or interfacial structure as opposed to inhomogeneities beneath the surface or interface. In some cases the theory may be extended to such systems, though this extension is nontrivial. Actual measurement of near-interface lateral structure using off-specular information is dealt with specifically.

## 2. Theory and Analysis

### a. Overview

The phenomenon of off-specular or diffuse X-ray scattering under grazing incidence was first observed by Yoneda[126] and subsequently studied phenomenologically by other groups.[127-133] Efforts to quantitatively explain the change in specular X-ray intensity as a result of off-specular scattering began in 1970.[134] At this time an understanding was growing among researchers that much of the observed scattering was probably due to details of the surface roughness of a sample. Progress being made at that time in the theoretical description of visible light and radar wave scattering from rough surfaces[135] was consistent with this view. Different approaches have been developed to tackle the general problem of scattering from rough surfaces as the radiation wavelength and scale of roughness vary, so that solutions are available for wavelengths over 10 orders of magnitude.[135]

For the solution of off-specular X-ray scattering from single rough surfaces alone several methods have been used which all entail converting the inherently three-dimensional problem of describing the scattering from an "interphase" of finite thickness, described by Eq. (8), into the interfacial problem defined in Eq. (9). The structure of the interface is described primarily by specifying correlations in the plane of the interface and variation in composition across the "interphase" is only considered indirectly. The methods used include those based on the Born approximation,[139,140] the so-called specular approximation,[141,144] Green's functions,[146] and the DWBA.[139,142] A further method that was developed by Croce and co-workers[134,136-138] and applied by Daillant and Bélorgey[143,144] is based on the reciprocity theorem, but has been shown to be equivalent to a type of DWBA. Extensions of these theoretical treatments have been made for films with two rough interfaces,[142,143] multilayers with rough interfaces,[141] and samples such as diblock copolymer films, which can display surface domains.[145] Both the specular approximation and the Croce method may be extended, in principle, to volume scattering near the interface as well by modeling the sample structure as a multilayer as discussed in Section 2a and defining in plane correlation functions between features in each layer as well as layer to layer correlations. Wu[147] handles the scattering problem in another way which he contends may be more readily extended[148] to scattering from three-dimensional inhomogeneities near the surface. The electron density difference with respect to a reference, $\Delta\rho_e$, in both the perpendicular and in plane directions is considered simultaneously within the approximation that the overall electron density function may be represented by a product $\Delta\rho_e(z, R) = \Delta\rho_e(z)\Delta\rho_e(R)$. The points in the different developments of the off-specular scattering expressions where approximations may be made are several, and generally each study handles them somewhat differently. This review focuses only on some key intermediate expressions and the final results. The reader is referred to the original papers for details of the variations.

For our discussion we adjust our notation slightly as clarified in Figure 19, which assigns a wave vector $\mathbf{k}_1$ to the incident beam, $\mathbf{k}'_1$ to the reflected beam, $\mathbf{k}'_1$ to the refracted beam, and $\mathbf{k}_2$ to the scattered beam. Consider the random rough surface $z(x, y)$,

shown in Figure 5, which has associated with it the average smooth surface, $z_0$, taken to be the $(x, y)$ plane.

### b. Formalisms for Calculating Cross-Sections

The simplest approach to the scattering from a single rough interface is based on the Born approximation. Sinha et al.[139] and Wong and Bray[140] discuss the form of the scattering in this limit. The differential cross-section including both the specular and diffuse components follows from Eq. (9)

$$\frac{d\sigma}{d\Omega} = \frac{r_0^2(\Delta\rho_e)^2}{q_z^2}\iint_{S_0} dx\,dy \iint_{S_0} dx'\,dy' \cdot e^{-iq_z[z(x,y)-z(x',y')]} e^{-i[q_x(x-x')+q_y(y-y')]} \tag{98}$$

where $S_0$ is the $(x, y)$ plane and $\Delta\rho_e$ is equal to $\rho_e$ of the condensed medium. If we assume that $[z(x, y) - z(x', y')]$ is a Gaussian random variable[139] and $g(R)$ goes to zero for some finite $R$, then we may write

$$S_{\text{diff}}(\mathbf{q}) = \frac{e^{-q_z^2\sigma^2}}{q_z^2}\iint_{S_0} dX\,dY\,(e^{q_z^2 C(X,Y)} - 1)\, e^{-i(q_x X + q_y Y)} \tag{99}$$

where $C(X, Y)$ is the height–height correlation function, with the interface defined in Eq. (69). The diffuse scattering structure factor is simply derived from that for the total scattering by including the $-1$ term in parentheses, which subtracts the specular component.

Equation (99) may be solved numerically for various models of $g(R)$. Results from such a calculation by Sinha et al.[139] for the

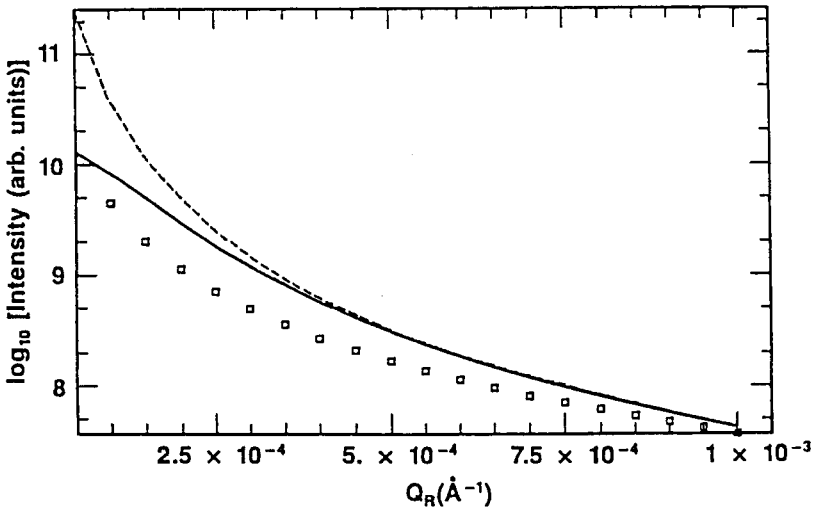


**FIGURE 20.** Diffuse scattering $S_{\text{diff}}(\mathbf{q}_r)$ calculated in the Born approximation by Sinha et al.[139] for a single rough surface with self-affine roughness as defined in Eq. (29). The plot presents portions of three transverse scans for incident angles greater than the specular value with no collimation effects included. The solid curve is for the case of $h = 0.5$, $\sigma = 7$ Å, and a cutoff length, $\xi$ of 7000 Å. In the idealized case that there is no cutoff, the diffuse scattering diverges at the specular condition as shown by the dashed curve. For a more jagged surface with cutoff, $h = 0.2$, $\sigma = 7$ Å, and $\xi = 7000$ Å, the intensities, shown as open squares, are somewhat lower. (Reproduced from reference 139 with permission.)

self-affine solid surface model given in Eq. (29) are reproduced in Figure 20. For the self-affine interface $S_{\text{diff}}(\mathbf{q}_r)$ diverges at the specular condition if no cutoff length is accounted for, but is independent of cutoff for large $\mathbf{q}_r$. On the other hand, $S_{\text{diff}}(\mathbf{q}_z)$, not shown here, appears to be independent of cutoff for all $\mathbf{q}_z$, although this result is known to be invalid for small $\mathbf{q}_z$. These authors[139] also solve Eq. (99) for a liquid surface with capillary waves as described by

$$g(R) = A + B \ln(R) \qquad (100)$$

when allowing for the existence of a cutoff length due to the coherence of the beam. $S(\mathbf{q}_r)$ calculated for this specific case is plotted in Figure 21 for three values of the coefficient, $B$, and perfect resolution. The scattering is always strongly peaked at the specular condition, $\mathbf{q}_r = 0$, with the ratio of peak to tail intensities decreasing as $B$ increases. The peak width increases as the coherence length scale cutoff decreases. As illustrated in Figure 21b, the limiting slope of the diffuse scattering tail changes with $q_z$.

Superior results may be obtained by using the DWBA approach of Sinha et al.[139] or Pynn[142] or the method of Névot and Croce.[143,144,187] In the DWBA a perturbation to the solution for a smooth surface is considered. A few aspects of the method must be mentioned to clarify our notation illustrated in Figure 22, which was adapted from Sinha et al.[139] The X-rays are considered to obey everywhere the stationary wave equation with the interaction potential, $V$, describing the interface taken to be

$$C(x, y) = V_1(x, y) + V_2(x, y)$$

Potential $V_1$ corresponds to the average smooth interface and the wave vector of the beam incident on this surface is $\mathbf{k}_1$. The reflected and transmitted waves for the smooth surface problem are denoted by $\mathbf{k}'_1$ and $\mathbf{k}'_1$, respectively. $V_2$ is the perturbation on $V_1$ due to roughness and we consider a time reversed scattering problem for this rough surface with an incident wave vector $-\mathbf{k}_2$. The corresponding specularly reflected wave is described by vector $-\mathbf{k}'_2$ and the transmitted beam by $-\mathbf{k}'_2$. Note that the DWBA solution is applicable for a general case where $\mathbf{k}_1$ and $\mathbf{k}_2$ are not necessarily related by specular reflection.

The diffuse scattering found from the form of the DWBA used by Sinha et al.[139] is

$$\left[\frac{d\sigma}{d\Omega}\right]_{\text{diff}} = L_x L_y \frac{|k_0^2(1 - n^2)|^2}{16\pi^2} \cdot |T_i(\mathbf{k}_1)|^2 |T_i(\mathbf{k}_2)|^2 S(\mathbf{q}^t) \qquad (101)$$

where $\mathbf{k}_1$ and $\mathbf{k}_2$ are the incident and scattered wave vectors, respectively, $k_0$ is the magnitude of the wave vector in free space and $S(\mathbf{q}^t)$ is

$$S(\mathbf{q}^t) = \frac{1}{|q_z^t|^2} e^{-[(q_z^t)^2 + (q_z^{t*})^2]\sigma^2/2} \iint_{S_0} dX\,dY \, e^{i(q_x X + q_y Y)} \left(e^{|q_z^t|^2 C(X,Y)} - 1\right) \qquad (102)$$

Daillant and Bélorgey's DWBA result[143] is identical to Eq. (101) while Pynn[142] obtains a slightly different form which lacks the explicit symmetry in $\mathbf{k}_1$ and $\mathbf{k}_2$ but gives numerically indistinguishable results in most cases. The DWBA result differs from the Born approximation result, Eq. (99), in two ways. First, it includes the factors $|T_i(\mathbf{k}_1)|^2 |T_i(\mathbf{k}_2)|^2$, involving the moduli of the Fresnel transmission coefficients of the smooth average surface

$$T_i(\mathbf{k}_j) \equiv \frac{2k_{j,z}}{k_{j,z} + k_{j,z}^t} \qquad (103)$$

$T_i(\mathbf{k}_2)$ refers to the time reversed scattering problem of a beam with wave vector $-\mathbf{k}_2$. A second difference is that $q_z^t$ is used in place of $q_z$. For $\mathbf{k}_1, \mathbf{k}_2 \gg k_c$ the factors $|T_i|$ approach unity and $q_z^t$ approaches $q_z$ so that the DWBA result approaches the Born approximation result as it should. An important feature predicted by the inclusion of the transmission coefficients in Eq. (101) is the presence of a maximum in the diffuse scattering when either $\mathbf{k}_1$ or $\mathbf{k}_2$ makes an angle with the surface equal to $\theta_c$. These maxima

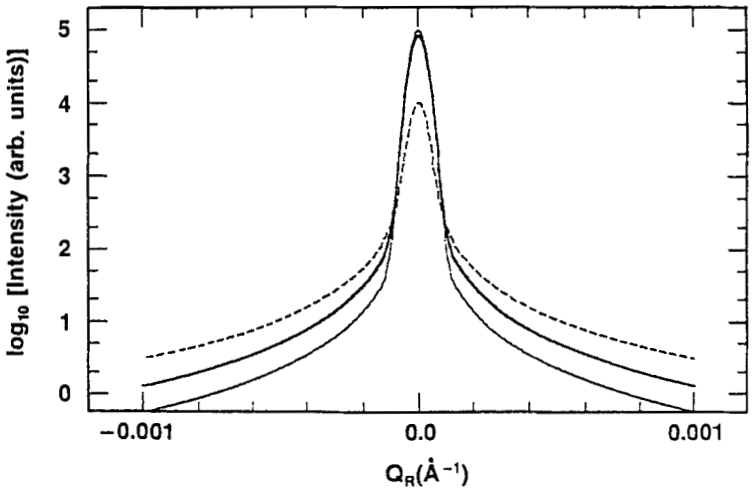


(a)

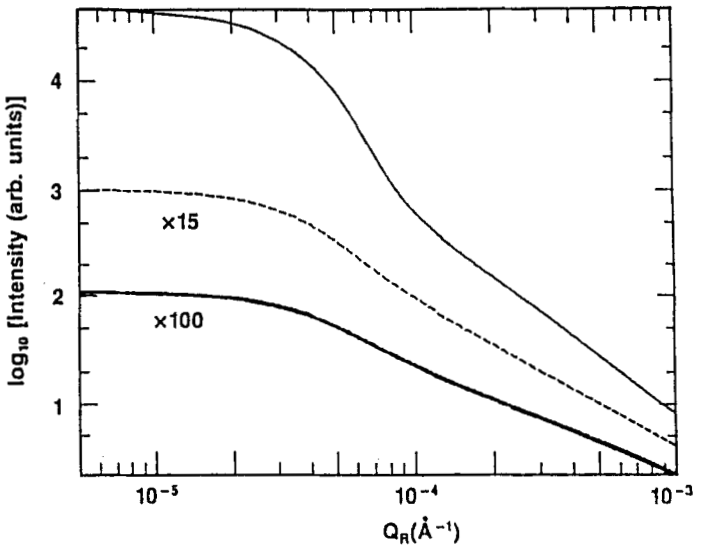


(b)

**FIGURE 21.** Diffuse scattering for the liquid surface calculated in the Born approximation by Sinha et al.[139] for a liquid surface described by Eq. (100) with A = 0 and a cutoff length $\zeta = 1 \times 10^5$ Å due to the coherence length of the incident beam. (a) As $B$ increases from 0.2 (solid, thin line) to 0.5 (bold line) to 5.0 (dashed) the peak to tail ratio decreases ($q_z = 0.3$ Å$^{-1}$). (b) A log-log plot shows different values for the limiting slope as $q_z$ is varied for a surface with $B = 8$: $q_z = 0.2$ Å$^{-1}$ (solid line), $q_z = 0.4$ Å$^{-1}$ (dashed line), $q_z = 0.5$ Å$^{-1}$ (bold). (Reproduced, with permission, from reference 139.)

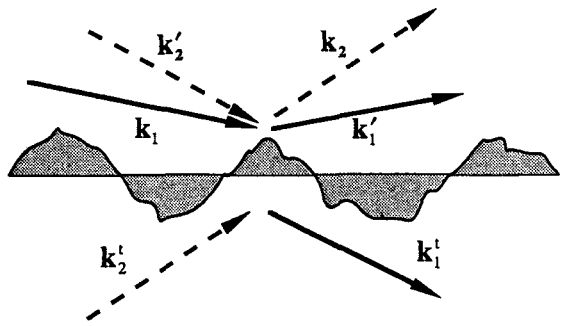


**FIGURE 22.** Definition of the wave vectors for the smooth surface (solid line) and time-reversed rough surface (broken line) solutions considered in the DWBA. (Adapted from reference 139.)

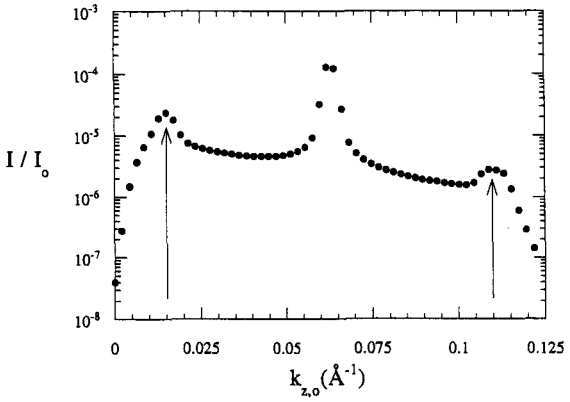


**FIGURE 23.** Intensity as function of incident angle for a "rocking curve" or "transverse scan" in which the detector position is held constant while the sample is rotated to vary $\mathbf{k}_1$. The sample is a LB multilayer containing layers of both cadmium arachidate (CdA) and a novel polyglutamate copolymer[108] for which the measured reflectivity curve appears in Figure 12. The scattering vector $q_z$ is set at 0.122 Å$^{-1}$ and the intensities have been normalized to the incident intensity. Note in particular the Yoneda peaks, marked with arrows, which correspond to $\theta_0 = \theta_c$ and $\phi = \theta_c$.

are illustrated in Figure 23 for a scattering experiment in which the sample is rocked while holding the angle $\theta_1 + \phi$ constant. Such peaks were first observed by Yoneda[126] and are often identified with his name.

Sinha and coauthors[139] point out that when $q_z^t$ is very small, two exponential terms in the DWBA scattering factor $S(\mathbf{q}_z^t)$ may be expanded to give

$$S(\mathbf{q}_z^t) = \iint_{S_0} dX\,dY\,C(X,Y)e^{i(q_x X + q_y Y)} \tag{104}$$

Therefore, the diffuse scattering for $q_z\sigma \ll 1$ yields directly the Fourier transform of the height–height correlation of the surface roughness.

Braslau et al.[146] consider the off-specular scattering from a liquid surface with thermally excited capillary waves using a Green's function approach and obtain for the differential cross-section:

$$\frac{d\sigma}{d\Omega_{\text{diff}}} = L_x L_y \frac{(r_0\rho_e)^2}{\theta}|T_i(\mathbf{k}_1)|^2|T_i(\mathbf{k}_2)|^2 \cdot\left[\frac{k_B T}{\gamma|\mathbf{q}_{xy}|^2 + \rho g}\right] \tag{105}$$

where $A_0$ is the illuminated area, $\theta_0$ is the incident angle, $\mathbf{q}_{xy} = (\mathbf{k}_2 - \mathbf{k}_1)\cdot\mathbf{r}_{xy}$. This result is only valid for weak, diffuse scattering, and though it includes the Fresnel coefficients it does not contain the exponential attentuation factor seen in Eq. (102). The authors therefore correct their result for larger $q$ by multiplying by $e^{-\sigma_T^2 q_z^2}$, where $\sigma_T$ is a total roughness parameter.

Sanyal et al.[151] use the DWBA formalism of Sinha et al.[139] to analyze the liquid surface surface scattering using a form for the correlation function that is very similar to that of Braslau et al.[146] In such a case the scattering cross-section and diffuse scattering structure factor are given by Eq. (101) and (102), respectively. Both the exponential attenuation factor and the Fresnel coefficient terms appear in the result without recourse to inclusion of a correction term. Similar DWBA expressions are also obtained by Daillant et al.[143,153] using a slightly different form for $C(X,Y)$.

Pynn[142] extends the calculation of diffuse scattering to the case of a film with one or two rough interfaces. For two rough inter-

faces he finds

$$\left[\frac{d\sigma}{d\Omega}\right] = L_x L_y \iint_{S_0} dX\,dY\, e^{-i(q_x X + q_y Y)} \cdot \Bigg\{ (r_0\rho_f)^2 \sum_{n=1}^{n=6} \frac{(-1)^{n+1}}{f_n g_n} \cdot F_n e^{-(f_n^2+g_n^2)\sigma^2/2} \cdot \Big\{ \exp\big[(-1)^{n+1} f_n g_n C(X,Y)\big] - 1 \Big\} + (r_0\rho_s - r_0\rho_f)^2 |T_f(k_1)|^2 |T_f(k_2)|^2 \cdot \frac{\exp\big[-(\gamma^2 + \gamma^{*2})\sigma_2^2\big]}{|\gamma|^2} \cdot \big[\exp\big[|\gamma|^2 \langle \eta(X,Y)\eta(0,0)\rangle\big] - 1\big] + (r_0\rho_s - r_0\rho_f)(r_0\rho_f)\,\mathrm{Re} \sum_{n=1}^{n=4} \frac{(-1)^{n+1}}{f_n \gamma} G_n e^{-(f_n\sigma_1^2 + \gamma\sigma_2^2)/2} \cdot \Big\{ \exp\big[(-1)^{n+1} f_n \gamma \cdot \langle \eta(X,Y)\xi(0,0)\rangle - 1\big] \Big\} e^{i\gamma t} \Bigg\} \tag{106}$$

where $\gamma = k_{1z}^s + k_{2z}^s$ and the wave vectors $k_{1z}^s$, $k_{2z}^s$ are evaluated in the substrate material. The functions $f_n$, $g_n$, $F_n$, and $G_n$ are all defined in terms of the Fresnel transmission and reflectivity coefficients $T_i(\mathbf{k}_j)$ and $R_i(\mathbf{k}_j)$ of the air/film and film/substrate interfaces with

$$R_i(\mathbf{k}_j) \equiv \frac{k_{j,z} - k_{j,z}^t}{k_{j,z} + k_{j,z}^t} \tag{107}$$

The electron densities of the film of thickness $t$ and substrate are given by $\rho_f$ and $\rho_s$, respectively. Height coordinates of the air/film and film/substrate interfaces are given by $\xi$ and $\eta$ and the corresponding roughness standard deviations by $\sigma_1$ and $\sigma_2$. Scattering from a rough film on a smooth substrate is captured by the first term. The second incorporates scattering from the rough film/substrate interface. The third term is only needed when correlations exist between the two interface roughnesses. When the two are perfectly correlated $\xi = \eta$ and the interfaces are said to be "conformal". Garoff et al.[157] have argued that if two interfaces are conformal, oscillations in the diffuse scattering at $q_x = 0$ will be in phase with oscillations in the specular reflectivity. Pynn[142] remarks this is true provided the dominant oscillatory contribution comes from the final term in Eq. (106), which requires that the X-ray contrast between film and substrate be sufficiently large. If the film has a negative scattering length density for neutrons, the diffuse neutron scattering from correlated roughness will be exactly out-of-phase with the neutron reflectivity, allowing for a sensitive complementarity between X-ray and neutron measurements. Daillant and Bélorgey[143] present some examples of the off-specular scattering one may expect to see in the case of a single thin film with two rough interfaces. Pynn[142] has done this also, but presents the results in the form of two-dimensional plots typical of time-of-flight neutron reflectivity measurements.

Further extensions of the theory to more complex systems are provided by other authors. Stearns[141] has given equations for the off-specular scattering from multilayers with rough interfaces in the region away from the critical angle using the so-called specular approximation, in which the transmitted and reflected specular fields are computed using a full dynamical treatment while the diffuse fields from each interface are considered kinematically. Daillant and Bélorgey[143-144] have very recently considered the case of two rough surfaces as well as the generalization to stratified media with $N$ strata following the method of Croce and co-workers.[136-138] They argue that this description also may be straightforwardly applied to bulk scattering in thin films as well. The discussion focuses on the result for a single rough film on a

rough substrate and their results simplify to those of Pynn.[142]

Off-specular scattering from multilayer samples having surface domains, such as illustrated schematically in Figure 24, has been analyzed by Cai et al.[145] Their expressions for the scattering are based on the specular approximation used by Stearns[141] and thus the diffuse scattering is described appropriately only away from the critical edge. Assuming that the average surface domain size is much larger than the correlation length the authors arrive at the following working expression for the diffuse scattering cross-section:

$$\left[\frac{d\sigma}{d\Omega}\right]_{\text{diff}} = L_x L_y \sum_{ij}^{N} \alpha_i \alpha_j \sum_{m=i-1}^{i} \sum_{n=j-1}^{j} \cdot(-1)^{n+m+i+j} \frac{\rho_m \rho_n^*}{q_{z,m} q_{z,n}^*} \cdot \exp\left[-i\left((q_{z,m} z_i - q_{z,n}^* z_j\right)\right] \cdot \exp\left[-\left(q_{z,m}^2 \sigma_i^2 + q_{z,n}^{*2} \sigma_j^2\right)/2\right] \cdot \int_{L_x}\int_{L_y} dX\, dY P_{ij}(X,Y) \cdot \exp\left[-i(q_x X + q_y Y)\right] \quad (108)$$

The interface indices $i$ and $j$ vary from 1 at the polymer/air interface to $N$ at the polymer/substrate interface, and the layer indices $m$ and $n$ range from 0 for air to $N$ for substrate. The remaining parameters are $\rho_m$, the scattering length density of the layer $m$, $q_{z,m}$, the momentum transfer in layer $m$, $q_x$ and $q_y$ are the lateral momentum transfer components, $z_i$ is the average height of interface $i$, and $\sigma_i$ is the root mean square roughness of interface $i$. $P_{ij}(X,Y)$ is the coherent

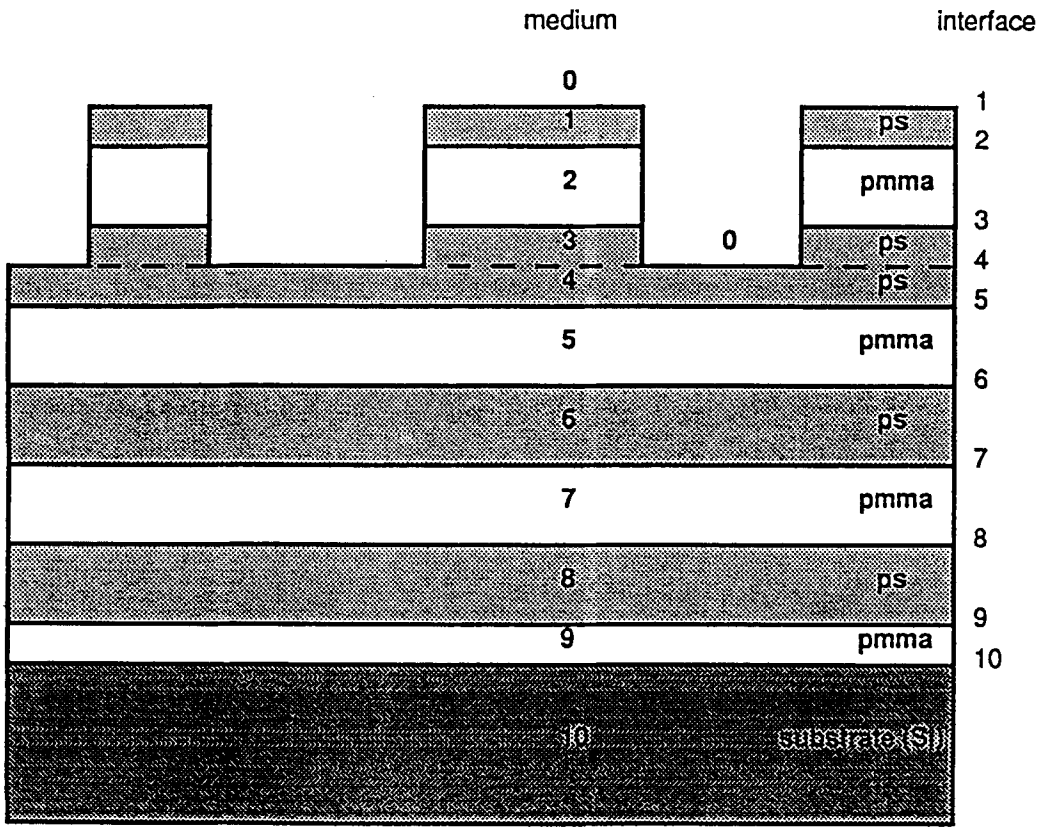


**FIGURE 24.** Schematic cross-section of the model structure used by Cai et al.[145] to analyze X-ray scattering data from an ordered polystyrene (PS) block polymethylmethacrylate (PMMA) film with surface domains. (In real systems a thin PS layer is presented to the air at all points on the sample surface.) (From reference 145, with permission.)

portion of the total domain–domain and roughness correlation function between interfaces $i$ and $j$

$$P_{ij}(X,Y) = h(X,Y)R_{ij} + h(X,Y) + R_{ij}$$
$$i,j \leqslant l-1$$
$$= \frac{\alpha^2 h(X,Y)R_{ij}}{(1-\alpha)^2} + \frac{\alpha^2 h(X,Y)}{(1-\alpha)^2} + R_{ij}$$
$$i,j = l$$
$$= R_{ij} - \frac{\alpha h(X,Y)}{1-\alpha} - \frac{\alpha h(X,Y)R_{ij}}{1-\alpha}$$
$$i \leqslant l-1, j = l \quad \text{or}$$
$$i = 1, j \leqslant l-1 \qquad (109)$$

where $l$ is the index of the layer supporting the surface domains, $\alpha$ is the domain surface coverage, and $\alpha_i$ is the coverage of interface $i$. $\alpha_i$ is equal to $\alpha$ if the interface contains domains, (1-$a$) if the interface supports domains, or 1 if the interface is completed.

Domain–domain correlations are represented in the terms containing $h(X,Y)$ and roughness correlations represented in $R_{ij}$, with $R_{ij}$ being the coherent diffuse scattering contribution

$$R_{ij}(q_{z,m}q^*_{z,m}; X,Y)$$
$$= \exp\left[q_{z,m}q^*_{z,n}C_{ij}(X,Y)\right] - 1 \quad (110)$$

and $C_{ij}(X,Y)$ the height–height correlation between interfaces $i$ and $j$. The diffuse scattering caused by surface domain scattering will be evidenced by coherent off-specular scattering along $q_z$ even when the roughnesses of the surface domains is not correlated with that of other interfaces. However, Cai et al.[145] remark that the diffuse scattering due to domains differs from that of correlated roughness. While the above equations are derived for the case where the domains are at the surface and the domain heights are uniform, they may be more generally applied to films with domains of arbitrary shape at the surface or below the surface. It is necessary only to divide the total film thickness into many layers such that the domain heights are uniform in each and then determine the correlation functions within each layer and between pairs of layers.

### c. Calculation of Experimentally Measurable Intensities

Several authors[17,79,139,142,143,151] discuss the importance of carefully accounting for two effects when calculating observable intensities from systems with appreciably diffuse scattering. First, it is essential to account for the diffuse scattering contribution which is observed in the specular ($q_x = q_y = 0$) direction and is unavoidably measured along with the true specular beam when performing a specular scan. If one wishes then to model the experimental "reflectivity" curve he must either add the appropriate diffuse scattering to the model specular intensity or subtract an estimate of the diffuse contribution from the measured reflected intensity. In some cases[186] one may be able to properly estimate the diffuse scattering at the specular condition by measuring its magnitude for a finite value of $q_x$ (or $q_y$) such that the specular reflection at $q_x = q_y = 0$ is outside the resolution volume. If the interface has long-range correlations or the resolution of the spectrometer is insufficient to allow this experimental separation of the specular and diffuse contributions, the diffuse intensity will have to be calculated.

While the $q_x$ and $q_y$ resolutions sometimes may be neglected in calculating a specular intensity without harm, they must be accounted for explicitly to obtain proper diffuse intensities, because absolute intensities must be considered to obtain quantitative information. The differential scattering cross-section must be integrated over the detector solid angle $\Omega_d$ and incident beam angular spreads $\Delta\theta$ and $\Delta\psi$ parallel to and perpendicular to the plane of incidence, respectively. As a simple example, if we assume a Gaussian line shape for the incident beam and a very narrow distribution for $\lambda$, the

"measured" intensity[143] $I_D$ is

$$I_D = \frac{1}{L_x L_y}\int d\delta\,\theta\, d\psi \frac{1}{2\pi\Delta\theta \times \Delta\psi} \cdot \exp\left(-\frac{\delta\theta^2}{2\Delta\theta^2} - \frac{\delta\psi^2}{2\Delta\psi^2}\right)\int \frac{d\sigma}{d\Omega}\, d\Omega_d \tag{111}$$

where $\delta\theta$ and $\delta\psi$ are the differences between actual and nominal values for $\theta$ and $\psi$. Because the scattering cross-section is generally given in terms of $\mathbf{q}$, the integration over $d\delta\theta_s\, d\Omega_d$ may be replaced by one over $\delta\mathbf{q}$ in practice.[79] That is, the resolution is accounted for by convolution of $d\sigma/d\Omega$ with a Gaussian resolution function $W(\delta\mathbf{q})$. We may consider as an example the simplest case corresponding to the specular condition. In that case we have

$$\Delta q_x = k_0 \sin\theta \max(\Delta\theta, \Delta\phi) \tag{112a}$$

$$\Delta q_y = k_0 \Delta\psi \tag{112b}$$

$$\Delta q_z = k_0 \max(\Delta\theta, \Delta\phi) \tag{112c}$$

To account for the difference in density of wave vectors projected in the Fourier space as compared to angular space we must include a factor

$$\frac{1}{2} k_0^2 q_z \max\left(\frac{\Delta\theta}{\Delta\phi}, \frac{\Delta\phi}{\Delta\theta}\right)$$

Typically, $\Delta\phi > \Delta\theta$ and then

$$I_D = \frac{1}{L_x L_y}\frac{1}{\sqrt{2\pi}\,\Delta\theta}\int \frac{2\Delta\theta}{k_0^2 q_z' \Delta\phi}\frac{d\sigma}{d\Omega} \cdot(\mathbf{q}' + \delta\mathbf{q}')d\delta\mathbf{q}' W(\delta\mathbf{q}') \tag{113}$$

We see that the measured diffuse scattering intensity always increases as the acceptance of the detector is increased, in contrast to a measured true specular intensity, which no longer increases with detector acceptance above a minimum acceptance necessary to capture the divergent specular beam. Therefore, the ratio of specular to diffuse intensity will be most advantageous for obtaining the corrected specular curve when the resolution is very good.

### 3. Performing the Experiments

Grazing incidence off-specular scattering measurements may be done in at least four ways. Differences and similarities among these may be seen in Table 1, which summarizes the quantities varied in each type of measurement as well as in a specular reflectivity measurement. Transverse scans, also called rocking curves, represent the measurement of diffuse scattering at various values of $q_x$, keeping $q$ constant. They are performed by fixing $2\theta$, the angle between incident and scattered directions and then varying the angle of incidence. Therefore, $q_z$ varies slightly and the penetration depth varies. Changing

**TABLE 1**
**Comparison of Specular and Off-Specular Measurements**

| Scan type | Parameter space probed | | | |
|---|---|---|---|---|
| | $q_z$ | $q_x$ | $q_y$ | $z_0$ |
| Specular | $q_{z,\min}$ to $q_{z,\max}$ [a] | 0 | 0 | $z_0(k_{z,\min})$ to $z_0(k_{z,\max})$ |
| Transverse | $q_z$ nearly fixed | $-k_{x,s}$ to $+k_{x,s}$ | 0 | $z_{0,\min}$ to $z_0(k_{z,\text{spec}})$ |
| Detector | $-k_{z,0}$ to $q_{x,\max}$ | $-k_{x,0}$ to $k_{x,s,\max}$ | 0 | $z_0(k_{z,0})$ |
| Longitudinal | $q_{z,\min}$ to $q_{z,\max}$ | ca. $q_{x,0}$ | 0 | $z_0(k_{z,\min})$ to $z_0(k_{z,\max})$ |
| $q_y$ | Fixed $q_z$ | Fixed $q_x$ | $q_{y,\min}$ to $q_{y,\max}$ | $z_0(k_{z,0})$ |

[a] Minimum and maximum values of q and k components can be set by experimenter within constraints of apparatus.

the incident angle is often done by rotating the sample, although for liquid samples both incident and detector spectrometer arms must be moved. An example of a transverse scan from an LB multilayer containing a polymeric bilayer is shown in Figure 23. The most prominent feature in data of this type are the Yoneda peaks, which are visible for all types of samples. The remainder of the curves are generally smooth and less striking, although it may be possible to observe weak oscillations characteristic of a correlation length in the surface structure.

The second type of small angle off-specular measurement, which we term simply "detector scan" is done by fixing the incident angle and scanning through the detector angle[142-144,147] $\phi$ in the plane of incidence. For these scans $q_x$ increases slowly as $q_z$ is increased away from the specular condition. Trajectories in the $q_x, q_z$ plane for one example set of such measurements is shown in Figure 25. Scans of this type show considerable structure for films having thicknesses of a few tens of nanometers as illustrated by the examples in Figure 26. This structure will in general include three contributions corresponding to height–height correlations at the air/film interface, at the film/substrate interface, and between the two interfaces. Oscillations of period $\Delta q_x = 2\pi/d$ result from correlation between interfaces, while the contribution from correlation within the

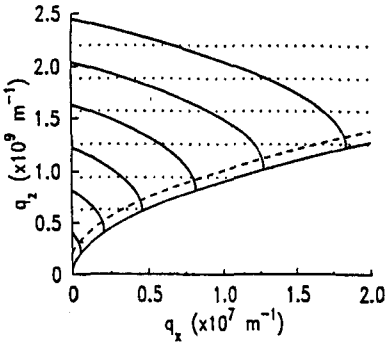


**FIGURE 25.** Trajectories followed in a scan through detector angle for fixed incidence angle $\theta_0 = 1.43°$ and $CuK_\alpha$ radiation. (From reference 143, with permission.)

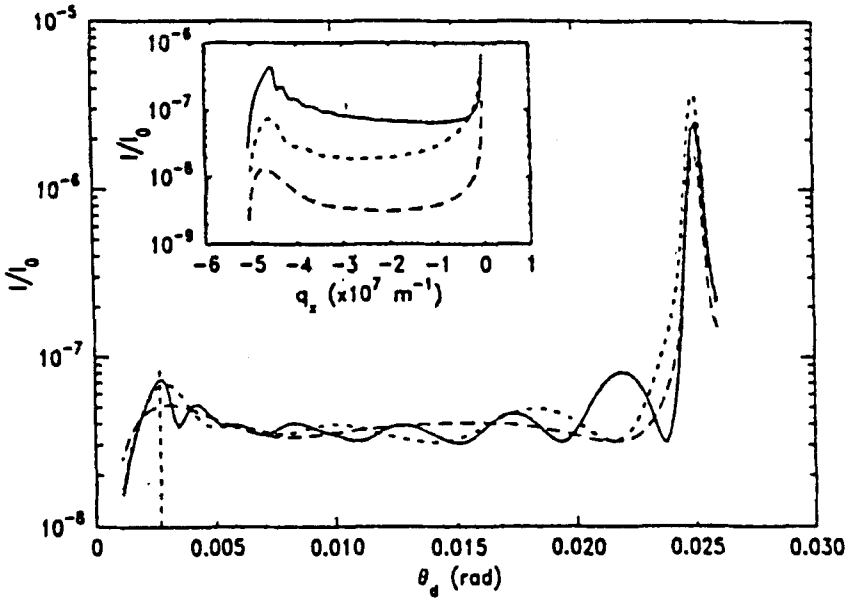


**FIGURE 26.** The effect of film thickness on the diffuse scattering from thin liquid films as expected from detector scans[143] is shown for the case of a freely suspended film of thicknesses 10 nm (dashed line), 20 nm (dotted line), and 35 nm (solid line). The critical value of the detector angle $\theta_d$ is indicated by the vertical dashed line. Variation in the diffuse scattering with thickness is shown in the inset for scans through $q_x$ and constant $q_z$. (From reference 143, with permission.)

air/film interface may contain oscillations of period $\pi/d$, which appear at detector angles close to critical. Wu[147] also gives example scattering results from this type of scan calculated for thin films.

In the third type of measurement, called a longitudinal scan, $q_z$ is varied while keeping $q_x$ constant at some value equal to a small fraction of $q_z$.[154] A measurement of this sort is approximated by scanning the incident and detector angles simultaneously with the detector angle always offset from the specular condition by a fixed value. An example[174] of a block copolymer thin film is presented in Figure 27. In the case that the contrasts at the film/air and film/substrate interfaces are large enough, the oscillations in the off-specular scan will be of the same period and in phase with those in the reflectivity curve if the film/air and film/substrate interfaces are correlated. Thus, such a scan presents a qualitative way to assess this correlation in a thin film sample.

The final type of small angle off-specular measurement discussed here is one in which the incident angle is constant and the detector scanned out of the incidence plane, probing a range for $q_y$ values about zero for constant $q_z$ and constant penetration depth. While the first three types of small angle off-specular measurement described may often be done with a beam which is much larger in the $y$ direction than in the $x$ direction, this $q_y$ scan requires comparable resolution for both. If the incident angle is set at or below the critical angle of the film, and the film thickness exceeds the penetration depth of the evanescent wave, the resulting scattering is related only to the film structure and scattering from the substrate does not interfere. This measurement differs from the transverse scan (rocking curve) in that $q_z$ is held absolutely constant and thus only the in-plane dimension is probed. Also, the penetration depth is held constant here. The $q_y$ scan also has an advantage over a detector scan in studying film in-plane structure. The incident angle may be held constant at or below critical for the detector scan, but only a very limited range of $q_x$ is available in that case, constraining the study of in-plane correlations. Therefore, this fourth measurement type presents a unique method for probing in-plane inhomogeneities in the sample near-surface region.

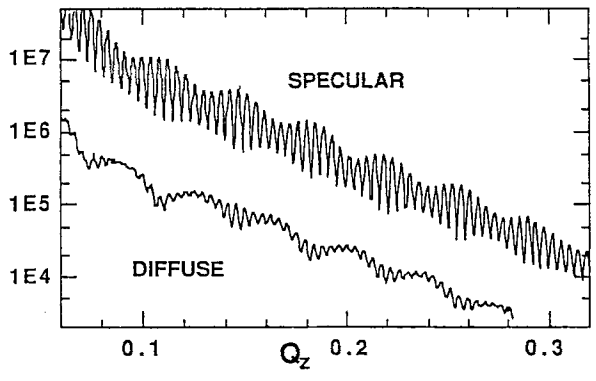


**FIGURE 27.** A longitudinal scan of diffuse scattering from a polystyrene-polymethylmethacrylate block copolymer thin film made by varying the incident and detector angles simultaneously, maintaining a constant offset between detector angle and the specular condition. (Reprinted, with permission, from reference 174.)

Clearly, a combination of these various measurements offers the greatest opportunities for characterizing interfaces because each has unique advantages and limitations. For example, Pynn[142] remarks with regard to characterization of correlations among structures of different interfaces within a sample that simply recording the scattering for small values of $q_x$ as a function of $q_z$ can be misleading. In principle, a two-dimensional map of the scattering as a function of both $q_x$ and $q_z$ is best. Such a map may indeed be available when collecting neutron reflectivity data using a time-of-flight spectrometer (e.g., SPEAR at Los Alamos Laboratory, CRISP at ISIS). Obtaining such a map with an X-ray spectrometer is generally not practical, although with use of a two-dimensional PSD[155] a considerable portion of the $q_z$, $q_x$ space can be investigated.

In another example of the complementarity of different measurements Wu[147] demonstrates how two potential models of the internal density profile of a thin film can yield nearly identical specular results, but are easily distinguished using a detector scan. He

calculates both the specular reflectivity and detector scan off-specular intensities for two samples, each consisting of a uniform, 20-nm thick film on a solid substrate. While the specular reflectivities of the two are nearly identical over the range of $q_z$ studied, $0 < q_z < 0.05$ Å$^{-1}$, the detector scans are readily distinguished, as seen in Figure 28.

## 4. Instrumentation

The instrumental requirements for performing off-specular scans are of two types: movement and resolution. In order to perform $q_y$ scans one must be able to move a counter perpendicular to the plane of incidence or one may use a PSD[188,189] with its axis along the $y$ direction. The component movements necessary to perform the first three off-specular scattering measurements described above are generally available in the apparatus used to perform reflectivity measurements. Indeed, transverse scans and detector scans over limited angular ranges are commonly required in the course of spectrometer and sample alignment. Longitudinal scans are also commonly performed as a means of properly estimating (on a purely empirical basis) the background/diffuse scattering correction for the reflectivity curve. In this sense the explicit pursuit of off-specular measurements often represents a quantitative rather than a qualitative extension of one's experimental effort.

Some off-specular measurements may present resolution requirements not met by an apparatus quite serviceable for many reflectivity measurements. Because separation of the specular and diffuse scattering is often intrinsically difficult, instruments presenting good incident beam resolution will have an advantage. The use of double or triple bounce monochromators can aid in this separation by assuring that the $q_y$ resolution is very good and that the incident beam profile drops off very sharply. If the features to be studied are very large, e.g., micron-sized surface domains of diblock films, high resolution is imperative. In most cases the collimation of the beam in the direction perpendicular to the

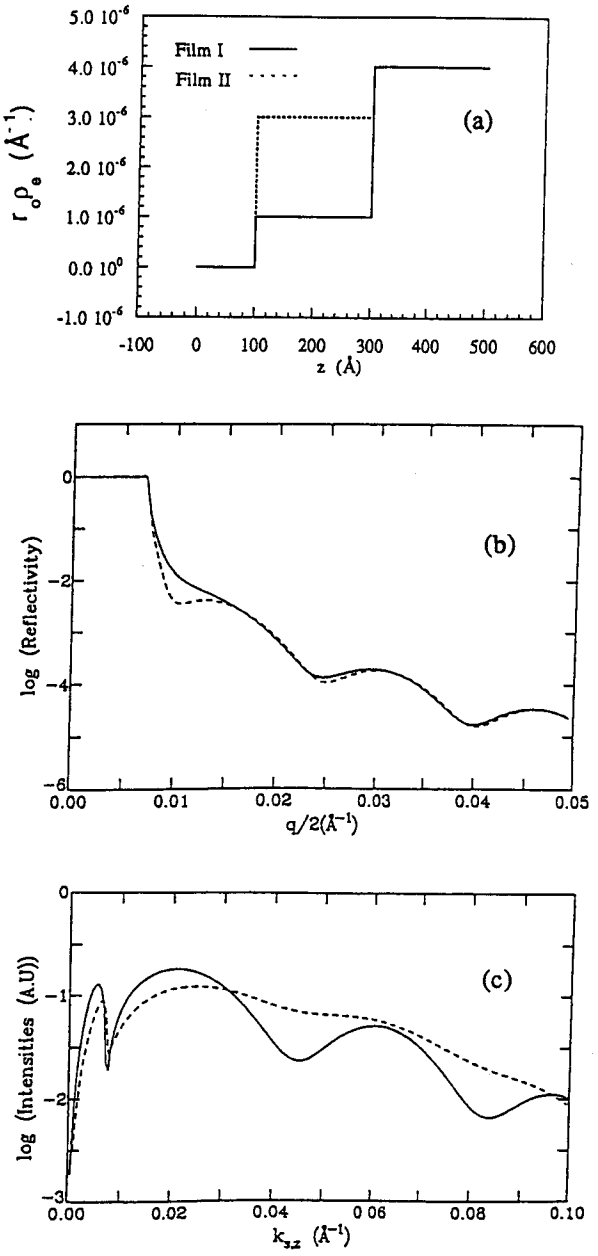


**FIGURE 28.** The advantage of complementing specular reflectivity with off-specular measurements is demonstrated for the simple case of a 20-nm thick homogeneous thin film on a substrate. Scattering length density profiles for films of two different scattering length densities are shown in (a). While the specular reflectivities for film I (solid line) and film II (dashed line), shown in (b) are nearly identical, the calculated intensities for detector scans from each sample, shown in (c), are markedly different. These latter scans are performed at an incident angle above the critical angle of the film in case I, but less than the critical angle of the film in case II. (Reprinted, with permission, from reference 147.)

incident plane can be relaxed compared to that in the scattering plane, in order to improve intensity. However, use of a beam finely collimated in both directions allows one to study the variation of surface structure across the sample.[84] At the specular direction the resolution in $q_x$ is given by $k_0 \sin \theta_0 \max (\Delta\theta_0, \Delta\phi)$.[143] The $q_x$ resolution actually demanded will depend on the scale of the surface features under study.

The relative diffuse scattering intensities of interest may be as low as $10^{-8}$ to $10^{-7}$ and thus the signal to noise ratio is even more critical than for some reflectivity measurements. Most diffuse scattering studies published to date have used synchrotron sources,[145,150,151,154,157,158] which provide time-efficient measurements of even such weak scattering. However, it may also be possible in some cases to adequately tackle a diffuse scattering problem using a rotating anode source[174] or sealed tube anode,[84] providing one is not limited by time and background scattering is aggressively limited. Daillant and co-workers[84] have made measurements with a fine focus sealed source. They use a primary $^{111}$Si crystal monochromator and a slit to limit background to 10 counts per 300 s above the detector noise of 30 counts per 300 s.

Previous remarks regarding sample quality for reflection measurements generally pertain here as well. However, two authors have been able to study samples which are not flat over large distances (i.e., centimeters) by using finely collimated beams. Daillant et al.[84] have considered spreading drops of polydimethylsiloxane and Pershan and coworkers[156] have studied the macroscopically curved surface of Gallium liquid metal.

### 5. Applications

Because the measurement of diffuse scattering has been so recently developed, it is interesting to note its use with some other systems as well as with polymers. The earliest quantitative interpretations of diffuse spectra were performed for a single glass/air interface with limited microroughness.[139] Sinha et al.[139] showed a comparison of specular, longitudinal diffuse scattering and transverse scans from Pyrex glass with theoretical curves computed using their DWBA expression and a power law correlation function with cutoff. The form of the longitudinal diffuse scattering was represented well.

The roughness of water[150] and ethanol[151] surfaces also have been studied. The amplitude and shape of the Yoneda peaks and their tails are sensitive to the scattering cross-section from the surface roughness and specifically to the height–height correlation function. The excellent agreement between theory and experiment for both specular and transverse scans in the work of Schlossman et al.[150] demonstrated that the capillary wave model is a good representation of the height–height correlation over a region of reciprocal space when only thermally excited capillary waves are present. This means capillary waves may be properly accounted for when measuring other systems in which additional mechanisms (e.g., surface elastic modes) play a role in determining the surface topology.

Sanyal et al.[151] have considered the X-ray scattering from capillary waves more recently using the formulation of Sinha et al.[139] in analyzing their data. This approach yields a nearly identical result for the nominal specular reflection as found by Braslau et al.[146] In addition, however, it yields explicitly the power law tails in the diffuse scattering.

Garoff et al.[157] and Tidswell et al.[154] have used off-specular scans to study the conformality of roughnesses between the two interfaces of wetting liquid layers on substrates. Garoff et al. studied a water layer on glass and argued for conformality of the interfaces based on a similiarity in oscillatory behavior of specular and longitudinal diffuse scans. Because the roughness of the glass substrate exceeded that of the surface of a sample of bulk water this conformality had the effect of making the surface of the ultrathin layer rougher than that of bulk water. Tidswell et al. also used longitudinal diffuse scattering scans to demonstrate conformality between the air/film and film/substrate interfaces for a silicon substrate wet by cyclohexane vapor.

For film thicknesses less than about 60 Å the film surface was constrained to follow the height variations of the substrate/liquid interface. For thicker films the roughness of the free surface was dominated by thermally induced capillary waves.

In a pair of publications dealing with both theoretical and experimental aspects, Daillant and Bélorgey[143,144] studied the correlation between the two free surfaces of draining soap films, using an experimental geometry which has considerably poorer resolution in the $y$ direction than in the $x$ direction. In this case, one essentially averages over the $y$ direction and the correlation function of interest is one having a variation only with $X = x' - x$. The particular correlation function they consider is

$$\begin{aligned}\langle z_1(0)z_1(X)\rangle &= \langle z_2(0)z_2(X)\rangle \\ &= \alpha[K_0(GX) + K_0(X/a_{\max}) \\ &\quad -2K_0(X/a_{\min})] \end{aligned} \tag{114}$$

where $K_0$ is the modified Bessel function[152] of the second kind of order zero. It is a reasonable model correlation function for systems exhibiting long-range correlations, including liquids. The correlation between the air/film and film/substrate interfaces is assumed to have the form

$$\langle z_1(0)z_2(X)\rangle = \alpha[K_0(X/a_{\max}) - K_0(GX)] \tag{115}$$

The parameters of this correlation function are a long wavelength cutoff, $a_{\max}$, a short wavelength cutoff, $a_{\min}$, due for example to bending rigidity or molecular size, and the strength of the correlation between interfaces, $G$. For $X \gg G^{-1}$ the interfaces are sufficiently smooth to be fully correlated, while for $X \ll G^{-1}$ the height variations are rather abrupt and there is only imperfect correlation. Both reflectivity and off-specular measurements are made. Because oscillations characteristic of the film thickness are observable in detector scans with fixed incident angle, these are used rather than rocking curves to study the in-plane surface modes. The contrast of the oscillations in both the reflectivity curve and off-specular scans should increase with increasing $G$. Reducing $a_{\min}$ increases the reflectivity for $q_z > q_c$ and decreases the amplitude of off-specular oscillations at the smallest detector angles. Using these two characteristics the authors are able to determine the two parameters $G$ and $a_{\min}$ separately[144] for free-standing soap films.

Daillant and Bélorgey[143] provide a helpful discussion of the magnitude of diffuse scattering effects and the implications for specular reflectivity analysis for small molecule liquid systems in general and the soap films studied in particular. The ratio of diffuse to specular intensity increases with $q_z$ and while an exact appraisal requires detailed numerical calculations of $S(\mathbf{q})$, this ratio may be conservativly approximated in the low $q_z$ limit as

$$\frac{I_{\text{diff}}}{(I_{\text{diff}} + I_{\text{spec}})} = \frac{\xi^2 q_z^2}{1 + \xi^2 q_z^2} \tag{116}$$

where $\xi$ depends on the roughness, the range of correlation, and the resolution $\Delta q_x$:

$$\xi^2 = \Delta q_x \int_0^\infty dX \langle z(0)z(X)\rangle e^{-1/2\Delta q_x^2 X^2} \tag{117}$$

$\xi$ is the average value of the correlation function on a length scale $\Delta q_x^{-1}$ and should have a value on the order of the roughness. We may use the criterion of $q^2\xi^2 \approx 1$ as a workable estimate of when the diffuse scattering begins to dominate. Using the resolution appropriate to their work, $CuK_\alpha$ ($\lambda$ = 1.54 Å) radiation, and a rms roughness of about 3 Å this approximation predicts that diffuse scattering will constitute $> 50\%$ of the total observed intensity in the specular direction for $\theta_0$ greater than about 40 mrad (2.3°). The success of this type of investigation with small molecule liquids suggests the study of very thin polymer films could be enlightening as well.

While reports of strong off-specular scattering for polymer films have existed for a

few years,[18] quantitative analysis only recently has been undertaken and then only for a few systems. At the moment the author is aware of studies investigating immiscible blend interfaces,[158] diblock copolymer film surfaces,[145] polymer solution surface modes,[160] and the wetting properties of thin elastomeric films.[161]

Zhao et al.[161] use diffuse scattering to measure the roughness of polyethylene propylene (PEP) films of different thicknesses on silicon wafer substrates with and without a native silicon oxide layer. A polymer of molecular weight $M_w$ = 290,000 and radius of gyration, $R_g$ = 214 Å is considered first. Rocking curves from two layers with thicknesses of 167 Å and 2000 Å, reproduced in Figure 29, show clearly the greater roughness at room temperature of the thinner film. This same measurement is also sensitive to a substantial smoothing of the 167 Å thick film which takes place upon annealing at 226°C. Off-specular scans through $q_x$ at constant $q_z$ = 0.10 Å$^{-1}$ for two 80 Å thick films spun on silicon supports show that the film on the wafer without the native oxide is nearly as smooth as the substrate itself, while that on the oxide-coated substrate is much rougher with an in-plane structure having a correlation length of about 1 μm. X-ray measurements from films of other molecular weights and thicknesses, complemented by AFM imaging of the actual surface morphology, indicate that for a given substrate surface energy and temperature the spun cast layers dewet when their thickness drops below a critical value which is roughly equal to the radius of gyration. An expression for effective spreading coefficient which accounts for stretching of the chains in the thin films qualitatively explains the thickness and temperature effects on wetting observed at a given molecular weight, but is unable to account for the molecular weight dependence.

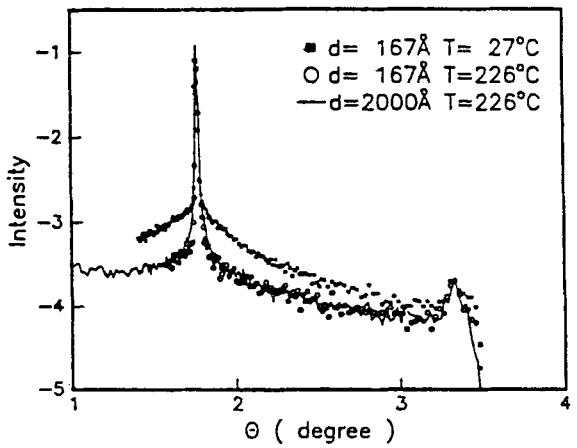


**FIGURE 29.** Rocking curves for $q_z$ = 0.25 Å$^{-1}$ from silicon wafer supported PEP films of thickness 167 Å (filled squares and open circles) and 2000 Å (solid line) are the same at 226°C. A dramatic increase in roughness of the 167 Å thick film when lowering the temperature to 27°C is evidenced clearly in the diffuse scattering. The scattering from the 2000-Å thick film changes little when cooling. (From reference 161 with permission.)

The same research group[158,159] has used specular and diffuse scattering measurements to study the immiscible blend interface between PS and PSBr both above and below the glass transition of the polymers. One of the challenges in the analysis of data of this type is the separation of the effects of interfacial mixing and interfacial roughness.

Diffuse scattering measurements have also been used[160] to study the surfaces of toluene/polybromostyrene (PSBr) and toluene/polystyrene solutions as a function of polymer concentration. For these viscoelastic solutions one might expect both surface elastic waves and capillary modes to contribute to the diffuse scattering. To calculate the expected diffuse intensities the authors build on the results of Pincus et al.[162,163] who derive the dynamic structure factor $S(k,\omega)$ of a concentrated polymer solution using a Maxwell model of the viscoelastic character of the solution. Because the hydrodynamic excitation energy is negligible compared to both the incident beam and detector energy resolutions, a normal X-ray scattering experiment is sensitive only to the static structure factor $S(k)$. $S(k)$ represents an average over all frequencies. In the large $k$ limit $S(k)$ approaches a form representative of capillary modes only, while in the small $k$ limit elastic modes dominate. An analytic form which closely approximates the exact form of $S(k)$ between these limits and also

allows for gravitational effects is

$$S(k) \cong \frac{k_B T}{\gamma\left(k^2 + \left\{\left[c(\tau)E_0 k\right]/\gamma\right\} + \kappa^2\right)} \tag{118}$$

where $\tau$ is the relaxation time, $E_0$ the transient solution modulus, and $c(\tau)$ is a fitting parameter. Backtransforming $S(k)$ to obtain the real space height–height correlation function $C(R)$ and applying approximations appropriate for $c(\tau)E_0 < 10^3$ dyn/cm$^2$ one obtains

$$C(R) \approx \frac{k_B T}{2\pi\gamma}\left[-\ln\left(\frac{\kappa R}{2} - \gamma_E - \frac{\pi c(\tau)E_0}{4\gamma\kappa}\right)\right] \tag{119}$$

where the last term is a correction to the small molecule liquid result incorporating capillary and gravity waves.[151] In the limit considered the correction term is only an additive constant to *C(R)* and the shape of the diffuse scattering is expected to remain unchanged from that of the solvent. Transverse and longitudinal diffuse scans presented by the authors for polybromostyrene ($M_n$ = 90 k, 1 M) in toluene and PDMS ($M_w$ = 1 M) in chlorobenzene for PSBr concentrations up to 11.7 vol% and a single PDMS concentration of 15% confirm this experimentally. Example transverse scan data from a 3.39 vol% 1 M PSBr solution for four different values of $q_z$ are compared in Figure 30 with model curves, which include a constant background due to bulk scattering from the solution. Capillary wave effects dominate the diffuse scattering far into the semidilute regime and the authors postulate that in order for elastic modes to impact the diffuse scattering, systems with $E_0$ exceeding $10^5$ dyn/cm$^2$ will have to be studied.

Surface domains on diblock copolymer thin films[144,174] also have been investigated. Symmetric diblock copolymers can self-assemble into lamellar morphologies containing domains rich in one or the other of the two blocks.[164] When constrained in a thin

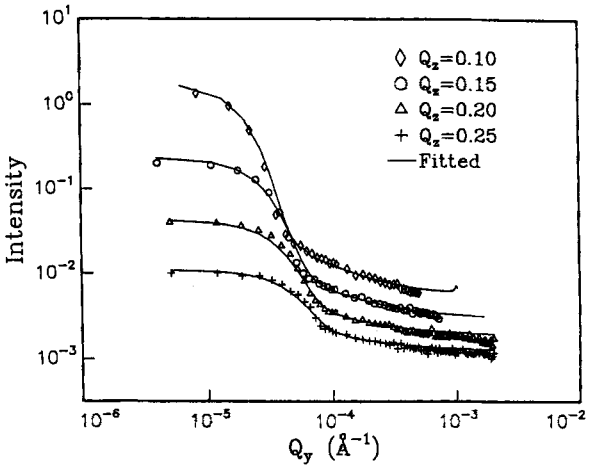


**FIGURE 30.** Transverse scans[160] at three four values of $q_z$ for a 3.39 wt% solution of 1 M mol wt PS in toluene compared with model curves calculated using the correlation function in Eq. (119) and including a constant background due to bulk scattering from the solution. (From reference 160, with permission.)

film geometry where the influence of the surface fields at the air/polymer and polymer/substrate interfaces play an important role, the lamellae are known to align parallel to the surface.[169–173] If the mass of polymer deposited in the thin film is not the proper amount to create a film of thickness equal to an integral number of domain layers, holes or islands are formed on the surface with a step height equal to the lamellar period.[165–168] Typically these features have lateral sizes on the order of microns.

The presence of two well-defined film thicknesses in ordered films of 100,000 g/mol molecular weight symmetric polystyrene-*b*-polymethylmethacrylate copolymers is shown explicitly by X-ray reflectivity and off-specular scans through $q_z$ at a small constant value of $q_x$ by Sirota et al.[174] Similiarity in the forms of the off-specular and specular scans gives evidence for conformality of the top surface roughness and substrate roughness, while a phase offset between oscillations in the two scans is related to the thickness of the domains.

Cai et al.[145] present specular, transverse, and longitudinal diffuse scan data in a more detailed study of thin films from the same

polymer. Spun cast films are annealed under vacuum for 60 to 100 h at 170°C to aid the film in ordering. Correcting the reflectivity scans for diffuse scattering in the specular direction is essential for this system due to its strong off-specular scattering. The effect of the surface domains on the diffuse scattering may be seen clearly from a comparison of Figures 31 and 32, which present transverse scans from a film without surface domains and one with domains. Without surface domains, only a resolution limited peak is observed at $q_x = 0$. In the other case, diffuse scattering characteristic of the domains is seen. Model fits to the data were calculated using surface domain correlation functions determined from optical and atomic force microscopy and an expression for the structure factor (given above) which is derived in the specular approximation. While correlation lengths for all interface roughnesses were allowed to vary to provide the best agreement with the data, conformality between the roughnesses of different interfaces was set to zero. The shape of transverse scans was found to vary with annealing time, suggesting that the establishment of a thermodynamically favored surface structure is very sluggish. As annealing time is increased, the central peak in the transverse scan becomes narrower and the oscillations move to smaller values of $q_x$. We note that high resolution measurements very close to the specular condition are needed to characterize the domain–domain correlations because of their micron-scale size. These demand a collimation and dynamic range most readily achieved with a synchrotron source. Information about the interfacial roughness correlations[174] is available without performing such high resolution transverse scans as mentioned above.

Longitudinal diffuse scans also clearly show the presence of surface domains. A scan from a film without surface domains shows no oscillations at all, while those from a film with domains shows oscillations with a period corresponding to the domain height of 423 Å. Corresponding model off-specular curves calculated using the authors' formalism are seen to capture approximately the period and amplitude of these off-specular oscillations, but not the phase. They attribute

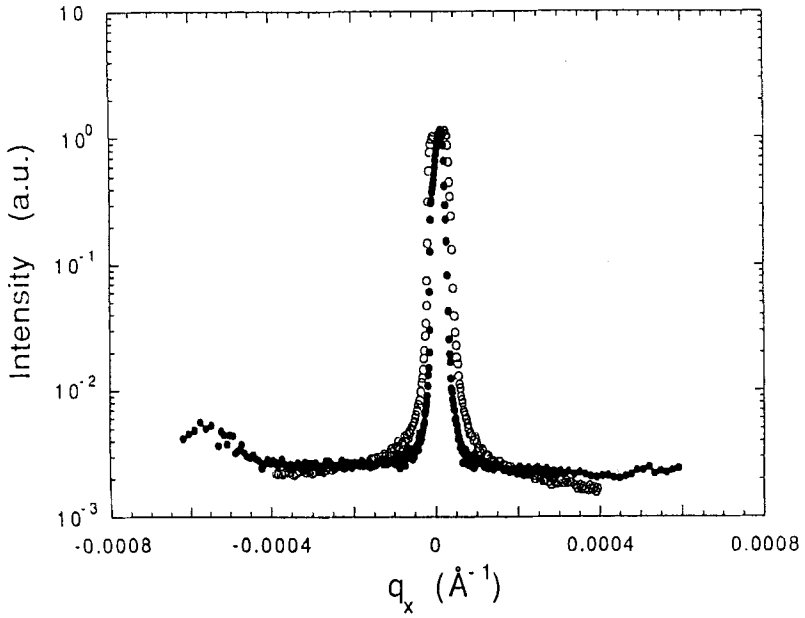


**FIGURE 31.** Measured intensity profiles of X-ray transverse scans at $q_z = 0.113$ Å$^{-1}$ (open circles) and $q_z = 0.081$ Å$^{-1}$ (filled circles) for a PS/PMMA diblock copolymer film without relief domains at the surface. (Reprinted, with permission, from reference 145.)

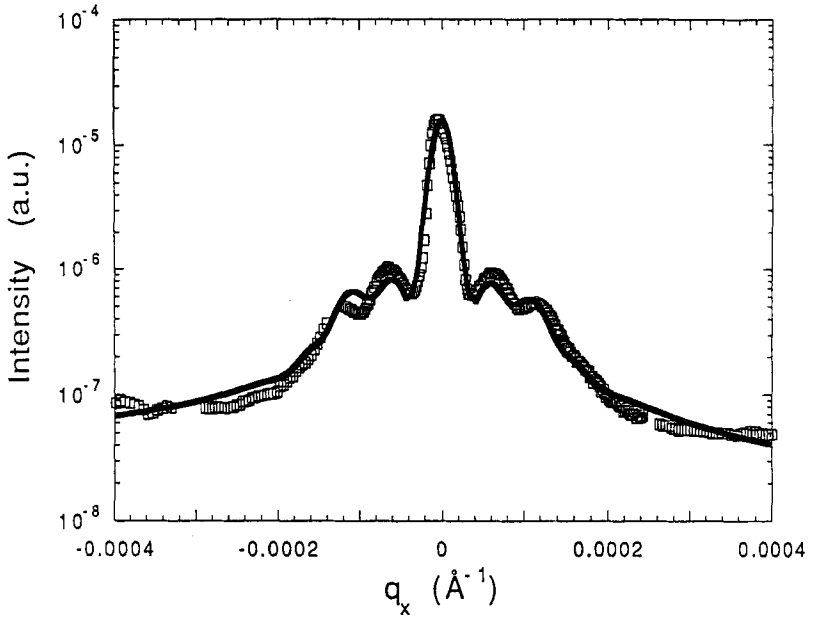


**FIGURE 32.** Measured intensity profiles of X-ray transverse scans at $q_z = 0.113$ Å$^{-1}$ (open squares) for a PS/PMMA diblock copolymer film which does have relief domains at the surface (64% coverage). Shown for comparison is the profile calculated using Eq. (108) and a correlation function derived from an AFM image of the surface. (Reprinted, with permission, from reference 145.)



this discrepancy to the fact that their treatment lies essentially within the Born approximation and does not include dynamic effects which would lead to a dependence upon surface coverage.

### 6. Grazing Incidence Small Angle Scattering (GISAS)

The study of diblock copolymer film off-specular scattering represents a link between the study of surface topology using diffuse scattering and the study of subsurface inhomogeneities using diffuse scattering. On the one hand the scattering from these block copolymer films may be described as scattering from a type of patterned surface roughness, while on the other hand it may be thought of as scattering from "holes" lying beneath the nominal surface presented by the tops of the surface domains. For the purposes of the present review we set measurements of the second kind apart under the classification of GISAS. Some of the formalisms presented above have been developed to the point where their application to the calculation of scattering from either surface or subsurface features is straightforward. However, to the author's knowledge only a very few measurements of the second type have been done.

In the GISAS experiment the focus of attention is on scattering of the refracted beam by inhomogeneities beneath the surface. By varying the incident angle, the effective depth from which the small angle scattering comes may be varied. For a hydrocarbon polymer if $\theta_0$ is kept below 0.14° for $CuK_\alpha$ radiation the effective penetration depth is $< 400$ Å. If the incident angle is allowed to increase far above $\theta_0$, then the scattering is very weak relative to the incident and refracted beams and a formalism in the specular beam approximation[141,144] may be applicable. For incident angles near critical a dynamic treatment in the DWBA such as that of Daillant and Bélorgey[143] must be invoked. In either case the calculation of the

scattering requires modeling the sample as a stack of layers, with the inhomogeneities distributed in the layers and the correlations among inhomogeneities within a single layer and between inhomogeneities of different layers defined.

While measurements of diblock thin film surface domains represent one example of GISAS with a polymer system, a couple of other examples from other materials science fields exist. The earliest study known to the author which explicitly seeks information on in-plane inhomogeneities in a thin film using GISAS is an investigation of gold thin film growth on glass by Levine and co-workers.[188,189] They modify a pinhole SAXS camera with a PSD by adding a sample goniometer capable of translating the sample into and out of the beam and rotating it to vary $q_0$. With the incident angle set to the critical value for glass, the PSD is placed with its axis perpendicular to the plane containing the incident and reflected beams at a height appropriate for capturing scattering of constant $q_z = q_c$ with $q_y$ varying above and below zero. At early stages of growth the adsorbate metal atoms form clusters or islands. Because the roughly hemispherical islands reflect poorly and the penetration depth exceeds the average film thickness, the incident beam is primarily reflected and refracted by the substrate.

As the refracted beam crosses the substrate surface the islands produce small angle scattering which is symmetric about the beam. This scattering comes at values of $q_y$ considerably larger ($0.02\ \text{Å}^{-1} < q_y < 0.15\ \text{Å}^{-1}$) than those at which surface roughness induced diffuse scattering is strongest. This fact together with the symmetry of the scattering about the beam allow it to be distinguished from scattering due simply to roughness. A pronounced peak in the scattering marks a characteristic distance of the island–island correlation, which the authors identify as a preferred center-to-center island spacing.

Naudon and co-workers consider GISAS to be a means of characterizing the size of Guinier-Preston (GP) zones in the near-surface region of a Al-Ag sample[190] and also precipitates in chemical vapor deposition (CVD) deposited tungsten-carbon films.[191] In contrast to studies of surface "bumps" such as those discussed above, GISAS from these samples deals with true subsurface inhomogeneities. The grazing incidence measurements with the Al-Ag alloys complement characterization of the bulk structure which has been pursued by several groups using small angle scattering in the transmission mode. A brief description of the alloy work illustrates the salient features of the measurement technique.

The authors use a fine linear focus source[190] and therefore cannot perform $q_y$ scans, but rather must use the "detector scan" type of off-specular measurement with a PSD employed to collect data over a range of $\phi$ simultaneously. This limits the size of the inhomogeneities that may be studied because no value of $2\theta$ less than $2\theta_c$ may be assessed in this geometry. The penetration of $CuK_\alpha$ X-rays in Al is somewhat less pronounced than in polymers, and even the material 1 $\mu$m away from the surface may be considered to be an interfacial zone. Thus, the authors make their measurements at an incidence angle, 0.7°, which is about three times the critical value. For this value of $\theta_0$ the reflectivity is $< 10^{-3}$, and the reflected beam at $2\theta = 1.4°$ does not figure prominently in the scattering observed because that from the GP zones is quite strong. The authors contend that the beam path lengths through the sample are small enough that multiple scattering can be neglected except for $2\theta$ very close to $\theta_0$. After correcting for absorption effects due to path length variation with $2\theta$, the small angle scattering curve shows a weak shoulder which the authors relate to a mean distance between spherical GP zones. The integrated intensity is used to derive the volume fraction of zones. Interpretation of this type of scattering data from a system with subsurface inhomogeneities is less straightforward than that from a $q_y$ scan due to the simultaneous variation of the in-plane scattering vector component and penetration depth.

## D. Grazing Incidence Diffraction

### 1. Technique and Theory

A final technique which uses small incident angles to gain surface sensitivity is grazing incidence diffraction (GID).[22,176] In this review we use the term GID restrictively to refer only to off-specular scattering out of the plane of incidence measured at values of $q$ far from the specular condition. For experiments of this type the $q$ component in the sample layer is very large compared to that perpendicular to the layer. This characteristically corresponds to limited penetration and sensitivity to lateral order in the sample. In this geometry it is possible to investigate static and dynamic correlations of molecules near the surface. In general the scattering far from the specular is extremely weak except in the case in which lateral correlations are sufficient to yield a Bragg peak. Even then such peaks will be weak in comparison to Bragg peaks from bulk systems, but they are measurable. One reason for the weak intensity is the small scattering volume involved. At grazing incidence the penetration depth may be orders of magnitude lower than that in a bulk measurement and there are fewer scattering entities to contribute to the signal. For polymer samples the low scattering power of the material (as compared to metals, for example) and the prevalence of amorphous structures will mean further limitations in the potential peak intensity. However, GID presents a unique opportunity for measuring order in polymer interfacial regions and will no doubt be exploited in the coming years, though perhaps not with the facility seen in applications of other grazing incidence X-ray techniques such as reflectivity.

The geometry of a GID measurement is that shown in Figure 19. In its most surface sensitive form the incident angle is kept just below the critical angle of the sample or sample substrate. Two advantages are won by this geometry. First, the scattering signal is markedly improved due to the enhancement of the surface electromagnetic field which occurs near $k_c$. For $k_{1,z}$ exactly equal to $k_c$ the surface field amplitude is twice that of the incident field, leading to a factor four enhancement in scattering power. For $k_{1,z}$ below $k_c$, the surface fields fall off monotonically to zero at $k_{1,z} = 0$. If an exit angle at the critical value is used as well a total scattering power enhancement of 16 is possible in principle, although in practice enhancements of 3 to 10 are accomplished. A second advantage of an incidence angle below $\theta_c$ is that extraneous diffuse scattering from the sample or substrate bulk is significantly reduced.

The scattering pattern expected from a GID experiment may be calculated using the DWBA approach.[192] For a truly two-dimensional system of zero thickness the Bragg reflections from an ordered structure become Bragg "rods" of intensity extending to infinity in the $z$ direction. For a thin film, the Bragg rods have a well-defined profile,[192,193] which reduces to that of a classical Bragg peak as the film thickness increases. From the peak location one may determine the spacing between diffracting planes using Bragg's law. The width of the peak yields a correlation length.[126]

### 2. Instrumentation

Several of the remarks made above regarding other grazing incidence techniques apply here. However, in contrast to diffuse scattering measurements near the specular condition for GID it is generally inappropriate to work with very unequal resolution in the $x$ and $y$ direction. In addition, the peak intensities of interest may even be weaker than scattering studied in grazing incidence diffuse measurements. Thus, work of this type on organic systems has been done almost exclusively with synchrotron-based spectrometers,[22] although Daillant et al.[84] present one GID peak from a self-assembled layer on silicon to press the point that some measurements in principle may be done with other sources.

GID experimental setups have been described by several authors.[22,177,186] Here, we

consider an illustrative example. Sirota et al.[178] discuss both a "low" and a "high" resolution spectrometer for GID measurements from liquid crystal systems. A comparision of the two systems is illustrative of the variations used by other authors[174] as well. A rotating anode-based triple axis spectrometer is used for "low resolution" measurements. The source operates with a $0.3 \times 0.3$ mm$^2$ effective source size and a vertically focusing pyrolytic graphite [002] crystal monochromator with equal focus-to-monochromator and monochromator-to-sample distances to provide horizontal Bragg-Brentano parafocusing. A flat pyrolytic graphite crystal is used as analyzer and the detector placed as close as possible to the sample ($\sim$ 350 mm) to maximize intensity. This setup produces a $\chi$ full width at half maximum (FWHM) of 12° for $2\theta = 20°$, where $\chi$ denotes the axis of sample rotation about a normal to the surface. The measured zero-arm $2\theta$ FWHM is 0.65° and the measured resolutions for $2\theta = 20°$ are $\Delta q_z = 9.2 \times 10^{-3}$ Å$^{-1}$ and $\Delta q_{\text{in-plane}} = 4.7 \times 10^{-2}$ Å$^{-1}$ with a direct beam intensity of $\sim 2 \times 10^8$ photons per second. This in-plane resolution is insufficient to distinguish the positional changes associated with a smectic-F-to-crystalline-G transition in thin films, but interlayer correlations can be studied for films thicker than about eight layers. In work by Gramsbergen et al.[179] a PSD is used in a low-resolution setup to greatly improve the counting statistics.

The high-resolution synchrotron-based spectrometer used by Sirota et al.[178] has a pair of asymmetrically cut $^{111}$Ge crystals as monochromator and a $^{220}$LiF crystal as analyzer. The FWHM in $\chi$ is about 2°, the longitudinal resolution, $\Delta q_{\text{in-plane}}$, is $3.8 \times 10^{-3}$ Å$^{-1}$ and the transverse resolution is limited by the sample mosaic. Measured peak intensities associated with the in-plane structure in 13 layer films are about 200 cpm with this spectrometer.

### 3. Applications

Eisenberger et al.[176] first applied this technique to the study of crystalline solid surfaces and it has since been applied by several groups to liquid metal surfaces,[177] liquid crystal surfaces,[178,179] Langmuir monolayers on liquid subphases,[180-186] and self-assembled octadecyltrichlorosilane (OTS) monolayers on solid supports.[84,187] As yet the application of this technique to polymeric systems[194-196] has been extremely limited.

Barton et al.[194] have studied a Langmuir film of OTS polymerized on an acidic aqueous subphase with pH 2. Comparison of first order Bragg peaks from the polymerized layer and an unpolymerized, highly compressed layer of stearic acid (SA) suggests that the polymerized layer has longer range order. The peak from the OTS is about three times as intense as that from SA, while consideration of the relative scattering powers alone would predict a ratio of 1.2. Because no second order diffraction peak is observed, no definitive structure could be proposed, and it is surmised that the extent of long range order in the polymerized layer is still less than that exhibited by some low temperature phases of nonpolymerizing monolayers of fatty acids and alcohols.[182,185]

Russell and co-workers[195,196] looked at polyimide thin films with GID to investigate the molecular ordering near the surface as opposed to that in the bulk. Their initial report discusses measurements at three different incident angles (0.12°, 0.14°, and 0.185°) about the critical angle of 0.18° which provide information on the structure corresponding to penetration depths of 55, 65, and $10^4$ Å, respectively. Clear peaks near values of the scattering vector $q$ of 0.4 and 0.78 Å$^{-1}$ are seen in Figure 33 for all three penetration depths. These may be associated with electron density correlations parallel to the chain axis and are identified as the 002 and 004 reflections of an orthorhombic unit cell. The positions and widths of these peaks decrease slightly with decreasing incident angle, suggesting better ordering nearer the surface. The scattering volume corrected peak intensities change dramatically with incident angle, those at 55 Å penetration being about 3% of those at $10^4$ Å penetration. Scattering features at $q > 0.8$ Å$^{-1}$ become markedly more distinct as the penetration depth is

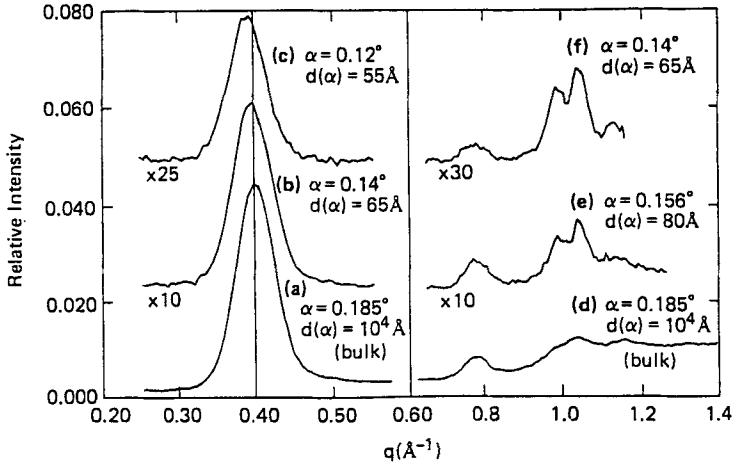


**FIGURE 33.** GISAS data from a polyimide film at incident angles, α, of 0.12°, 0.14°, and 0.185° just below and above the critical angle of 0.18° demonstrate a distinct improvement in the ordering near the air/polymer interface. For these incident angles **q** lies nearly parallel to the interface. A shift in the (002) reflection with penetration depth may be recognized by comparison with the vertical line at $q = 0.4$ Å$^{-1}$. (Reprinted, with permission, from reference 195.)



decreased, also evidencing an increased ordering near the surface. Other results from the work[196] indicate that no enhanced ordering occurs at the silicon substrate/polymer interface. Films of 100 Å thickness were more ordered that thicker films subjected to the same thermal treatment.

## IV. CONCLUDING REMARKS

A wide variety of X-ray scattering phenomena may be used for the characterization of polymer interfaces and the near-interfacial region. While all these phenomena are closely related theoretically, experimental considerations and differing sensitivities of the phenomena have led to the separate development of several scattering experiments, each with a particular area of applicability. This review has sought to recover some sense of the unity behind these disparate techniques as well as to clarify the advantages and disadvantages of each.

SAXS and XR already enjoy wide use in the characterization of polymer interfaces and the application of reflectivity will continue to expand. Complementary techniques such as neutron reflectivity and atomic force microscopy will play an important role in this widening use as they are important for minimizing ambiguity in the reflectivity analysis. The greatest opportunities for new advances in characterization lie, however, in the area of off-specular measurements. With the recent advances in the theory of this phenomena, the door is open for fruitful exploitation of the technique. Grazing incidence diffraction will enjoy somewhat less attention for polymer systems due to its limited application for amorphous structures.

## ACKNOWLEDGMENTS

I am thankful to J. Sokolov and Z. Cai for providing preprints of their work prior to publication and to W.-L. Wu for discussions of some of the material. V. Tsukruk and A. Schmidt provided many helpful comments on drafts of the text, and steered me to several articles of interest. Finally, I gratefully acknowledge assistance from S. Petrash in preparing the figures and from other members of my research group, T. Vierheller, A. Liebmann, H. Wu, and X. Li in preparing figures and proofreading the text.

## REFERENCES


1. Chou, N.J., XPS/SIMS/AES for surface and interface characterization of thin polymer films, in *New Characterization Techniques for Thin Polymer Film;* Tong, H.M.; Nguyen, L.T., Eds.; Wiley: New York, 1990.
2. Briggs, D., Characterization of surfaces, in *Comprehensive Polymer Science*, Vol. 1; Allen, J.; Bevington, J.C., Eds.; Pergamon Press: Oxford, 1989.
3. Arndt, T.; Wegner, G., in *Optical Techniques to Characterize Polymer Systems*; Bässler, H., Ed.; Elsevier: Amsterdam, 1989; p 41.
4. Henkee, C.S.; Thomas, E.L.; Fetters, L.J. *J. Mat. Sci.* **1988**, *23*, 1685.
5. Reneker, D.H.; Patil, R.; Kim, S.J.; Tsukruk, V.V., in *Polymer Characterization*, Kluwer: London, 1993.
6. White, H.S.; Earl, D.J.; Norton, J.D.; Kragt, H.J. *Anal. Chem.* **1990**, *62*, 1130.
7. Hickel, W.; Duda, G.; Jurich, M.; Kröhl, T.; Rochford, K.; Stegeman, G.I.; Swalen, J.D.; Wegner, G.; Knoll, W. *Langmuir*. **1990**, *6*, 1403.
8. Whitlow, S.J.; Wool, R.P. *Macromolecules*. **1991**, *24*, 5926
9. Green, P.F.; Doyle, B.L. Ion beam analysis of thin polymer films, in *New Characterization Techniques for Thin Polymer Films*; Tong, H.M; Nguyen, L.T., Eds.; Wiley: New York, 1990; p 139.
10. Budkowski, A.; Steiner, U.; Klein, J. *J. Chem. Phys.* **1992**, *97*, 5229.
11. Seggern, J.U.; Klotz, S.; Cantow, H.J. *Macromolecules*. **1989**, *22*, 3328.
12. Hong, P.P.; Boerio, F.J.; Clarson, S.J.; Smith, S.D. *Macromolecules*. **1991**, *24*, 4770.
13. Lindner, P.; Zemb, Th., Eds.; *Neutron, X-Ray and Light Scattering: Introduction to an Investigative Tool for Colloidal and Polymeric Systems*; Elsevier: Amsterdam, 1991.
14. Stamm, M. *Adv. Polymer Sci.* **1992**, *100*, 357.
15. Russell, T.P. *Annu. Rev. Mat. Sci.* **1991**, *21*, 249.
16. Stein, R.S. *Pure Appl. Chem.* **1991**, *63*, 941.
17. Sinha, S.K. *Phys. B*. **1991**, *173*, 25.
18. Russell, T.P. *Mat. Sci. Rep.* **1990**, *5*, 171.
19. Porod, G., General theory, in *Small Angle X-Ray Scattering*; O. Glatter, O. Kratky, Eds.; Academic Press: New York, 1982; Chapter 2.
20. Baltá-Calleja, F.J.; Vonk, C.G., *X-Ray Scattering of Synthetic Polymers*; Elsevier: New York, 1989.
21. Bachrach, R.Z., Ed.; *Synchrotron Radiation Research, Advances in Surface and Interface Science*; Vol. 1; Plenum: New York, 1992.
22. Als-Nielsen, J., Solid and liquid surfaces studied by synchrotron X-ray diffraction, in *Topics in Current Physics*, Vol. 43, *Structure and Dynamics of Surfaces II*; Schommers, W.; von Blanckenhagen, P., Eds.; Springer-Verlag: New York, 1987.
23. Hashimoto, T.; Fujimura, M.; Kawai, H. *Macromolecules*. **1980**, *13*, 1660.
24. Tyagi, D.; McGrath, J.E.; Wilkes, G.L. *Polymer Sci. Eng.* **1986**, *26*, 1371.
25. Hendricks, R.W.; Shaffer, L.B.; Bonfiglioli, A.; Rojas, F.A.; Gerold. V.; Dünkeloh, H.; Epperson, J.E.; Jensen, B.T.; Levelut, A.M.; Dartyge, E.; Perret, R.; Balyuzi, H.H.M.; Woodcock, M.; Schmidt, P.W.; Lin, J.S.; Wershaw, R.I. *J. Appl. Cryst*. **1978**, *11*, 196.
26. Kratky, O.; Pilz, I.; Schmits, P. *J. Coll. Int. Sci.* **1966**, *21*, 24.
27. Guinier, A.; Fournet, G.; *Small Angle Scattering of X-Rays*, John Wiley and Sons: New York, 1955.
28. Porod, G. *Kolloid-Z.* **1951**, *124*, 83.
29. Porod, G. *Kolloid-Z.* **1952**, *125*, 51.
30. Porod, G. *Kolloid-Z.* **1952**, *125*, 108.
31. Auvray, L.; Auroy, P., in *Neutron, X-Ray and Light Scattering: Introduction to an Investigative Tool for Colloidal and Polymeric Systems*; Lindner, P.; Zemb, Th., Eds.; Elsevier: 1991; p 199.
32. Kirste, R.; Porod, G. *Koll. Z., Z. Polymer*. **1962**, *184*, 1.
33. Bale, H.D.; Schmidt, P.W. *Phys. Rev. Lett*. **1984**, *53*, 596.
34. Glatter, O., Data treatment, in *Small Angle X-Ray Scattering*; O. Glatter, O. Kratky, Eds.; Academic Press: New York, 1982; Chapter 4.
35. Ruland, W. *J. Appl. Cryst*. **1971**, *4*, 70.
36. Bonart, R.; Müller, E.H.; *J. Macromol. Sci.-Phys.* **1974**, *B10*, 177.
37. Vonk, C.G. *J. Appl. Cryst.*, **1973**, *6*, 81.
38. Ruland, W. *Colloid Polym. Sci*. **1977**, *255*, 417.
39. Koberstein, J.T.; Morra, B; Stein, R.S. *J. Appl. Cryst.*, **1980**, *13*, 34.
40. Roe, R.-J. *J. Appl. Cryst.*, **1982**, *15*, 182.
41. Shilov, V.V.; Tsukruk, V.V.; Lipatov, Y.S *Polymer Sci. U.S.S.R.* **1984**, *26,* 1503.
42. Hendricks, R.W.; Schmidt, P.W. *Acta Phys. Aust.* **1967**, *26*, 97.
43. Hendricks, R.W.; Schmidt, P.W. *Acta Phys. Aust.* **1973**, *37*, 20.
44. Ruland, W. *Macromolecules*. **1987**, *20*, 87.
45. Stamm, M. *Polym. Prepr. (Am. Chem. Soc., Dev. Polymer Chem.)* **1983**, *24*, 380.
46. Bartels, C.R.; Crist, B.; Graessley, W.W. *J. Polym. Sci. Polym. Lett. Ed.* **1983**, *21*, 495.
47. Stamm, M.; *Polym. Prepr. (Am. Chem. Soc., Dev. Polymer Chem.)* **1987**, *28*, 56.
48. Brautmeier, D.; Stamm, M.; Lindner, P.J. *Appl. Cryst.* **1991**, *24*, 665.
49. Yoo, J.N.; Sperling, L.H.; Glinda, C.J.; Klein, A. *Macromolecules*. **1990**, *23*, 3962.
50. Garbella R.; Wendorff, J.W. *Makromol. Chem. Rapid Commun.* **1986**, *7*, 591.
51. Roe, R.-J.; Fishkis, M.; Chang, J.C. *Macromolecules*. **1981**, *14*, 1091.
52. Siemann, U.; Ruland, W. *Coll. Polymer Sci*. **1982**, *260*, 999.
53. Hadziioannou, G.; Mathis, A.; Skoulios, A. *Colloid Polymer Sci*. **1979**, *257*, 15.

54. Hadziioannou, G.; Skoulios, A. *Macromolecules.* **1982**, *15*, 258.
55. Strobl, G.R.; Schnieder, M.J. *J. Polymer Sci. Polymer Phys. Ed.* **1980**, *18*, 1348.
56. Ophir, Z.; Wilkes, G.J. *Polymer Sci.: Polymer Phys. Ed.* **1980**, *18*, 1469.
57. Hashimoto, T.; Shibayama, M.; Kawai, H. *Macromolecules.* **1980**, *13*, 1237.
58. Todo, A.; Hashimoto, T.; Kawai, H. *J. Appl. Cryst.* **1978**, *11*, 558.
59. Hashimoto, T.; Todo, A.; Itoi, H.; Kawai, H. *Macromolecules.* **1977**, *10*, 377.
60. Alexander, L.E., *X-Ray Diffraction Methods in Polymer Science*, Wiley- Interscience: New York, 1969.
61. Kiessig, H. *Ann. Phys.* **1931**, *10*, 769.
62. Reiter, G.; Hüttenbach, S.; Foster, M.D.; Stamm, M. *Fresenius J. Anal. Chem.* **1991**, *341*, 284.
63. Lekner, J.; *Theory of Reflection of Electromagnetic and Particle Waves*, M. Nijhoff Publishers: Dordrecht, The Netherlands, 1987.
64. Pedersen, J.S. *J. Appl. Cryst.* **1992**, *25*, 129.
65. Sivia, D.S.; Hamilton, W.A.; Smith, G.S. *Phys. B.* **1991**, *173*, 121.
66. Sivia, D.S.; Hamilton, W.A.; Smith, G.S., Rieker, T.P.; Pynn, R. *J. Appl. Phys.* **1991**, *70*, 732.
67. Névot, L.; Pardo, B.; Corno, J. *Rev. Phys. Appl.* **1988**, *23*, 1675.
68. Croce, P.; Névot, L. *Rev. Phys. Appl.* **1976**, *11*, 113.
69. Croxton, C.A.; *Statistical Mechanics of the Liquid Surface*, Wiley: New York, 1980.
70. Compton, A. *Philos. Mag.*, **1923**, *14*, 1121.
71. Parratt, L.G. *Phys. Rev.* **1954**, *95*, 359.
72. Sauro, J.; Fankuchen, I.; Wainfan, N. *Phys. Rev.* **1963**, *132*, 1544.
73. Croce, P.; Devant, G.; Sere, M.G.; Verhaeghe, M.F. *Surf. Sci.* **1970**, *22*, 173.
74. Foster, M.; Stamm, M.; Reiter, G.; Hüttenbach, S. *Vacuum.* **1990**, *41*, 1441.
75. Weiss, A.H.; Deutsch, M.; Braslau, A.; Ocko, B.M.; Pershan, P.S. *Rev. Sci. Instr.* **1986**, *57*, 2544.
76. Jark, W.; Stöhr, J. *Nucl. Instr. Methods.* **1988**, *A266*, 654.
77. Pershan, P.S. *J. Phys. (Paris)* **1990**, *C7 (50, Suppl.)*, C7-1.
78. Pershan, P.S.; Als-Nielsen, J. *Phys. Rev. Lett.* **1984**, *52*, 759.
79. Pershan, P.S.; Braslau, A.; Weiss, A.H.; Als-Nielsen, J. *Phys. Rev. A.* **1987**, *35*, 4800.
80. Parrish, W.; Erickson, C.; Huang, T. C.; Hart, M.; Gilles, B.; Toraya, H. *Mat. Res. Soc. Symp. Proc.* **1991**, *208*, 327.
81. Chason, E.; Warwick, D.T. *Mat. Res. Soc. Symp. Proc.* **1991**, *208*, 351.
82. Loxley, N.; Bowen, D. K.; Tanner, B. K. *Mat. Res. Soc. Symp. Proc.* **1991**, *208*, 107.
83. Schlossman, M.L.; Pershan, P.S.; *X-Ray and Neutron Scattering from Liquid Surfaces in Light Scattering by Liquid Surfaces and Complementary Techniques;* Langevin, D., Ed.; Marcel Dekker: New York, 1992; Chapter 18.
84. Daillant, J.; Benattar, J. J.; Leger, L. *Phys. Rev. A.* **1990**, *41*, 1963.
85. Naudon, A.; Chirab, J.; Gondeau, P.; Mimault, J. *J. Appl. Cryst.* **1989**, *22*, 460.
86. Bilderback, D.H. *SPIE.* **1981**, *315*, 100.
87. Bilderback, D.H.; Hubbard, J. *Nucl. Instr. Methods* **1982**, *195*, 85, 91.
88. Tanner, B.K.; Miles, S.J.; Bowen, D. K.; Hart, L.; Loxley, N. *Mat. Res. Soc. Symp. Proc.* **1991**, *208*, 345.
89. Elben, H.; Strobl, G. *Macromolecules.* **1993**, *26*, 1013.
90. Bornside, D. Ph.D. Thesis, University of Minnesota, Minneapolis, 1988.
91. Rieutord, F.; Benattar, J.J.; Rivoira, R.; Lepêtre, Y.; Blot, C.; Luzet, D. *Acta Cryst.* **1989**, *A45*, 445.
92. Sikka, M.; Singh, N.; Karim, A.; Bates, F.S. *Phys. Rev. Lett.* **1993**, *70*, 207.
93. Kunz, M.C.; Mayes, A.M.; Russell, T.P. *Am. Phys. Soc.* **1993**, *48*, 421.
94. Green, P.F.; Russell, T.P. *Macromolecules.* **1992**, *25*, 783.
95. Murphy, M.A.; Blaise, J.K.; Peticolas, L.J.; Bean, J.C. *Langmuir.* **1993**, *2*, 1134.
96. Xu, S.; Murphy, M.A.; Amador, S.M.; Blaise, J.K. *J. Phys. I*, **1991**, *1*, 1131.
97. Ulman, A.; *An Introduction to Ultrathin Organic Films;* Academic Press: New York, 1991.
98. Gaines, G.L.; *Insoluble Monolayers at Liquid-Gas Interfaces;* Wiley Interscience: New York, 1966.
99. Swalen, J.D.; Allara, D.L.; Andrade, J.D.; Chandrass, E.A.; Garoff, S.; Israelarchvili, J.; McCarthy, T.J.; Murray, R.; Pease, R.F.; Rabolt, J.F.; Wynne, K.J.; Yu, H. *Langmuir.* **1987**, *3*, 932.
100. Roberts, G.G. *Adv. Phys.* **1985**, *34*, 475.
101. Mathauer, K.; Embs, F.; Wegner, G.; in Comprehensive Polymer Science First Suppl. Vol. Allen, G.; Aggarwal, S.L.; Russo, S.; Eds.; Pergamon Press: Oxford, 1992; Chapter 17.
102. Pomerantz, M.; Segmüller, A. *Thin Solid Films.* **1980**, *68*, 33.
103. Rieutord, F.; Benattar, J.J.; Bosio, L.; Robin, P.; Blot, C.; de Kouchkovsky, R. *J. Phys. (Paris).* **1987**, *48*, 679.
104. Foster, M.D.; Vierheller, T.; Schmidt, A.; Mathauer, K.; Knoll, W.; Wegner, G.; Satija, S.; Majkrzak, C.F. *Mat. Res. Soc. Symp. Proc.* **1992**, *248*, 40.
105. Schwartz, D.K.; Garnaes, J.; Viswanathan, R.; Zasadzinski, J.A. *Science.* **1992**, *257*, 508.
106. Tsukruk, V.V.; Foster, M.D.; Reneker, D.R.; Schmidt, A.; Knoll, W. accepted in *Langmuir.*
107. Tsukruk, V.V.; Foster, M.D.; Reneker, D.R.; Schmidt, A.; Wu, H.; Knoll, W. accepted in *Macromolecules.*
108. Vierheller, T.R.; Foster, M.D.; Wu, H.; Schmidt, A.; Mathauer, K.; Knoll, W.; Wegner, G.; Satija, S.; Majkrzak, C. Manuscript in preparation.

109. Mozz, R.; Sajiv, J. *J. Coll. Interface Sci.* **1984**, *100*, 465.
110. Nuzzo, R.G.; Allara, D.L. *J. Am. Chem. Soc.* **1983**, *205*, 4481.
111. Tidswell, I.M.; Ocko, B.M.; Pershan, P.S.; Wasserman, S.R.; Whitesides, G.M.; Axe, J.D. *Phys. Rev. B.* **1990**, *41*, 1111.
112. Wasserman, S.R.; Whitesides, G.M.; Tidswell, I.M.; Ocko, B.; Pershan, P.S.; Axe, J.D. *J. Am. Chem. Soc.* **1989**, *111*, 5852.
113. Silberzam, P.; L'eger, L.; Aussere, D.; Bennatton, J.J. *Langmuir.* **1991**, *7*, 1647.
114. Tillman, N.; Ulman, A.; Penner, T.L. *Langmuir.* **1989**, *5*, 101.
115. Hoffman, D.; Rabolt, J.F. *Bull. Am. Phys. Soc.* **1993**, *38*, 713.
116. Auroy, P.; Mir, Y.; Auvray, L. *Phys. Rev. Lett.* **1992**, *69*, 93.
117. Kramer, E.J.; Green, P.; Palmstrøm, C.J. *Polymer.* **1984**, *25*, 473.
118. Russell, T.P.; Karim, A.; Mansour, A.; Felcher, G.P. *Macromolecules.* **1988**, *21*, 1890.
119. Hüttenbach, S.; Stamm, M.; Reiter, G.; Foster, M. *Langmuir.* **1991**, *7*, 2438.
120. Kramer, E.J.; Green, P.; Palmstrøm, C.J. *Polymer.* **1984**, *25*, 473.
121. Schaub, M.; Mathauer, K.; Schwiegk, S.; Albouy, P.-A.; Wenz, G.; Wegner, G. *Thin Solid Films.* **1992**, *210 / 211*, 397.
122. Sawyer, L.C.; Grubb, D.T.; *Polymer Microscopy;* Chapman & Hall: New York, 1987.
123. Sinha, S.K.; Sanyal, M.K.; Huang, K.G.; Gibaud, A.; Rafailovich, M.; Sokolov, J.; Zhao, X.; Zhao, W. *Springer Proc. Phys.* **1992**, 85.
124. Rieutord, F.; Benattar, J.J; Rivoira, R.; Lepêtre, Y.; Biot, C.; Luzet, D. *Acta Cryst.* **1989**, *A45*, 445.
125. Chupa, J.A.; McCauley, J.P., Jr.; Strongin, R.M.; Smith, A.B., III; Peticolas, L.J.; Bean, J.C.; Blaise, J.K. *Abstr. of ACS Coll. Div. Spring Mtg.* **1993**, No. 145.
126. Yoneda, Y. *Phys. Rev.* **1963**, *131,* 2010.
127. Guenter, O.J. *J. Appl. Phys.* **1965**, *30*, 1361.
128. Nigam, A.N. *Phys. Rev. A.* **1965**, *4*, 1189.
129. Sauro, J.; Fankuchen, I.; Wainfan, N. *Phys. Rev.* **1963**, *132*, 1544.
130. Sauro, J.; Bindell, J.; Wainfan, N. *Phys. Rev.* **1966**, *143*, 439.
131. Bindell, J.B.; Wainfan, N. *J. Appl. Cryst.* **1970**, *3*, 503.
132. Kov'ev, E.K.; Matveev, Yu.A. *Sov. Phys. Solid State.* **1981**, *23*, 331.
133. Hogrefe, H. Ph.D. Thesis, University of Hamburg, Hamburg, Germany, 1985.
134. Croce, P.; Devant, G.; Sere, M.G.; Verhaeghe, M.F. *Surf. Sci.* **1970**, *22*, 173.
135. Beckmann, P.; Spizzichio, A.; *The Scattering of Electromagnetic Waves from Rough Surfaces;* Artech House: Norwood, MA, 1987.
136. Croce, P.; Prod'homme, L. *Nuovo Rev. Opt.* **1976**, *7*, 121.
137. Croce, P. *Nuovo Rev. Opt.* **1977**, *8*, 127.
138. Névot, L.; Croce, P. *Rev. Phys. Appl.* **1980**, *15*, 761.
139. Sinha, S.K.; Sirota, E.B.; Garoff, S.; Stanley, H.B. *Phys. Rev.* **1988**, *B38*, 2297.
140. Wong, P.-Z.; Bray, A. *J. Phys. Rev.* **1988**, *B 37*, 7751.
141. Stearns, D.G. *J. Appl. Phys.* **1989**, *65*, 491.
142. Pynn, R. *Phys. Rev.* **1991**, *B45,* 602.
143. Daillant, J.; Bélorgey, O. *J. Chem. Phys.* **1992**, *97*, 5824.
144. Daillant, J.; Bélorgey, O. *J. Chem. Phys.* **1992**, *97*, 5837.
145. Cai, Z.-H., Huang, K.; Montano, P.A.; Russell, T.P.; Bai, J. M.; Zajac, G.W. *J. Chem. Phys.* **1993**, *98*, 2376.
146. Braslau, A.; Pershan, P.S.; Swislow, B.M.; Ocko, B.M; Als-Nielsen, J. *Phys. Rev. A.* **1988**, *38*, 2457.
147. Wu, W.-L. *J. Chem. Phys.* **1993**, *98*, 1687.
148. Wu, W.-L. Private communication.
149. Pershan, P.S. *Faraday Disc. Chem. Soc.* **1990**, *89*, 231.
150. Schlossman, M.L.; Schwartz, D.K.; Kawamoto, E.H.; Kellogg, G.J.; Pershan, P. S.; Ocko, B.M.; Kim, M.W.; Chung, T.C. *Mat. Res. Soc. Symp. Proc.* **1990**, *177*, 351.
151. Sanyal, M.D.; Sinha, S.K.; Huang, K.G.; Ocko, B.M. *Phys. Rev. Lett.* **1991**, *66*, 628.
152. *Handbook of Mathematical Functions;* Abramowitz, M.; Stegun, I.A.; Eds.; National Bureau of Standards: Washington, D.C., 1972.
153. Daillant, J.; Bosio, L.; Harzallah, B.; Benattar, J.J. *J. Phys. II (Paris).* **1991**, *1*, 149.
154. Tidswell, I.M.; Rabedeau, T.A.; Pershan, P.S.; Kosowsky, S.D. *Phys. Rev. Lett.* **1991**, *66,* 2108.
155. Fischetti, R.F.; Xu, S.; Blaise, J.K. *Mat. Res. Soc. Symp. Proc.* **1991**, *208*, 231.
156. Kawamoto, E.H.; Lee, S.; Pershan, P.S.; Deutsch, M.; Maskil, N.; Ocko, B.M. Preprint.
157. Garoff, S.; Sirota, E.B.; Sinha, S.K.; Stanley, H.B. *J. Chem. Phys.* **1989**, *90*, 7505.
158. Sokolov, J.; Zhao, W.; Zhao, X.; Rafailovich, M.H.; Sinha, S.K.; Sanyal, M.; Ocko, B.M.; Mansfield, T.; Kramer, E.; Bates, F.S. *Bull. Am. Phys. Soc.* **1991**, *36,* 384.
159. Zhao, W.; Zhao, X.; Rafailovich, M.H.; Sokolov, J.; Mansfield, T.; Stein, R.S.; Composto, R.C.; Kramer, E.J.; Jones, R.A.L.; Sansone, M.; Nelson, M. *Phys. B.* **1991**, *73*, 43.
160. Zhao, W.; Zhao, X.; Sokolov, J.; Rafailovich, M.H.; Sanyal, M.K.; Sinha, S.K.; Cao, B.H.; Kim, M.W.; Sauer, B. *J. Chem. Phys.*, **1992**, 97, 8536.
161. Zhao, W.; Catailovick, M.H.; Sakolov, J.; Fetters, L.J.; Plano, R.; Sanyal, M.K.; Sinha, S.K.; Sauer, B.B. *Phys. Rev. Lett.* **1993**, *70*, 1453.
162. Pleiner, H.; Harden, J.L; Pincus, P. *Europhys. Lett.* **1988**, *7*, 383.
163. Harden, J.L; Pleiner, H.; Pincus, P.A. *J. Chem. Phys.* **1991**, *94*, 5208.
164. Bates, F.S.; Fredrickson, G.H. *Annu. Rev. Phys. Chem.* **1990**, *41*, 525.

165. Coulon, G.; Russell, T.P.; Deline, V.R.; Green. P.F. *Macromolecules*. **1989**, *22*, 2581.
166. Coulon, G.; Ausserre, D.; Russell, T.P. *J. Phys. Fr.* **1990**, *51*, 777.
167. Coulon, G.; Collin, B.; Aussere, D.; Chatenay, D.; Russell, T.P. *J. Phys. Fr.* **1990**, *51*, 2801.
168. Coulon, G.; Daillant, J.; Collin, B.; Benattar, J.J.; Gallot, Y. *Macromolecules*. **1993**, *26*, 1582.
169. Anastasiadis, S.H.; Russell, T.P.; Satija, S.K.; Majkrzak, C.F. *J. Chem. Phys.* **1990**, *92*, 5677.
170. Foster, M.D.; Sikka, M.; Singh, N.; Bates, F.S.; Satija, S.K.; Majkrzak, C.F. *J. Chem. Phys.* **1992**, *92*, 8605.
171. de Jeu, W.H.; Lambooy, P.; Hamley, I.; Vaknin, D.; Pedersen, J.S.; Kjaer, K.; Seyger, R.; van Hutten, P.; Hadziioannou, G. *J. Phys. II Fr.* **1993**, *3*, 139.
172. de Jeu, W.H.; Lambooy, P.; Vaknin, D. *Macromolecules*. **1993**, 26, 4973.
173. Hasegawa, H.; Hashimoto, T. *Macromolecules*. **1985**, *18*, 589.
174. Sirota, E.B.; Hughes, G.J.; Sinha, S.K.; Satija, S.K.; Russell, T.P. *Polymer Prepr. (Am. Chem. Soc. Dev. Polym. Chem.)* **1990**, *31*, 81.
175. Tidswell, I.M.; Rabedeau, T.A.; Pershan, P.S.; Folkers, J.P.; Baker, M.V.; Whitesides, G.M. *Phys. Rev. B*. **1991**, *44*, 10869.
176. Eisenberger, R.; Marra, W.C. *Phys. Rev. Lett*. **1981**, *46*, 1081.
177. Thomas, B.N.; Barton, S.W.; Novak, F.; Rice, S.A. *J. Chem. Phys.* **1986**, *86*, 1036.
178. Sirota, E.B.; Pershan, P.S.; Sorensen, L.B.; Collett, J. *Phys. Rev. A*. **1987**, *36*, 2890.
179. Gramsbergen, E.F.; Als-Nielsen, J.; de Jeu, W.H. *Phys. Rev. A*. **1988**, *37*, 1335.
180. Kjaer, K.; Als-Nielsen, J.; Helm, C.A.; Laxhube, L.A.; Möhwald, H. *Phys. Rev. Lett.* **1987**, *58*, 2224.
181. Dutta, P.; Peng, J.B.; Lin, B.; Ketterson, J.B.; Prakash, M.; Georgeopoulos, P.; Ehrlich, S. *Phys. Rev. Lett*. **1987**, *58*, 2228.
182. Barton, S.W.; Thomas, B.N.; Flom, E.B.; Rice, S.A.; Lin, B.; Peng, J.B.; Ketterson, J.B.; Dutta, P. *J. Chem. Phys.* **1988**, *89*, 2257.
183. Helm, C.A.; Möhwald, H.; Kjaer, K.; Als-Nielsen, J. *Biophys. J*. **1987**, *52*, 381.
184. Kjaer, K.; Als-Nielsen, J.; Helm, C.A.; Tippmann-Krayer, P.; Möhwald, H. *J. Phys. Chem.* **1989**, *93*, 3200.
185. Lin, B.; Shih, C.; Bohanon, T.M.; Ice, G.E.; Dutta, P. *Phys. Rev. Lett*. **1990**, *65*, 191.
186. Schwartz, D.K.; Schlossmann, M.L.; Pershan, P.S. *J. Chem. Phys*. **1992**, *96*, 2356.
187. Tidswell, I.M.; Rabedeau, T.A.; Pershan, P.S.; Kosowsky, S.D.; Folkers, J.P.; Whitesides, G.M. *J. Chem. Phys.* **1991**, *95*, 2854.
188. Levine, J.R.; Cohen, J.B.; Chung, Y.W.; Georgopoulos, P. *J. Appl. Cryst.* **1989**, *22*, 528.
189. Levine, J.R.; Cohen, J.B.; Chung, Y.W. *Surf. Sci.* **1991**, *248*, 215.
190. Naudon, A.; Slimani, T.; Goudeau, P. *J. Appl. Cryst.* **1991**, *24*, 501.
191. Slimani, T.; Goudeau, P.; Naudon, A. *J. Appl. Cryst.* **1991**, *24*, 638.
192. Vineyard, G.H. *Phys. Rev. B*. **1982**, *26*, 4146.
193. Brunel, M.; de Bergevin, F.; *Acta Crystallogr. Sect.* **1986**, 299.
194. Barton, S.W.; Goudot, A.; Rondelez, F. *Langmuir*. **1991**, *7*, 1029.
195. Russell, T.P.; Factor, B.; Toney, M.F. *Phys. Rev. Lett*. **1991**, *66*, 1181.
196. Factor, B.J.; Russell, T.P.; Toney, M.F. *Macromolecules*. **1993**, *26*, 2847.